



HAL
open science

Marche des robots humanoïdes avec des semelles souples

Adrien Pajon

► **To cite this version:**

Adrien Pajon. Marche des robots humanoïdes avec des semelles souples. Automatic. Université Montpellier, 2017. English. NNT : 2017MONT060 . tel-01938409

HAL Id: tel-01938409

<https://theses.hal.science/tel-01938409>

Submitted on 28 Nov 2018

HAL is a multi-disciplinary open access archive for the deposit and dissemination of scientific research documents, whether they are published or not. The documents may come from teaching and research institutions in France or abroad, or from public or private research centers.

L'archive ouverte pluridisciplinaire **HAL**, est destinée au dépôt et à la diffusion de documents scientifiques de niveau recherche, publiés ou non, émanant des établissements d'enseignement et de recherche français ou étrangers, des laboratoires publics ou privés.

**THÈSE POUR OBTENIR LE GRADE DE DOCTEUR
DE L'UNIVERSITÉ DE MONTPELLIER**

En Robotique

École doctorale I2S

Unité de recherche CNRS-UM LIRMM IDH

Humanoid Robots Walking with Soft Soles

Présentée par Adrien PAJON

Le 1er Décembre 2017

Sous la direction de Abderrahmane KHEDDAR

Devant le jury composé de

Olivier BRUNEAU, Professeur, Université Paris-Saclay

Yannick Aoustin, Professeur, Université de Nantes

Philippe SOUÈRES, Directeur de Recherche, LAAS-CNRS

Daniele PUCCI, Researcher, IIT Italy

Pierre-Brice WIEBER, Chargé de Recherche, Inria Grenoble

Sylvain MIOSSEC, Maître de Conférence, Université d'Orléans-IUT de Bourges

Rapporteur

Rapporteur

Président du Jury

Examineur

Examineur

Co-Encadrant



**UNIVERSITÉ
DE MONTPELLIER**

I would like to dedicate this thesis to my loving wife and parents . . .

Acknowledgements

My first thoughts, as I write the last lines of this manuscript, go to the two persons who have watched over its growth, Abderrahmane Kheddar and Sylvain Miossec. I was aware from the start of the difficulties that could arise by placing my research under the advice of two purposeful researchers, and it is with great delight that I see how we have been working together in *bonne entente*.

I want to thank Abderrahmane Kheddar for all the time and thorough feedback that he gave me. I have always been impressed how, in the midst of professoral business, he would still find ways to set aside time for deep discussion. It has been a privilege for me to work under his relentless curiosity and high scientific standards.

I want to thank equally Sylvain Miossec for these three years. Dr Miossec really helped me on hard theoretical part of my PhD and he has kept the momentum going with never-ending energy and enthusiasm, making me discover the excitement of research. Looking at the path behind us leaves me eager to ask: *et après?*

Giovanni De Magistris is a man who made this PhD possible, not only by initiating me to the research behavior, but also by being always so attentive and open to discussion. Knowing at the back of my mind that I could always reach out to him was of great support.

I want to thank Enrico Chiovetto which is the man who initiate me to human study and measurements. We spend three months together in your Germany and that was a rich experience to speak and share about human inspired vision of robotics.

I would like to address a special thank to Kevin Chappellet as well. They say one can really appreciate the value of people in times of stress, to which I will only add that I was very glad to be with Mr. Chappellet managing the robot interface and hardware during the robot experiments as I reached the deadline of any article I prepared and wrote.

This thesis has also benefited from open and friendly technical discussions with Pierre Gergondet, Hervé Audren, Don Joven Agravante, Joris Vaillant, Vincent Samy, Karim Bouyarmane and Stéphane Caron. Thank you all for your time. I am looking forward to our next encounters.

Finally, I want thank all the other person I had the chance to get to know during my PhD and I forgot to mention in my acknowledgements.

Abstract

English

When unexpected changes of the ground surface occur while walking, the human central nervous system needs to apply appropriate control actions to assure dynamic stability. Many studies in the motor control field have investigated the mechanisms of such a postural control and have widely described how center of mass (COM) trajectories, step patterns and muscle activity adapt to avoid loss of balance. Measurements we conducted show that when stepping over a soft ground, participants actively modulated the ground reaction forces (GRF) under the supporting foot in order to exploit the elastic and compliant properties of the surface to dampen the impact and to likely dissipate the mechanical energy accumulated during the ‘fall’ onto the new compliant surface.

In order to control more efficiently the feet-ground interaction of humanoid robots during walking, we propose adding outer soft (i.e. compliant) soles to the feet. They absorb impacts and cast ground unevenness during locomotion on rough terrains. However, they introduce passive degrees of freedom (deformations under the feet) that complexify the tasks of state estimation and overall robot stabilization. To address this problem, we devised a new walking pattern generator (WPG) based on a minimization of the energy consumption that offers the necessary parameters to be used jointly with a sole deformation estimator based on finite element model (FEM) of the soft sole to take into account the sole deformation during the motion. Such FEM computation is time costly and inhibit online reactivity. Hence, we developed a control loop that stabilizes humanoid robots when walking with soft soles on flat and uneven terrain. Our closed-loop controller minimizes the errors on the center of mass (COM) and the zero-moment point (ZMP) with an admittance control of the feet based on a simple deformation estimator. We demonstrate its effectiveness in real experiments on the HRP-4 humanoid walking on gravels.

Français

Lorsque des changements inattendus de la surface du sol se produisent lors de la marche, le système nerveux central humain doit appliquer des mesures de contrôle appropriées pour assurer une stabilité dynamique. De nombreuses études dans le domaine de la commande moteur ont étudié les mécanismes d'un tel contrôle postural et ont largement décrit comment les trajectoires du centre de masse (COM), le placement des pas et l'activité musculaire s'adaptent pour éviter une perte d'équilibre. Les mesures que nous avons effectuées montrent qu'en arrivant sur un sol mou, les participants ont modulé de façon active les forces de réaction au sol (GRF) sous le pied de support afin d'exploiter les propriétés élastiques et déformables de la surface pour amortir l'impact et probablement dissiper l'énergie mécanique accumulée pendant la 'chute' sur la nouvelle surface déformable.

Afin de contrôler plus efficacement l'interaction pieds-sol des robots humanoïdes pendant la marche, nous proposons d'ajouter des semelles extérieures souples (c'est-à-dire déformables) aux pieds. Elles absorbent les impacts et limitent les effets des irrégularités du sol pendant le mouvement sur des terrains accidentés. Cependant, ils introduisent des degrés de liberté passifs (déformations sous les pieds) qui complexifient les tâches d'estimation de l'état du robot et ainsi que sa stabilisation globale. Pour résoudre ce problème, nous avons conçu un nouveau générateur de modèle de marche (WPG) basé sur une minimisation de la consommation d'énergie qui génère les paramètres nécessaires pour utiliser conjointement un estimateur de déformation basé sur un modèle éléments finis (FEM) de la semelle souple pour prendre en compte sa déformation lors du mouvement. Un tel modèle FEM est coûteux en temps de calcul et empêche la réactivité en ligne. Par conséquent, nous avons développé une boucle de contrôle qui stabilise les robots humanoïdes lors de la marche avec des semelles souples sur terrain plat et irrégulier. Notre contrôleur en boucle fermée minimise les erreurs sur le centre de masse (COM) et le point de moment nul (ZMP) avec un contrôle en admittance des pieds basé sur un estimateur de déformation simplifié. Nous démontrons son efficacité expérimentalement en faisant marcher le robot humanoïde HRP-4 sur des graviers.

Contents

List of Figures	xiii
Nomenclature	xvii
1 Introduction	1
2 Human Walking on unknown soft material	5
2.1 Background	6
2.2 Material and Methods	7
2.2.1 Participants	7
2.2.2 Compliant platform	7
2.2.3 Protocol	8
2.2.4 Data analysis	9
2.3 Results	13
2.3.1 Vertical GRF	13
2.3.2 CoP displacement	14
2.4 Discussion	14
2.5 Conclusion	18
3 A Humanoid Walking Pattern Generator for soft soles	19
3.1 Background	20
3.2 Simplified mechanical model of humanoid robot	20
3.3 ZMP, a stability criteria	21
3.4 Walking pattern generator	23
3.4.1 Optimization criteria	23
3.4.2 Force model	25
3.4.3 Torque model	25
3.4.4 Constraints	26
3.5 ZMP and COM trajectories	28

3.5.1	Global ZMP trajectories	28
3.5.2	Local ZMP trajectories	30
3.5.3	COM trajectories	33
3.6	WPG validation with experiments on HRP-2	35
3.6.1	Walking pattern behaviors	36
3.6.2	Experiments with ankle flexibilities	36
3.6.3	Experiment with flexible sole	38
3.6.4	WPG optimization results	39
3.7	Conclusion	41
4	Soft sole deformation estimator	45
4.1	Problem formulation	46
4.2	Deformation estimator	47
4.2.1	Feet trajectories	47
4.2.2	Soft sole model	48
4.2.3	Frictional contact problem	51
4.2.4	ZMP force and position algorithm	53
4.2.5	Initial conditions	57
4.3	DE validation with experiments on HRP-4	58
4.3.1	Multi-objective quadratic program controller	58
4.3.2	HRP-4 walking with soft sole using the new controller	59
4.3.3	Results	61
4.3.4	Discussion	64
4.4	Conclusion	66
5	A closed-loop controller to walk with soft soles	67
5.1	Control framework structure	68
5.2	ZMP-COM control layer	69
5.2.1	Linear inverted pendulum model	70
5.2.2	Pole placement for ZMP-COM tracking control	71
5.3	ZMP-force distribution layer	73
5.3.1	Optimal force distribution and ZMP placement	73
5.3.2	Satisfaction of ZMP constraints	76
5.3.3	ZMP projection to CoP	77
5.4	Floor reaction force control layer	78
5.5	Experiments	81
5.5.1	Experimental setup	81

Contents	xi
<hr/>	
5.5.2 Robot feedback state estimator	81
5.5.3 Walking on flat floor and gravel	82
5.6 Conclusion	84
6 Conclusion	89
Notes	92
Bibliography	93
Publications	98
Appendix A WPG : QP formulation	99
A.1 Optimization parameters and optimization criteria	99
A.1.1 Optimization parameters	99
A.1.2 Optimization criteria	100
A.2 Force and torque computation	101
A.3 Global ZMP detailed	102
A.4 COM detailed	104
A.5 Ankle position detailed	106
A.6 Local ZMP detailed and force distribution	107
Appendix B Detail of the Frictional contact problem	111
B.1 Signorini's law	111
B.2 Coulomb's law	113
B.3 Gauss-Seidel method for contact handling	115
Résumé en français	117

List of Figures

1.1	Examples of human walking in different environment.	1
1.2	Examples of well-known robot feet.	2
1.3	Examples of CoP trajectory of Human and Humanoid Robot.	3
2.1	Compliant walking platform. The first part was characterized by high (H) ground stiffness, the second part by low (L) ground stiffness.	8
2.2	Example of a walking trial.	9
2.3	ForceShoe system; MTx (orange boxes); F/T sensors (steel grey cylinder) .	10
2.4	VICON markers on ForceShoes	11
2.5	Example of CoP projection on the surface of H under the foot segment f_s (green box) on ground with high (H) stiffness and on low (L) stiffness. . . .	12
2.6	Example of vertical Ground Reaction Forces (GRF) under the foot stepping (a) before and (b) after the transition from hard ground to soft mattress. . .	15
2.7	(a,b) Vertical GRF peak height	16
2.8	Example of CoP projected on plane H before and after the walking transition from H to L.	17
2.9	CoP displacement under the support foot.	17
3.1	Simplified actuation model in sagittal plane at left and cart-table model at right	21
3.2	Support convex hull during DSP.	22
3.3	Example of walking sequences with via-points (o) and ZMP trajectories during SSP (blue) and DSP (red)	29
3.4	ZMP and COM trajectories	37
3.5	Ankle torque with flexible soles and ankle flexibilities	38
3.6	COM acceleration in the swinging direction with flexible soles and ankle flexibilities	39
3.7	Energy needed by left leg to achieve the whole walk	40
3.8	Photo of HRP-2's feet with flexible soles	40

3.9	ZMP and COM trajectories	41
3.10	Examples of a generated walking gait	42
4.1	(a): Rectangular parallelepiped soles mounted on HRP-4's feet; (b): meshed sole with 1494 tetrahedron elements	47
4.2	Control scheme. The ankle reference trajectories change according to sole deformations.	48
4.3	Simple sole shape. O_s is the center of the surface attached to the foot	48
4.4	Contact between the sole and the ground	52
4.5	Framework for contact handling to obtain \mathbf{F}_{ZMP}^d and \mathbf{P}_{ZMP}^d . $t_s - 1$ is the previous time step and $\Psi = [\mathbf{F}_{ZMP} - \mathbf{F}_{ZMP}^d, \mathbf{P}_{ZMP} - \mathbf{P}_{ZMP}^d, \Gamma_{\mathbf{P}_{ZMP},n}]^T$. . .	53
4.6	(a): new HRP-4's feet; (b): photo of HRP-4's feet with flexible soles	59
4.7	(a): ZMP trajectory under the left foot and COM trajectory during the 6 th foot step (SSP+DSP); (b): ankle trajectories when the foot is not in contact with the floor	60
4.8	COM acceleration compared to the reference acceleration along x/y/z axes with and without the deformation estimator (DE).	61
4.9	Norm of horizontal ground reaction forces and the vertical ground reaction forces measured with and without the DE in right foot.	62
4.10	Right ankle position along x/y/z axes in the COM frame.	63
4.11	Ankle orientation along x/y/z axes with and without the DE.	64
4.12	Ankle torque for different cost functions.	65
4.13	COM acceleration for different cost functions.	65
5.1	Different views of HRP-4 walking on gravel with soft soles.	68
5.2	<i>Overview of the control loop.</i> Superscripts d and c denote desired and control references, respectively, while robot measurements have none. $i \in \{R, L\}$ stands for right or left foot. \mathbf{P} refers to positions, \mathbf{F} to forces and Θ to orientations.	69
5.3	<i>ZMP-COM tracking controller:</i> the state reference \mathbf{x}^d of COM velocity, COM and ZMP position is compared to the measured state \mathbf{x} in order to control the system (in red) with a ZMP control \mathbf{x}_{ZMP}^c	73
5.4	Graphical description of the optimal \mathbf{P}_{ZMP_L} and \mathbf{P}_{ZMP_R} in DSP from (5.22). . .	76
5.5	Examples of control ZMP \mathbf{P}_{ZMP}^c projected at the point \mathbf{P}_{ZMP}^s on the edge of the ZMP support area equivalent to the foot shape in contact with the ground (dashed red) in SSP.	77

5.6	Convex hull of ground contact points (dashed red) and reduced ZMP support area (black) in double support phases (DSP) when ZMP-force distribution minimizes ankle torques. The control ZMP \mathbf{P}_{ZMP}^c is projected to \mathbf{P}_{ZMP}^s	78
5.7	Example of CoP projection on ZMP plane.	79
5.8	<i>Reaction force controller</i> : the ZMP $\mathbf{P}_{ZMP_i}^c$ and contact force \mathbf{F}_i^c under the foot i are compared to the robot state \mathbf{P}_{ZMP}^c and \mathbf{F}_i^c in order to control in admittance the robot by generating foot i relative position \mathbf{P}_i^c and orientation Θ_i^c control.	80
5.9	(a): new HRP-4's feet; (b): photo of HRP-4's feet with soft soles	81
5.10	<i>Walking over flat floor and gravel (granulometry: 10/20 mm)</i> : ZMP and COM measured compared with the references along x/y axes during a four steps and 20cm long walk.	83
5.11	<i>Walking over flat floor and gravel (granulometry: 10/20 mm)</i> : Vertical ground reaction forces under each foot measured compared with the references along x/y axes during a four steps and 20cm long walk.	84
5.12	<i>Walking over flat floor and gravel (granulometry: 10/20 mm)</i> : CoP under each foot measured compared with the references along x/y axes during a four steps and 20cm long walk.	86
5.13	<i>Walking over flat floor and gravel (granulometry: 10/20 mm)</i> : COM velocity measured compared with the references along x/y axes during a four steps and 20cm long walk.	87

Nomenclature

Roman Symbols

\mathbf{F} a force vector, $[F^x \ F^y \ F^z]^T$

(fs) denotes the frame fs

g is the gravitational constant = 9.81 m/s²

\mathbf{O}_f Origin of frame f

\mathbf{P} a position coordinate vector, $[x \ y \ z]^T$

q denotes the q^{th} sequence of the walking cycle

S is a surface of the sole

S_D is the surface of the sole that could be in contact with the ground

T_j denotes the ending time of phase j

Greek Symbols

$\partial\Omega$ is exterior surface of Ω

$\mathbf{\Gamma}$ a torque vector, $[\Gamma^x \ \Gamma^y \ \Gamma^z]^T$

Ω is the meshed sole shape

Ω_l is the interior volume of Ω

Θ an orientation vector, $[\tau \ \phi \ \psi]^T$

Superscripts

a is the a -axis coordinate of a 3D vector with $a \in [x, y, z]$

- c denotes the control value generated by the controller
- d denotes the desired value generated by the WPG
- j denotes the j^{th} phases
- l denotes a vector expressed in the sole frame

Subscripts

- D denotes the surface nodes attached to the rigid robot foot
- fs denotes the segment fs
- I denotes the internal nodes of the sole
- i (in chapter 3) denotes the foot $i \in [1, 2]$ where '1' define the foot that leaves the floor at the end of DSP, and '2' define the foot that comes in contact at the beginning of DSP
- i (in chapter 5) denotes the foot $f \in \{R, L\}$ right or left foot references
- S denotes nodes that could be in contact with the ground

Other Symbols

- fs the foot segment $\in [forefoot; rearfoot]$

Acronyms / Abbreviations

- COM Center of mass
- CoP Center of pressure
- DE Deformation Estimator
- DoF Degree of Freedom
- DSP Double support phases
- EMG Electromyographic
- FEM Finite Element Model
- ForceShoe Shoe with a pair of force and torque sensors attached under the sole

F/T Force/Torque

GRF Ground reaction force

H High ground stiffness

L Low ground stiffness

MTx Xsens motion tracker

SSP Single support phases

VICON Motion capture system

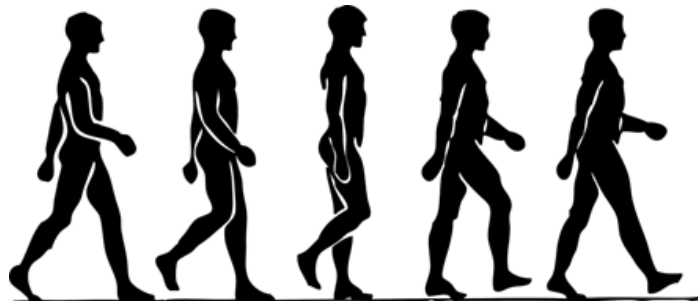
WPG Walking Pattern Generator

ZMP Zero Moment Point

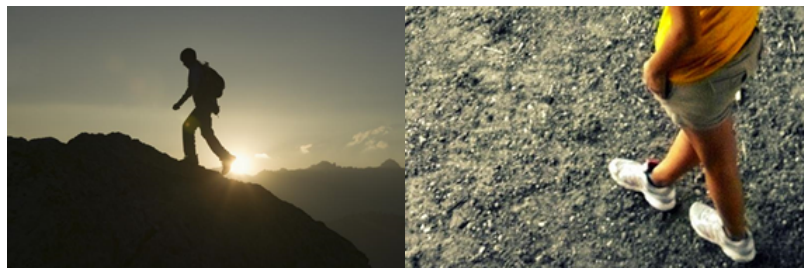
Chapter 1

Introduction

For humans, walking is a natural behavior learned during childhood to move its whole body from one place to another. Bipedal humanoid walking alternates phases of contact creation and breaking with the ground (see Fig. 1.1a). In order to avoid being hurt by the environment, humans have a whole body balance strategy to deal with perturbations. This strategy is backed up by complex adaptive feet that can shape the environment. Such walking control allow humans to walk almost anywhere and cast ground uncertainties during walking like uneven ground (see Fig. 1.1b) or rough terrain with gravels (see Fig. 1.1c).



(a) Snapshot of human walking

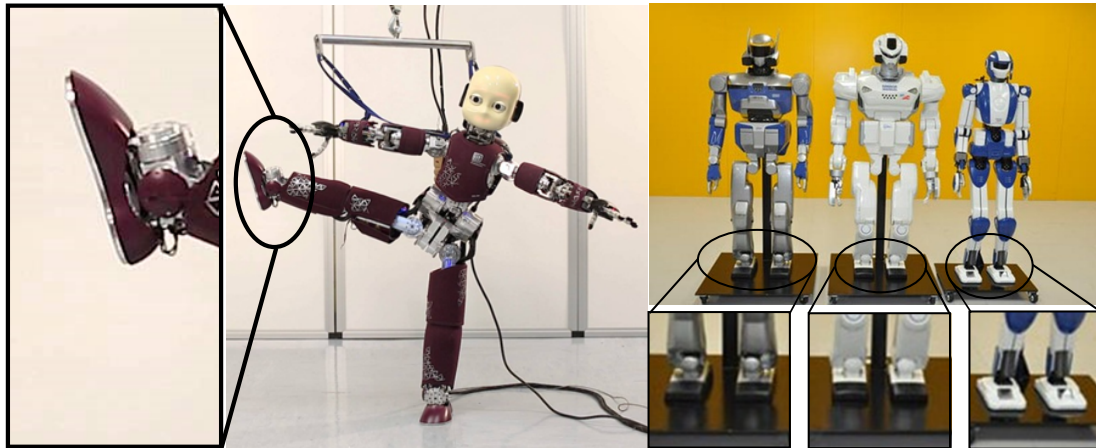


(b) Human walking on mountain

(c) Human walking on gravel

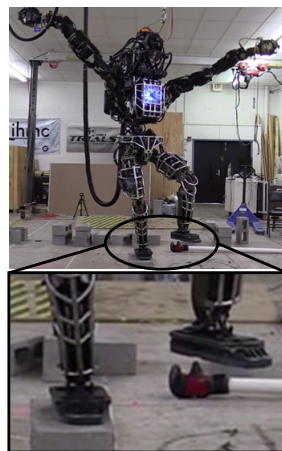
Figure 1.1 Examples of human walking in different environment.

The human living environment has been shaped, optimized and designed for human-size bipedal humanoids. In that way, to help him in its different tasks, humans have naturally decided to build humanoid robots. In a locomotion point of view, biped walkers are the most adaptive to any environment. However, actual humanoid robot have lack of design in the feet. Indeed, most of well-known humanoid robot have flat and rigid feet (see Fig. 1.2).



(a) iCub (RobotCub)

(b) HRP-2, HRP-3 and HRP-4 (Kawada)



(c) Atlas (Boston Dynamics)

Figure 1.2 Examples of well-known robot feet.

In comparison, a simple look at human feet shows:

- an envelop that can change its properties by being soft (to shape little ground irregularities and absorb foot landing impact shock) or stiff (to improve stability)
- two segments (heel and toe) linked by a joint (to increase the foot degrees of freedom).

Such feet allow humans to have an adaptive control of the feet-ground interaction. Indeed, the center of pressure (CoP), which is a sum up of contact points pondered by their respective ground reaction forces, under the foot has a curvative trajectory (see Fig. 1.3a). On the contrary, in humanoid robotics, due to foot design limitations, most commonly generated motion (and by extension CoP) are straight (see Fig. 1.3b).

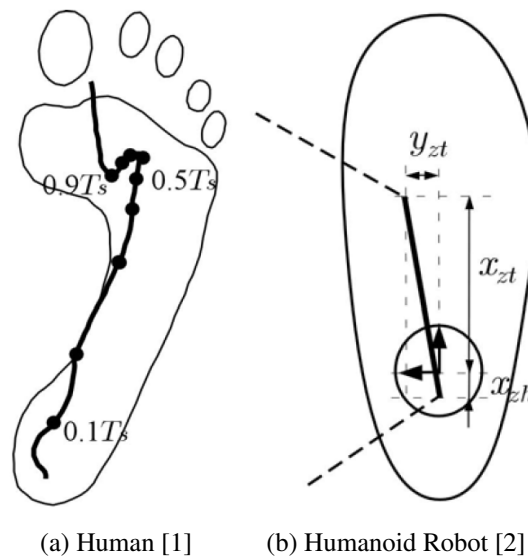


Figure 1.3 Examples of CoP trajectory of Human and Humanoid Robot.

Hence, we point the need to increase the degree of freedom of humanoid robots feet. We chose to investigate adding a thick soft soles under the robots feet in order to:

- increase the foot degrees of freedom with passive sole deformation
- absorb foot landing impact with the inherent properties of thick soft materials
- cast ground unevenness and irregularities.

Because, to date no existing controller generates motion for humanoid robot to walk with soft soles, the question is : *is it possible for humanoid robot to walk with soft soles ?*

In this study, we investigate the use of soft soles to walk. Human has a natural behavior to walk on soft material (feet, shoes, mattress, ...). So we firstly look at human balance strategy (in Chapter 2) to inspire the development of a humanoid robot controller. Then we develop jointly a walking pattern generator (in Chapter 3) to generate the robot motion and a deformation estimator (in Chapter 4) to predict the sole deformation and take it into account in the foot movement to obtain a stable walk. However, due to high computational time, such

method inhibit online motion generation and robot reactivity to perturbations. Hence, we finally design a closed-loop controller (in Chapter 5) based on a simple deformation estimator to online track the reference motion and deal with sole deformations. All these developments are validated by experimental tests on real humanoid robots HRP-2 and HRP-4.

Chapter 2

Human Walking on unknown soft material

Human has a natural behavior to deal with ground uncertainties and unevenness when walking. Hence it was logical to begin to study the human ability to stabilize and recover in order to expand such a method on humanoid robots.

Abstract

Control actions are applied by the central nervous systems to assure dynamic stability when unexpected stiffness changes of the ground surface occur while walking. Many studies in the motor control field have investigated the mechanisms of such a postural control and have widely described how center of mass (COM) trajectories, step patterns and muscle activity adapt to avoid loss of balance. However, much less attention has been given to the role played by the ground reaction forces (GRF).

The aim of this chapter was to examine the ground reaction forces adaption when stepping unexpectedly on a soft, compliant surface. Differently from the classical methods to record ground reaction forces based on the use of force platforms positioned at fix locations along the walking path, here we used special shoes, each one equipped with a pair of force sensors under the sole.

Results showed that when stepping over the soft ground participants actively modulated the ground reaction forces under the supporting foot in order to exploit the elastic and compliant properties of the surface to dampen the impact and to likely dissipate the mechanical energy accumulated during the “fall” onto the new compliant surface. Interestingly, this motor strategy emerged already in the first trial, when participants experienced the transition

for the first time. The results presented in this chapter are helpful for the development of our new controller and improve stability in humanoid robotic locomotion.

2.1 Background

Human locomotion is a complex dynamic process during which one has to continuously exert corrective actions to react to various perturbations to maintain balance and continue walking [3].

Many studies have investigated the adaptive mechanisms underlying the control of posture submitted to expected and unexpected perturbation during several walking tasks such as, for instance, slipping [4], tripping [5] [6] or sudden drop of the support surface [7] [8], [9]. A part of these studies, in particular, has investigated how people react to changes in surface conditions caused by different ground softness. Ferris and colleagues [10] found that runners adjust leg stiffness for their first step over a new surface of different stiffness to assure a smooth transitions between the two surfaces. Marigold and Patla [11] investigated the control of centre of mass (COM), lower limb dynamics and postural response modulation of muscle activity during unexpected walking transitions between surfaces characterized by different compliance properties. The authors found that the recovery response to the first changing softness trial presented muscle onset latencies ranging between 97 and 175 ms (supporting thus evidence for a pre-programmed walking strategy) and muscle activity modulation while on the compliant surface. In addition, they also found significant changes in movement dynamics affecting the COM vertical trajectories, aiming to increase dynamic balance. These results were later confirmed by another study [12] that, in addition, described an increase in step length, step width and stability margin on the anterior-posterior direction on the compliant surface to increase the whole-body base of support and to provide in such a way a more effective control of the COM.

Most of the works reported above investigating recovery responses following changes of ground stiffness during walking or running analysed mainly movement kinematics and electromyographic (EMG) activity, giving less attention to the kinetic aspects of the movement and to the role that the ground reaction forces play in the recovery strategies. Ferris and colleagues [10] recorded the ground reaction forces of runners running continuously on surface characterized by different level of stiffness and reported the global mechanics was similar in the different experimental conditions. It must be remarked that no softness transition occurred during those recording. To our knowledge no other study has reported up to now detail results characterizing ground reaction forces associated with walking transitions between different compliant surfaces. However, some results have been reported in

the context of a similar walking condition, that is when an unexpected loss of ground level occurs. Van Dieën and colleagues [7] first showed that the GRF on the landing leg was much more dominated by the initial impact. The same observations were later confirmed in other two similar studies [8, 9].

Our investigation details more the role of GRF in the recovery of balance when an unexpected change of ground softness occurs and how GRF adapt in the trials following the first, when the softness transition is known. To record GRF under the feet we used a special pair of shoes equipped with a couple of 3D force sensors attached under the sole of each shoe. This allowed us to measure precisely the GRF and the center of pressure (CoP) position under each foot. The use of these force shoes allowed to overcome the intrinsic experimental limitations associated with the more classic use of force platforms, first of all the need of keeping the location of the force platforms fixed during the experiment.

2.2 Material and Methods

2.2.1 Participants

Ten participants (five female and five male; age 27 ± 5 years; mass 70 ± 20 kg; height: 1.69 ± 0.08 m) volunteered for this study. Participants had no muscular, neurological, or joint disorders which would affect their performance in this study. The experiment conformed to the declaration of Helsinki and written informed consent was obtained from all the participants according to the protocol of the local ethical committee (Ethik-kommission an der medizinischen Fakultät der Eberhard-Karls Universität und am Universitätsklinikum Tübingen). The ethic committee had approved this study in advance.

2.2.2 Compliant platform

Participants had to walk on an horizontal platform (6 m long, 2 m wide and 0.3 m deep) characterized by two different levels of ground stiffness (Fig. 2.1). The first part of the walking surface (4 m long, 2 m wide) consisted in an elevated wooden platform characterized by a high value of ground stiffness (H in Fig. 2.1). The second part of the platform (2 m long, 2 m wide, 0.3 m deep) following the wooden part consisted of a soft mattress (L in Fig. 2.1) characterized by a lower value of ground stiffness. The whole platform was covered with a uniform tarpaulin in order to hide the ground transition.

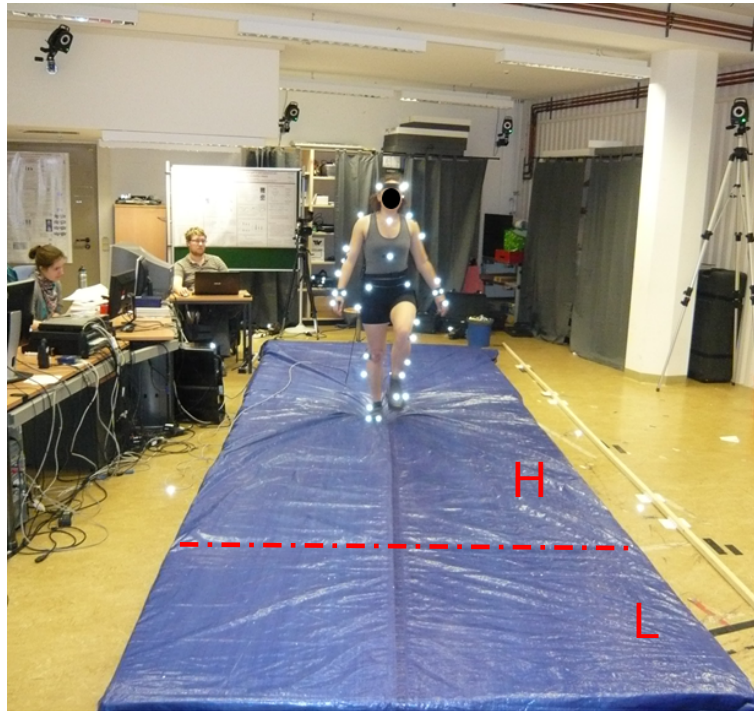


Figure 2.1 Compliant walking platform. The first part was characterized by high (H) ground stiffness, the second part by low (L) ground stiffness.

2.2.3 Protocol

At the beginning of each experimental trial, participants stood on the edge of the platform at the beginning of the H area and faced toward the other end of the platform. After a 'go' signal was verbally provided by the experimenter and data collection had started, participants had to walk at a preferred pace until the other end of the platform, where they had to stop without stepping off it. At the end of each trial participants were asked to go back to the initial position walking on the normal ground and to prepare for the following trial. Each participant accomplished a total of 10 experimental trials. Participants were not aware of the ground softness transition that they would experience. At the end of each trial, before the participant moved back to the initial position, the tarpaulin was pulled from both the lateral sides of the platform to make the whole surface looking flat again to hide in this was any sign of the transition as much as possible. Sample pictures from a typical trial are shown in Fig. 2.2.

Movement kinematics was recorded by means of a (VICON, Oxford, UK) motion capture system with 10 infrared cameras, tracking the positions of 42 reflective markers (2.5 cm diameter) with spatial error below 1.5 mm. The markers were attached with double-sided

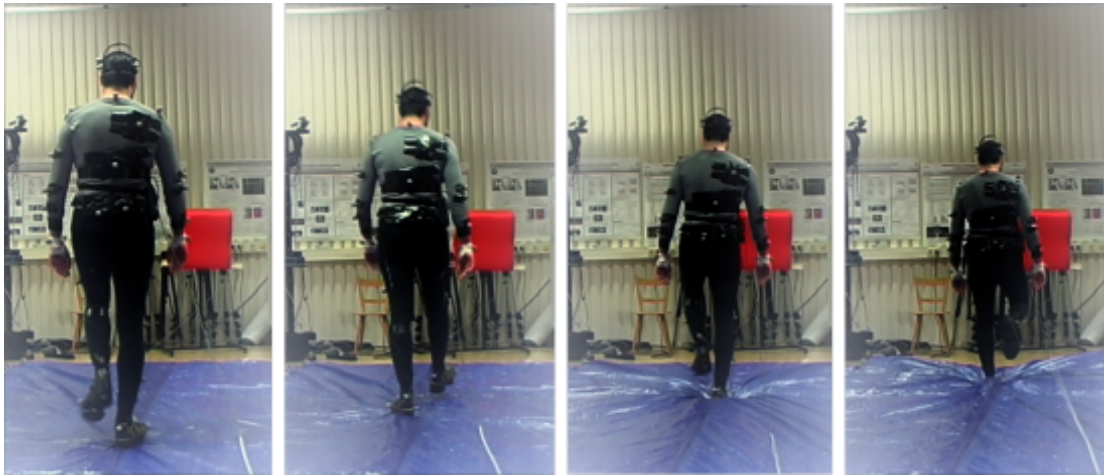


Figure 2.2 Example of a walking trial.

adhesive tape to tight clothing worn by the participants. Markers were placed on the locations specified by the VICONs PlugInGait marker set. Commercial VICON software was used to reconstruct and label the markers and to interpolate short missing parts of the trajectories. Sampling frequency was set at 100 Hz.

Ground Reaction Forces (GRF) were recorded using two special pairs of shoes, called ForceShoe, manufactured by Xsens Technologies B.V. (Enschede, The Netherlands). A picture of one of those shoes can be seen in Fig. 2.3. Shoes had size 40 or 42 (EU). For details on the system please refer to [13]. The ForceShoe consisted of standard orthopedic sandals equipped with two six degrees of freedom force/torque (F/T) sensors (ATI-Mini45-SI-580-20, Schunk GmbH & Co, KG) and two *MTx* (Xsens motion tracker). Each *MTx* consisted in a miniature inertial measurement unit containing linear accelerometers, rate gyroscopes and magnetometers. Sampling frequency was set at 50 Hz and synchronized with the VICON by using a link cable and synchronization pulse. Datas were gathered with MT Manager ForceShoe 1.7.4.

2.2.4 Data analysis

Kinematics data

The positions of the VICON markers on the feet were used to retarget the torques measured by the ForceShoe in the global (VICON) frame of reference. The output of the F/T sensors under the shoes indeed are initially expressed in the local frame of reference of the foot.

First of all, the VICON markers positions are given in a random orientation frame that has to be reoriented in a world frame. To any world frame, a common direction is the vertical



Figure 2.3 ForceShoe system; MTx (orange boxes); F/T sensors (steel grey cylinder)

one. During the experiments, four markers were put on the floor to delimit the platform in three parts. As the floor of the experiments room is horizontal, by using 3 markers on the floor, the vertical direction can be easily obtained with a cross product of two vectors defined by three markers on the floor.

Then, the ForceShoe measurement units, directly gives the vertical direction from the acceleration and gyroscope measures. One of the horizontal direction of the world frame defined by the ForceShoes point the north direction obtained by the magnetometer.

However, VICON doesn't point the north. Hence, VICON and ForceShoe world frame have to be horizontally aligned. To do so, VICON markers on the foot are stuck on the ForceShoe leather straps as shown in Fig. 2.4. Three markers were used for the alignment: (i) over the thumb toe (see Fig. 2.4a), (ii) on the side opposite to the thumb toe and near the little toe (see Fig. 2.4a), and (iii) on the back strap over the heel and behind the ankle (see Fig. 2.4b). Those markers position are known in the ForceShoe frame when the foot is on a flat horizontal floor. Hence, extract the VICON marker positions in the same condition and by using a method of least squares, we obtain the alignment of both frames.

Force data

The orientations of each ForceShoe is provided directly by the two MTx sensors attached to its sole. Similarly, the sensors provide direct information about the gravity direction. The two MTx sensors divide each force shoe in two segment, a forefoot and rearfoot foot segment. In the rest of this paper, we will use the term fs to indicate any of these segments.



Figure 2.4 VICON markers on ForceShoes

The frames of reference attached to each foot segment are centered on the F/T sensors position (\mathbf{O}_{fs}) and oriented in such a way to have two axes (x and y) laying on the flat surface of the sensors and one axis (z) perpendicular to it and direct in the upwards side of the force shoes.

Forces and torques associated with each sensor can be expressed as:

$$\mathbf{F}_{fs} = \begin{pmatrix} F_{fs}^x \\ F_{fs}^y \\ F_{fs}^z \end{pmatrix} \quad \mathbf{\Gamma}_{fs}(\mathbf{O}_{fs}) = \begin{pmatrix} \Gamma_{fs}^x \\ \Gamma_{fs}^y \\ \Gamma_{fs}^z \end{pmatrix} \quad (2.1)$$

where \mathbf{F}_{fs} is the force measured by the force sensor equivalent to the ground reaction forces associated with segment fs in the (fs) frame of reference and $\mathbf{\Gamma}_{fs}(\mathbf{O}_{fs})$ is the torque measured by the torque sensor associated with the same segment in (fs) frame and computed with respect to \mathbf{O}_{fs} .

The CoP is defined as the the point of application of the ground reaction force vector. Based on [14], the CoP of each segment can be computed by solving the following equation:

$$\mathbf{\Gamma}_{fs}(\mathbf{P}_{CoP,fs}) = \mathbf{\Gamma}_{fs}(\mathbf{O}_{fs}) + \mathbf{\Gamma}_{fs}(\mathbf{P}_{CoP,fs}/\mathbf{F}_{fs}) = \mathbf{\Gamma}_{fs}(\mathbf{O}_{fs}) + \overrightarrow{\mathbf{P}_{CoP,fs}\mathbf{O}_{fs}} \times \mathbf{F}_{fs} = 0 \quad (2.2)$$

where $\mathbf{\Gamma}_{fs}(\mathbf{P}_{CoP,fs}/\mathbf{F}_{fs})$ is the torque of the force \mathbf{F}_{fs} computed with respect to its point of measurement \mathbf{O}_{fs} at the CoP position $\mathbf{P}_{CoP,fs}$ of foot segment fs.

Remind that each foot segment is considered as a plane perpendicular to the z-axis of the F/T sensor and at the altitude 0, the CoP position can be obtained as:

$$\mathbf{P}_{\text{CoP},fs} = \begin{pmatrix} -\frac{\Gamma_{fs}^y}{F_{fs}^z} \\ \frac{\Gamma_{fs}^x}{F_{fs}^z} \\ 0 \end{pmatrix}_{(fs)} \quad \Gamma_{fs}(\mathbf{P}_{\text{CoP}}) = \begin{pmatrix} 0 \\ 0 \\ \Gamma_{fs}^z \end{pmatrix}_{(fs)} \quad (2.3)$$

On H, all the ForceShoe segments in contact with the floor are coplanar with the ground surface H. Thus in order to obtain the CoP under the foot, it is easy to move every torques to one common point $\mathbf{O}_0 \in H$:

$$\Gamma(\mathbf{P}_{\text{CoP}}) = \Gamma(\mathbf{O}_0) + \Gamma(\mathbf{P}_{\text{CoP}}/\mathbf{F}_{\text{total}}) \quad (2.4)$$

with

$$\Gamma(\mathbf{O}_0) = \sum_{fs} (\Gamma(\mathbf{O}_{fs}) + \Gamma(\mathbf{O}_0/\mathbf{F}_{fs})) \quad \text{and} \quad \Gamma(\mathbf{P}_{\text{CoP}}/\mathbf{F}_{\text{total}}) = \overrightarrow{\mathbf{P}_{\text{CoP}}\mathbf{O}_0} \times \left(\sum_{fs} \mathbf{F}_{fs} \right)$$

Then the combination of equations (2.3) and (2.4) allows to compute the CoP of the whole body.

On L, all the ForceShoe segments in contact with the soft mattress are not at the same altitude nor in the same orientation. To compare the CoP on H and on L, they have to be in the same horizontal plane. Hence, we chose to project the CoP on L in the horizontal plane H by projecting them along the direction of there respective GRF. Figure 2.5 shows an example of projection of CoP in the plane H.

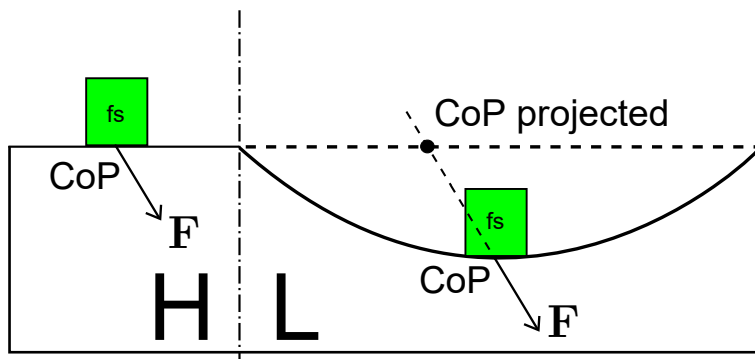


Figure 2.5 Example of CoP projection on the surface of H under the foot segment fs (green box) on ground with high (H) stiffness and on low (L) stiffness.

All reaction forces were normalized with respect to the average vertical gravitational force measured while standing (body mass \times gravity acceleration $g = 9.81 \text{ m/s}^2$).

With the aim of studying the reactive responses to an unexpected change of ground softness and to investigate possible effects of practice on the modulation of the GRF we considered the first, second, fifth and tenth trials for analysis. For each trial, we analyzed the temporal evolution of the vertical component of the GRF associated to the transition step. More specifically we analyzed the GRF under the last foot that, during the walk, struck on the H area of the platform and the first foot that struck on the L area. For each foot we quantified the amplitude of the two main force peaks, one associated with the first strike of the foot on the ground and the second one associated with foot rolling and ankle extension in the last part of the stance phase when the ankle joint is extended to provide forward acceleration to the whole-body to move forward. For each trial and each foot, we also quantified the maximum CoP displacement along the direction of motion. To standardize the displacements of the CoP across subjects, we divided the amplitude of each displacement by the distance between the marker on the right heel of the participants and the marker positioned on the toe of the right ForceShoe.

2.3 Results

All participants successfully walked over the transition without losing their balance. We were particularly interested in examining how participants reacted to the change of ground stiffness during their first experimental trial, when they still were not aware of the transition. However, in order to investigate possible learning effects appearing over the trial, we also analyzed the GRF and CoP displacements of the second, fifth and tenth trial.

2.3.1 Vertical GRF

In Fig. 2.6a is an example of recorded GRF under the foot which last stand on H for one subject. We can observe a classical vertical GRF recordings [15] under the foot during one foot step (a double peak curve). In that case the first and second peak are almost similar. This fact is also showed in Fig. 2.7a which represent the mean GRF peak recorded during the last step on H within all subjects. Over the trials, the first peak height slightly increase when decreasing on the second peak. For its part, the standard deviation of the peak height increase over the trials for both peak.

In Fig. 2.6b is an example of recorded GRF under the foot which first stand on L for one subject. We can still observe a double peak curve but in that case, the first peak is much

higher than the second. This fact is also showed in Fig. 2.7b which represent the mean GRF peak recorded during the first step on L within all subjects. We can also observe that the first peak on L is higher than those on H when the second is lower. Over the trials, the first peak height begin to slightly decrease and increase at the tenth trial when decreasing on the second peak. For its part, the standard deviation of the first peak height (Fig. 2.7a) is lower at the first trial when higher and almost constant during the other. For the second peak, the standard deviation of the peak height (Fig. 2.7a) is decreasing over the trials.

2.3.2 CoP displacement

We computed the CoP under each foot in order to compare their length. Fig. 2.8 shows an example of CoP under each foot before and after the walking transition from H to L. In Fig. 2.9, we can see that the CoP length under the last foot standing on H increases over the trials when almost constant under the first step standing on L. We can also observe that during the two first trials the CoP length is longer on L than on H of almost 10 % while almost similar for the fifth and tenth trials. For its part, the standard deviation of the CoP length on H is almost similar over the trials (around 15 %) while on L, its length is almost twice at the first trial and similar after that.

2.4 Discussion

Walking stability can be threatened in everyday life by various external perturbations such as, for instance, an unexpected change of the mechanical features of the walking surface. The goal of this study was to investigate what motor strategies are commonly used to avoid loss of balance when an unforeseen transition from a hard to a soft surface occurs during locomotion.

Some previous studies investigated already the mechanisms underlying the unexpected transitions on a soft surface. For instance Marigold and Patla [11] found that when stepping on a compliant surface the central nervous system modulates both COM trajectories and EMG activity to maintain dynamic stability. However, our contribution in this study is to characterize such a walking transition analyzing systematically the GRF and CoP displacements under the feet.

Our results suggested that participants might take into account of the mechanical properties of the soft surface to counteract the unexpected perturbation. Indeed, no participant lost balance during transition from H to L. It can be a fusion of balance strategies from natural walking and a direct identification of ground property.

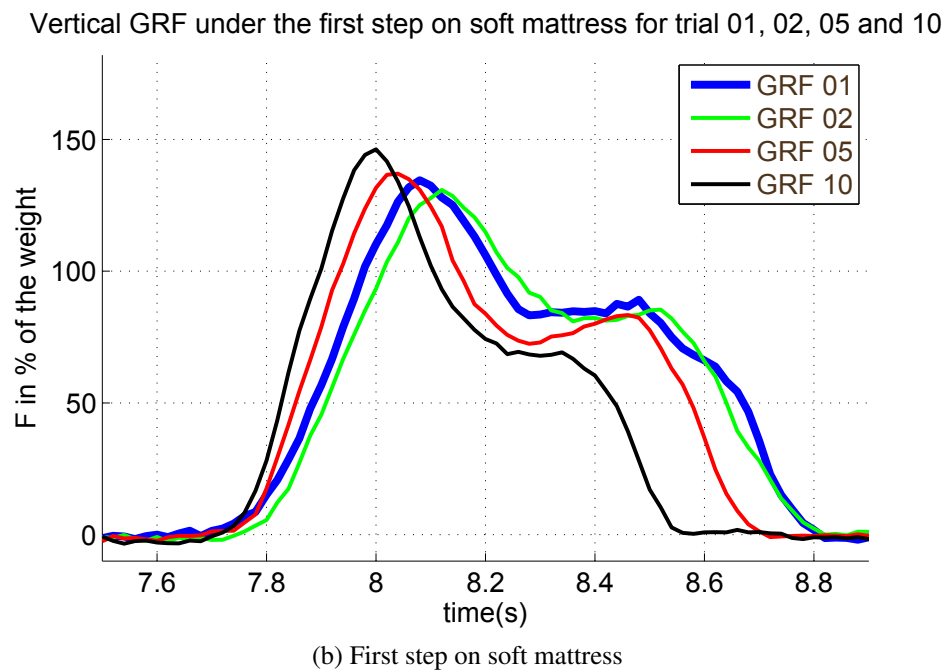
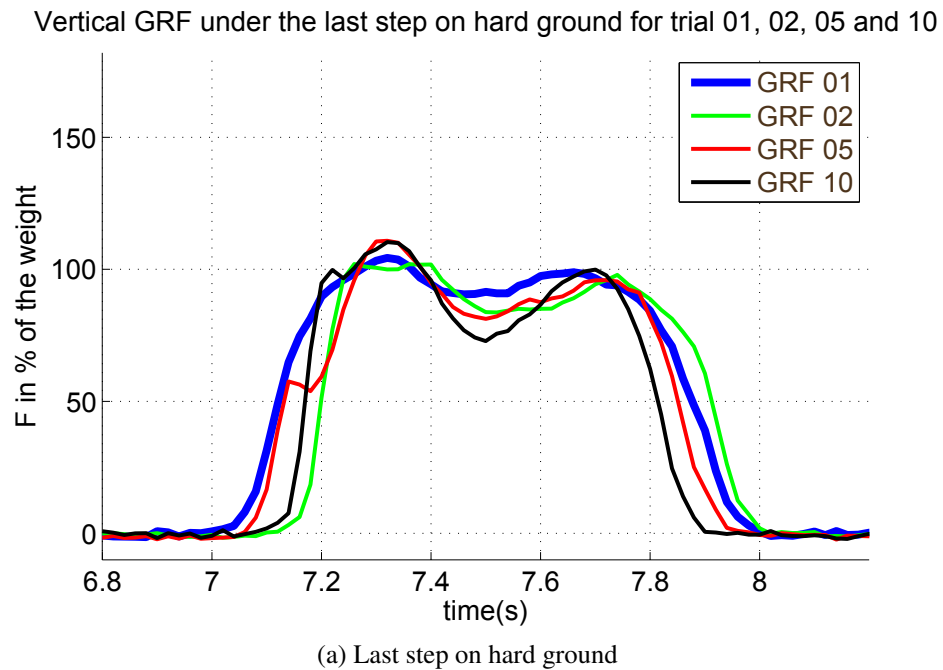
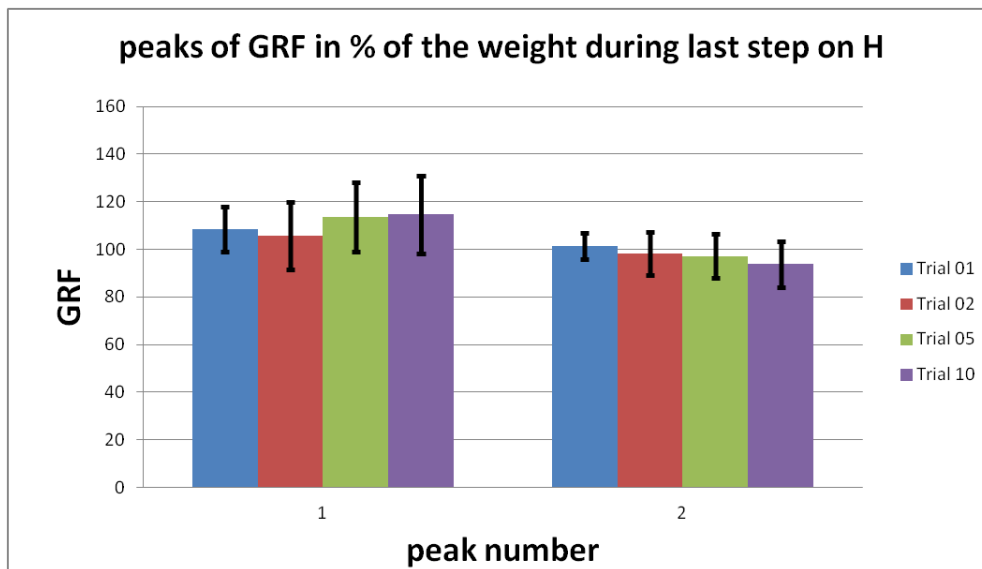
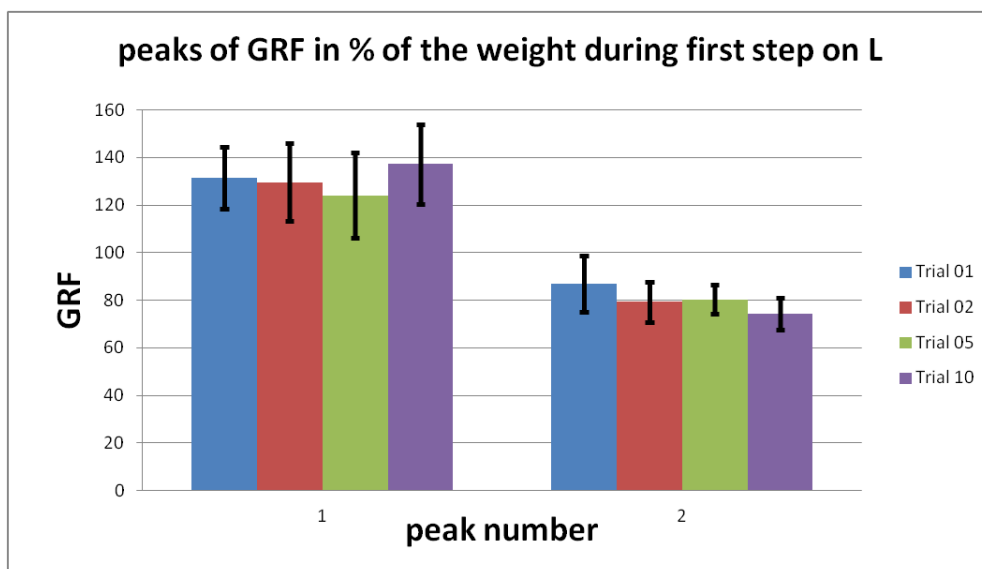


Figure 2.6 Example of vertical Ground Reaction Forces (GRF) under the foot stepping (a) before and (b) after the transition from hard ground to soft mattress.

The increased amplitude of the first GRF peak under the foot on the soft surface can be explained with an increase of COM vertical acceleration due to the longer vertical distance covered by the COM when "falling" onto the soft surface. Similarly to us, von Dieën and



(a) Last step on hard ground



(b) First step on soft mattress

Figure 2.7 (a,b) Vertical GRF peak height

colleagues [7] described that, when an unexpected change of ground level occurs, GRF on the landing lag are mainly dominated by the initial impact on the lower ground.

However, we found that the second GRF peak on the soft surface was smaller than the second peak under the foot on the hard surface. This result can be put in parallel with the longer CoP horizontal displacement under the foot on the soft surface than under the one

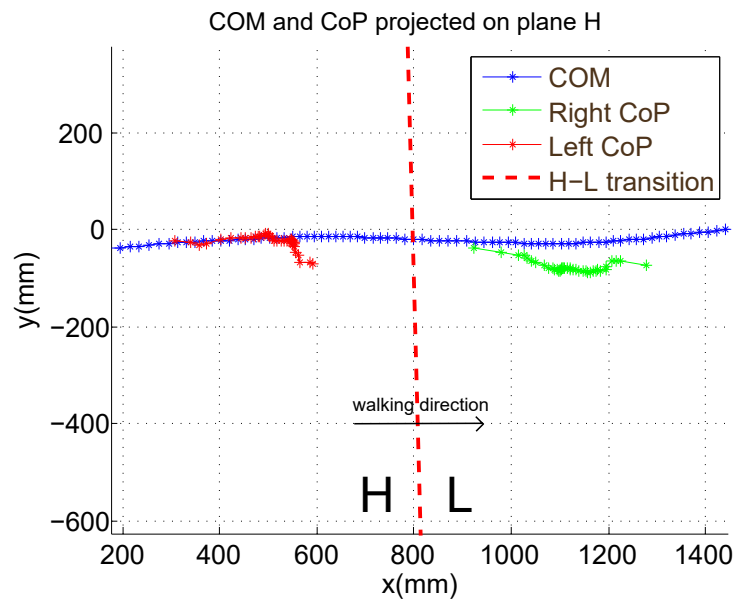


Figure 2.8 Example of CoP projected on plane H before and after the walking transition from H to L.

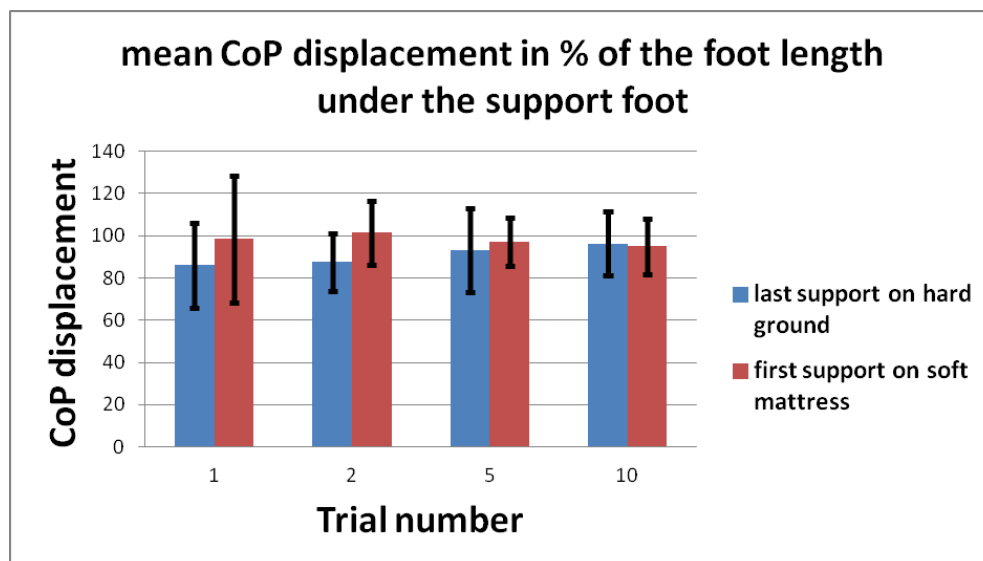


Figure 2.9 CoP displacement under the support foot.

on the hard surface. These results could be a joint effect of bumping on the mattress when falling and a longer contact with the mattress induced by the deformation.

Very interestingly we found also that the responsive behavior described above occurred already during the first trial, when participants were still not aware of the transition, and it

was tuned during the subsequent trials (the amplitude of the second peak on the soft was decreasing with practice). At the contrary we did not find any effect of practice on the GRF under the feet on the hard surface. When the participants start on H, the ground properties are known or predicted as known which induce that the walking is already optimal with less adaptation to occur. On the contrary, when switching to L, the deformable ground properties are unknown but can be pre-evaluated from previous real-life experiments and then identified to tune the control strategy. These findings together suggest a possible tune of control strategy at the time of the transition. Although any interpretation of the changes underlying the control of locomotion during the transition is delicate. However, it can be speculated that the control "gains" changes when ground stiffness changes. Hence, we can interpret those changes as the correction of postural response to assure dynamic stability elicited by the afferent feedback information.

2.5 Conclusion

In this chapter we provided interesting experimental evidences regarding the possible strategies that people adopt when unexpectedly stepping onto a soft surface to preserve dynamic stability and avoid loss of balance. Although additional analysis are needed to understand better all the mechanics of the transition, our results show that participants modulate the GRF to likely dampen the acceleration that the whole-body COM gain because of the transition on the soft surface.

The results reported in this chapter are interesting and provide experimental evidences on the modulation of the GRF and of the CoP under the feet when a surface transition occurs. In humanoid robotics, we chose to extend and adapt those results for the whole walk. In addition, to cast ground unevenness and absorb shock we chose to thick soft soles under the robots feet. With a larger point of view, the control strategy with such soles is close to the walk on mattress (with a lower deformation coefficient). In order to walk with such soles, we develop in Chapter 3 a walking pattern that takes into account the ZMPs under each foot (equivalent to CoPs on flat floor) and ground reaction force distribution. In Chapter 4, we develop an open-loop controller based on a deformation estimation of the soft soles on flat ground equivalent to a walk with known and predictable ground property. Finally, we devise in Chapter 5 a closed-loop control strategy to keep the robot balance which take into account the sole deformation in order to correct the motion errors inspired by the human balance strategy.

Chapter 3

A Humanoid Walking Pattern Generator for soft soles

In Chapter 2, we pointed that human strategy to balance on soft surface combines the control of center of pressure (CoP) and ground reaction force (GRF) under each foot. In order to extend this observation to humanoid robotics walking with soft soles, we need to generate the motion by taking into account those parameters.

Abstract

In this chapter, a new walking pattern generator (WPG) [16, 17] is devised based on a minimization of the energy consumption of a linear inverted pendulum model of humanoid robots. The optimization problem is designed to be quadratic in order to be solved by a QP solver and with optimization parameters that offers the necessary parameters and constraints in order to manage soft soles problems. All components of the cost function are linear functions of zero moment point (ZMP), initial and final COM state, foot step positions and local ZMP under each foot during the double support phases.

This pattern generator is implemented in two sets of experiments implying the HRP-2 humanoid robot: walking with different weighting between (i) the center of mass forces, and (ii) torques applied at the ankle joint. Two types of feet are also considered: the HRP-2 built-in flexible ankle, and a proposed solution that keeps the ankle-to-foot without flexibility and add instead a flexible sole. The latter shows several benefits that are discussed.

3.1 Background

Bipedal walking on regular grounds is a well-documented and thoroughly studied problem in the humanoid robotics research. An excellent synthesized review is presented in [18]. Recent studies show this maturity level for humanoid walking on flat floor. For example, walking with human-in-loop [19], walking with human stylized gaits [20][21] or walking with emotional behavior gaits [22]. In the latter works, the precise control at the interface between the humanoid robot and the sole (ground) plays an important role. For example, reducing impacts and having smooth walking is critical and different studies showed the importance of the foot shape design [23][24].

Comparing to humans, the humanoid robots must compensate as much as possible: (i) the limited number of degree-of-freedom; (ii) their rigid mechanical design unlike the compliance found in human joints and links; and (iii) the robust (implicit) control of the feet-ground interaction (contact). The use of soft soles can help dealing with those limitations. In fact, a well-designed soft sole may include as much as possible the missing ingredients as far as their effects can be projected in the contact operational space. Therefore, human joint/link compliance effect has a projected equivalence in the operational space that can be embedded with soft soles.

However, in order to use soft soles and take into account their deformation, integrating existing walking pattern generators (WPG) is not straightforward. Since we will model the sole deformation in quasi-static in Chapter 4, the orientation of the foot is directly linked to the ZMP of the foot and the sole's shape. Among other technical reasons required by the use of flexible soles (i) we must manage a ZMP under each foot, especially in the double support phase, and (ii) we must have a smooth ZMP to get a smooth foot orientation. To date, no existing WPG fulfills such requirements. Our WPG integrates the latter issues as a QP with an energy criteria to save computational time. We assess our WPG with walking experiments involving the HRP-2 robot having either ankle flexibility or simple flexible soles.

3.2 Simplified mechanical model of humanoid robot

If we look at a humanoid robot like HRP-2, we have a mechanical system with 42 degrees of freedom (DoF). Such system is complex to control and command. To reduce the complexity, a first approximation is taken by fixing the arm and chest joints to obtain a reduced system with 6 DoF into each leg and a point-mass at the COM. With a second approximation, we consider only the ankle joints which reduce the system with 2 DoF in rotation along \vec{x} and

\vec{y} when the foot is on the ground. As a last approximation, we want to control the COM height with respect to the ground. Hence, we consider a prismatic joint along the leg.

With these approximations, we obtain an inverse pendulum model with a controlled length represented in Fig. 3.1a. Such a model is detailed by Kajita *et al.* [25].

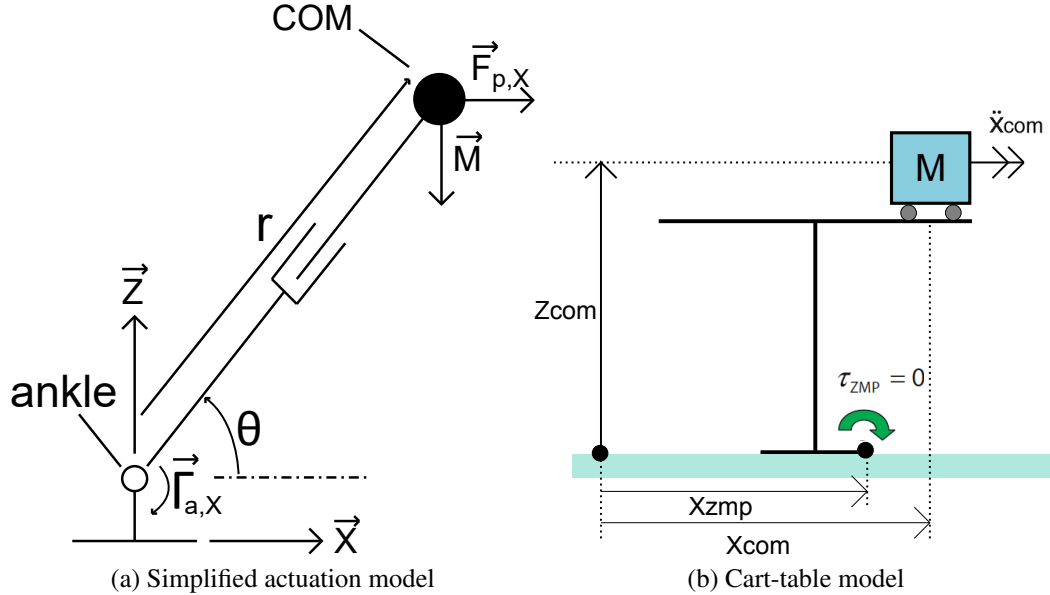


Figure 3.1 Simplified actuation model in sagittal plane at left and cart-table model at right

By convention, the \vec{x} axis is along the direction in front of the robot and the \vec{y} axis is the direction lateral to the robot. The \vec{z} axis is the direction normal to the ground. In addition, the sagittal plane is the plane containing \vec{x} and \vec{z} axis when the frontal plane contain \vec{y} and \vec{z} axis.

With such robot model, the control is realized in a similar way along the frontal and sagittal plane. Thus the computation development will be the same along \vec{x} and \vec{y} axis.

A last simplification is made during the robot motion. The COM height is considered as constant during the whole walking cycle. In that case, we obtain a linear cart-table model used to generate the robot movements. See Fig. 3.1b.

For the rest of this study, we will only develop computation along \vec{x} axis because they can easily be extended to \vec{y} axis.

3.3 ZMP, a stability criteria

Biped robots do their locomotion relatively to floor while keeping their balance and not falling down. They move by using alternately their foot as only contact area to the floor

(called single support phases or SSP) with transition phases to switch from one to the other with both feet on the floor (called double support phases or DSP).

The gait planning and control of biped robots are difficult because there is no base link fixed and the CoP of each support area are not continuous on the floor. The Zero Moment Point (ZMP) is usually used as a dynamic criterion for gait planning and control of biped robots for dynamic stable walking. Vukobratovich *et al.* originally proposed ZMP concept [26, 27] and presented a method of controlling ZMP by adding a compensation input to a leg's joint. Based on ZMP concept, numerous gait planning and control methods were developed.

To simplify, the ZMP is the projection of the CoP into one plane along the direction of the GRF. On flat ground, the ZMP is equivalent to the CoP. During SSP, the ZMP is equivalent to the CoP of the contact foot on the ground and during DSP, the ZMP is the CoP of the total GRF applied to the whole robot (barycenter of the CoP under each foot pondered by their respective GRF). And if the ZMP is inside the support convex hull, the robot is considered stable during walking.

During SSP, the support convex hull is the area under the foot in contact with the floor and during DSP, the support convex hull includes the support foot areas and the area in between. See Fig. 3.2.

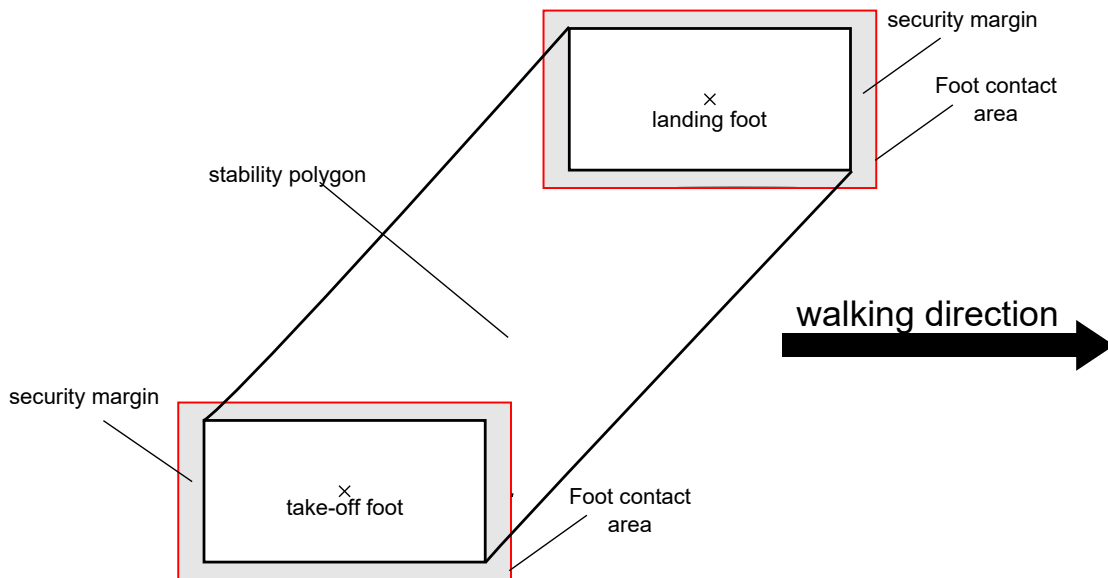


Figure 3.2 Support convex hull during DSP.

The WPG in this study is ZMP based and cart-table model [28] based to link the ZMP with the robot COM. From the cart-table model [25], we obtain a relation between the ZMP

and the COM:

$$x_{ZMP} = x_{COM} - \frac{z_{COM} - z_{ZMP}}{g} \ddot{x}_{COM} \quad (3.1)$$

where x_{ZMP} is the coordinate of the ZMP along \vec{x} axis, g the gravitationnal constant and \ddot{x}_{COM} is the acceleration of the COM along \vec{x} axis.

3.4 Walking pattern generator

To formulate a WPG to be used with soft soles and take into account the deformation, coherent choices are to be made for: (i) the model used, which allows to compute the criteria from the parameters, (ii) the criteria to optimize, and (iii) the parameters defining in which space optimal solutions are to be searched.

There are several works that formulate walking gaits as optimization problems, e.g. [29, 28, 30]. Almost all use an inverted pendulum model with a point mass. Wieber *et al.* [29] compute smooth zero moment point (ZMP) and center of mass (COM) trajectories by minimizing the jerk of the COM. In [30] a similar criterion is used, but the number of steps and walking speed that minimize energy consumption are considered. The approach in [28] generates stable walking gaits by bringing the ZMP close to ankle positions.

In most cases, human try to optimize the whole body movement in order to minimize the fatigue. Thus we naturally choose to base our optimization criteria on this observation. They are based on energy criteria inspired by human [3][31].

During the generation of ZMP and COM trajectories, we will try to minimize the energy consumed by the actuators to move the robot.

As explained before, walking is split in two phases: (i) a single support phase (SSP), with one foot on the floor, and (ii) a double support phase (DSP), where both feet touch the floor. During the DSP, we note with subscript '1' the foot that leaves the floor at the end of DSP, and with subscript '2', the foot that comes in contact at the beginning of DSP.

3.4.1 Optimization criteria

We want to generate walking gaits that minimize the energy consumption E :

$$\min. (E) \quad (3.2)$$

From [30], the energy consumption that accounts for the motor and the gear models can be expressed as:

$$E = \sum_j \int_{t_i}^{t_f} (a_j \tau_j^2 + b_j \tau_j \dot{q}_j + c_j \dot{q}_j^2) dt \quad (3.3)$$

where τ_j is the force/torque, \dot{q}_j is the joint j velocity, and a_j , b_j , c_j are the coefficients depending on joint j motor parameters and gear ratio.

Using the simplified robot model in Fig. 3.1a, Eq. (3.3) becomes:

$$E = \int_{t_i}^{t_f} (a_p F_p^2 + b_p F_p \dot{r} + c_p \dot{r}^2 + a_a \Gamma_a^2 + b_a \Gamma_a \dot{\theta} + c_a \dot{\theta}^2) dt \quad (3.4)$$

where subscript p denotes the prismatic joint and a the ankle joint, F_p is the prismatic force, \dot{r} is the prismatic velocity, Γ_a is the ankle torque and $\dot{\theta}$ is the ankle velocity.

In order to save computational time when solving such minimization problem, we chose to use a QP solver by expressing the criterion components as linear function of the optimization variables. In the energy criterion (3.4), except Γ_a and F_p , the $\dot{\theta}$ and \dot{r} are nonlinear functions of the COM and the ZMP. To keep a quadratic criterion, only the terms Γ_a^2 and F_p^2 are kept. The term F_p^2 is equal to $\mathbf{F}_{\text{COM}}^2$, where \mathbf{F}_{COM} is the force acting on the COM. Finally for a 3D pendulum, Γ_a^2 is replaced by $\|\mathbf{\Gamma}_a(t)\|^2$ and $\mathbf{F}_{\text{COM}}^2$ by $\|\mathbf{F}_{\text{COM}}(t)\|^2$. Therefore Eq. (3.4) becomes:

$$\begin{aligned} E = & \lambda \int_{t_i}^{t_f} \|\mathbf{F}_{\text{COM}}(t)\|^2 dt + (1 - \lambda) \int_{\text{SSP}} \|\mathbf{\Gamma}_{a_{\text{SSP}}}(t)\|^2 dt \\ & + \frac{1}{2} (1 - \lambda) \int_{\text{DSP}} (\|\mathbf{\Gamma}_{a_1}(t)\|^2 + \|\mathbf{\Gamma}_{a_2}(t)\|^2) dt \\ & + \mu \int_{\text{DSP}} (\|\ddot{\mathbf{P}}_{\text{ZMP}_1}(t)\|^2 + \|\ddot{\mathbf{P}}_{\text{ZMP}_2}(t)\|^2) dt \end{aligned} \quad (3.5)$$

where λ and μ are the weights of each criterion; a_{SSP} denotes the ankle of the support foot in SSP; a_i refers to the ankle of the foot $i \in [1, 2]$ in DSP; $\mathbf{P}_{\text{ZMP}} = [x_{\text{ZMP}} \ y_{\text{ZMP}} \ z_{\text{ZMP}}]^T$ are the ZMP coordinates. Since motor characteristics of the simplified model of Fig. 3.1a are not known, we did not know how to choose these two weights. Therefore, experiments on a real robot were used to determine the weights so that our criterion is the best to minimize total walking energy consumption.

This criterion is interesting since by taking $\lambda = 1$ we obtained a walking pattern close to [29, 30]; while taking $\lambda = 0$ we found a solution with ZMP close to ankle like in [28]. Intermediate values of λ give compromises between the two approaches.

In equation (3.5), the new term in factor with μ does not come from previous energy consumption. From the pure energy consumption, ZMP_i are only linked to the minimization of ankle torques which result into oscillating ZMP from toe-heel-toe-heel (see Fig. 3.4b with $\mu = 0$) which is far from the heel-toe human like ZMP trajectory. Inspired by term related to

the minimization of COM force equivalent to the minimization of COM acceleration, we define this term to obtain heel-toe ZMP trajectory in the direction of the walk (see Fig. 3.4b with $\mu = 15$). This term can also be seen as an energy if we consider the link between the foot rotation and the ZMP_i position under the foot detailed in Chapter 4.

All terms of (3.5) are analytically detailed in the latter sections. The linear matrix formulation used to obtain the QP formulation of the problem are detailed in Appendix A.

3.4.2 Force model

As seen previously in 3.2, the COM forces need to be known. By isolating the simple robot model and from the Newton's law, the robot is only affected by two forces: the COM forces and the GRF at the ZMP. As a dynamic solid with two forces, they are equal and opposed along the direction between their points of application.

The point of application of the COM forces is the COM and the one of the GRF is the ZMP.

As explained in section 3.2, during walking, the robot keeps its COM at a constant height. In addition the only force along \vec{z} axis applied on the COM is its weight $-mg\vec{z}$.

From the Newton's law and the zmp equation (3.1), the COM forces are known and defined as:

$$\mathbf{F}_{\text{COM}} = -\mathbf{F}_{\text{ZMP}} = M(\ddot{\mathbf{P}}_{\text{COM}} - \vec{g}) = -\frac{Mg}{z_{\text{COM}} - z_{\text{ZMP}}}(\mathbf{P}_{\text{ZMP}} - \mathbf{P}_{\text{COM}}) \quad (3.6)$$

where \mathbf{P}_{ZMP} is the ZMP position vector, \mathbf{P}_{COM} is the COM position vector and M is the robot mass. Since the COM and ZMP height are constant, \mathbf{F}_{COM} is constant along \vec{z} axis.

As ZMP and COM positions are necessary to compute COM forces, their model will be developed later in section 3.5 and their computation in section 4.

3.4.3 Torque model

The walking cycle alternates between the two phases: SSP and DSP. During SSP, the robot has only one foot in contact with the floor as support whereas it has two feet as support on the floor in DSP. We choose to differentiate the torques computation in ankle during both phase types.

Torques in SSP

During SSP, one foot is in contact with the floor when the other is in the air moving to its next support position. During this phase, the torques in the moving ankle is null. Thus remain the torques in ankle of the supporting foot.

By isolating the support foot, from the Newton's law and assuming that it doesn't slip on the floor during the whole SSP, we obtain:

$$\mathbf{\Gamma}_{a_{SSP}} = \mathbf{F}_{COM} \times (\mathbf{P}_{a_{SSP}} - \mathbf{P}_{ZMP}) \quad (3.7)$$

where $\mathbf{\Gamma}_{a_{SSP}}$ is the torques of the support foot and computed with respect to the ankle position, $\mathbf{P}_{a_{SSP}}$ is the ankle position and \mathbf{P}_{ZMP} is the ZMP position equivalent to the CoP on the ground.

From section 3.4.2, COM and ZMP are necessary to compute torques in ankle.

Torques in DSP

During DSP, the robot has its two feet in contact with the ground and the GRF under each foot will induce torques. The subscript '1' denotes the foot that take off the floor at the end of DSP, and the subscript '2' denotes the foot that strike and land on the floor at the beginning of DSP.

By isolating the each foot, from the Newton's law and assuming that they don't slip on the floor during the whole DSP, we obtain:

$$\mathbf{\Gamma}_{a_1}(t) = \mathbf{F}_1(t) \times (\mathbf{P}_{a_1}(t) - \mathbf{P}_{ZMP_1}(t)) \quad (3.8)$$

$$\mathbf{\Gamma}_{a_2}(t) = \mathbf{F}_2(t) \times (\mathbf{P}_{a_2}(t) - \mathbf{P}_{ZMP_2}(t)) \quad (3.9)$$

where $\mathbf{\Gamma}_{a_i}$ is the torques of the foot i and computed with respect to the ankle i position, \mathbf{F}_i is the GRF under foot i , \mathbf{P}_{a_i} is the ankle i position and \mathbf{P}_{ZMP_i} is the ZMP position under foot i equivalent to the CoP of foot i on flat ground.

To compute the torques during DSP, ZMP_i positions and GRF under each foot need to be known.

3.4.4 Constraints

The problem that we solve is:

$$\begin{cases} \min_X (E) \\ \text{subject to equality and inequality constraints} \end{cases} \quad (3.10)$$

where the criteria E comes from (3.5) and it is based on a simplification of the energy consumption, and the optimization variables X include the ZMP limit conditions, the COM initial and final conditions and the feet positions (A.3).

The inequality constraints are:

1. $ZMP \in$ the convex hull during the SSP
2. ZMP_1 and $ZMP_2 \in$ the convex hull during the DSP
3. Maximum and minimum foot step stretching distance

The equality constraints are:

1. Initial robot state as condition on the first via-point of ZMP and ZMP_1 and on the initial condition of the COM.
2. Final condition on the COM as a goal to reach or condition on the COM over the whole walk (e.g. COM velocity...) (*optional*)
3. Final robot state as condition on the last via-point of ZMP and ZMP_1 (*optional, e.g. used to constraint the final robot acceleration if the final COM is defined and foot orientation when taking into account the sole deformation*)
4. Foot step placement (*optional, e.g. used to define a specific path...*)

We imposed:

- Initial and final feet positions
- Initial and final position, speed and acceleration of the ZMP
- SSP and DSP duration
- COM height
- Foot step directions. It can be changed to define the rotation during walking
- Foot step positions. It is *optional* and define a specific walking path

The two first inequalities are used to generate feasible trajectories. Such criteria is fulfilled by constraining the ZMP trajectories inside the support convex hull [32]. During the SSP, this condition is linear and can directly be integrated as inequality constraints into a QP. During the DSP, this condition is not linear [29] if foot placements are parameters of the optimization. However, if ZMP_1 and ZMP_2 trajectories are in the support convex hull defined by the areas

of each foot, the stability condition for the ZMP trajectories is fulfilled. Therefore, these conditions are linear and can also directly be integrated in a QP optimization.

Based on human walking results in [31] and for ensuring safe walking w.r.t the robot lack of precision [28], we defined a feet support areas within a security margin of 5 – 10% of the foot length.

To avoid self-collisions, we defined a minimal distance between the robot feet (3 cm) and to avoid stretched legs' singularity, we chose a maximum step length (30 cm).

The boundary conditions for the COM velocity (3.26) and (3.30) could not be satisfied at the low level in the equation system (3.31). In order to respect those conditions, we added them as equality constraint to the optimization.

3.5 ZMP and COM trajectories

Our objective is to obtain smooth variations of the foot/ankle orientations of the control framework of Fig. 4.2. Since the orientation of the foot is directly linked to the zero moment point (ZMP) position (See eq. (4.13)), we need smooth ZMP trajectories to obtain smooth feet orientations in Chapter 4.

Several works formulate walking gaits as an optimization problem [28–30]. Almost all use an inverted pendulum model with a point mass and study the global ZMP. Herdt *et al.* [29] compute smooth ZMP and COM trajectories by minimizing the COM jerk. Shin *et al.* [30] minimize the energy consumption changing number of steps and walking speed. Kajita and Espiau [28] generate stable walking gaits by bringing the ZMP close to ankle positions.

To compute the ZMP and COM trajectories, we used the cart-table model (3.1), where the COM trajectory is defined as a 5th order polynomial function (minimum jerk invariant theory). Based on [33] and [34], modeling the ZMP trajectories by polynomials of a given degree α and solving (3.1), result in a COM trajectory with the polynomial part having the same order α . Therefore, we define the ZMP trajectory as a smooth 5th order polynomial.

For the remainder of this chapter, we denote with subscript '1' the foot that leaves the floor at the end of DSP, and with subscript '2' the foot that comes in contact at the beginning of DSP.

3.5.1 Global ZMP trajectories

The walking is defined in three sequences:

1. *Starting sequence*: the robot begins with a DSP. This sequence starts on the point ZMP_{initial} and is cut into two 'half DSP' to increase the DoF of the ZMP trajectory.
2. *Walking sequences*: the robot does n steps. Each step is a sequence of three consecutive parts of phases: 'half SSP' \rightarrow 'DSP' \rightarrow 'half SSP'.
3. *Stopping sequence*: the robot ends with a DSP. This sequence ends on the point ZMP_{final} and is cut into two 'half DSP' to increase the DoF of the ZMP trajectory.

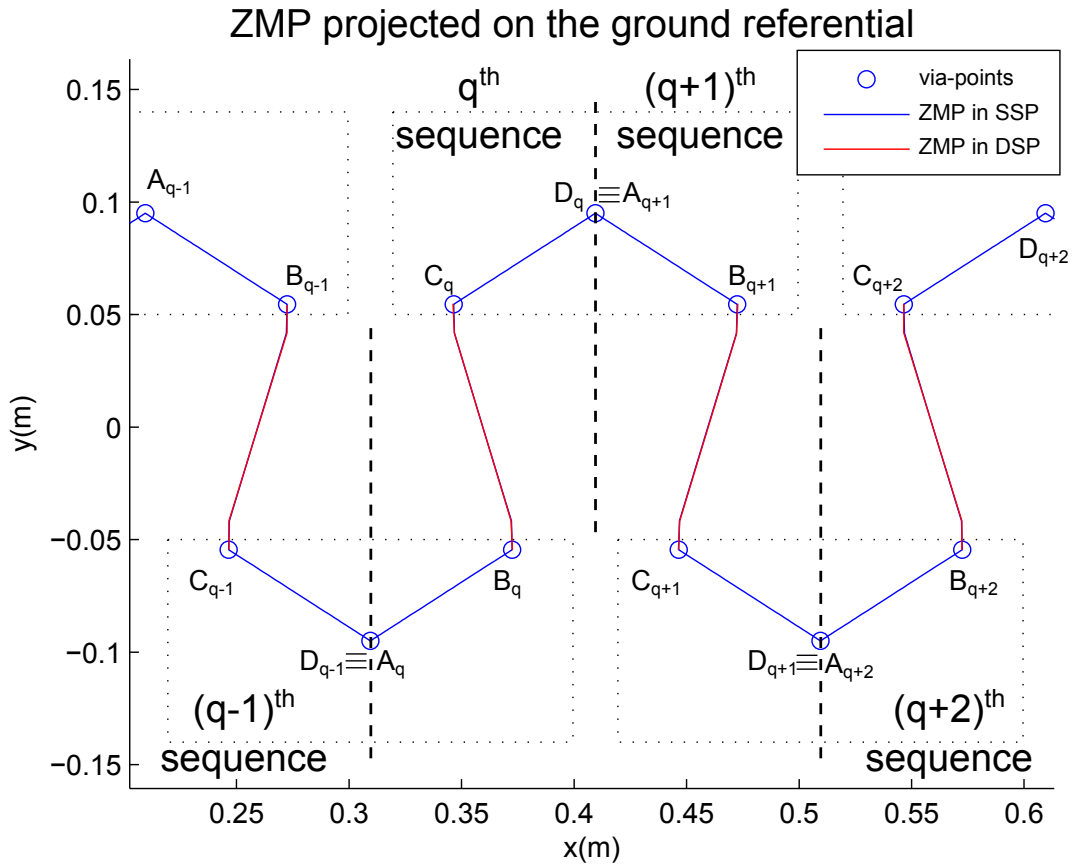


Figure 3.3 Example of walking sequences with via-points (o) and ZMP trajectories during SSP (blue) and DSP (red)

Each *walking sequence* is defined as two 'half SSP' and one 'DSP'. Four via-points are defined to parametrize each duration of these phases, see Fig. 3.3. For a given walking sequence $q \in [1 \cdots n]$, we have:

- The first 'half SSP' goes from via-point A_q to B_q .
- The DSP' goes from via-point B_q to C_q .

- The last ‘half SSP’ goes from via-point C_q to D_q .

Based on these walking gait sequences, we need $m = 3n + 2$ polynomials to model the whole ZMP trajectory, each of which writes:

$$x_{\text{ZMP}}^{(j)}(t) = \sum_{i=0}^5 c_i^{(j)} (\Delta t_j)^i = c_5^{(j)} \Delta t_j^5 + c_4^{(j)} \Delta t_j^4 + c_3^{(j)} \Delta t_j^3 + c_2^{(j)} \Delta t_j^2 + c_1^{(j)} \Delta t_j^1 + c_0^{(j)} \Delta t_j^0 \quad (3.11)$$

where the superscript $j \in [1 \dots m]$ denotes the j^{th} phases and c_i is the i^{th} polynomial coefficient. In (3.11) $\Delta t_j = t - T_{j-1}$, where T_{j-1} is the ending time of phase $j - 1$.

To find the polynomial coefficients of (3.11) and obtain smoother trajectories, we enforced the boundary conditions in position, speed and acceleration at each via-point.

To obtain the polynomial functions of the ZMP trajectory, we interpolated them between $\text{ZMP}_{\text{initial}} \rightarrow C_1$ during *starting sequence*, $A_q \rightarrow B_q$, $B_q \rightarrow C_q$ and $C_q \rightarrow D_q$ during the *walking sequence* q and $B_{n+2} \rightarrow \text{ZMP}_{\text{final}}$ during *stopping sequence*. In our ZMP trajectory definition, C_1 is equal to A_2 , D_q to A_{q+1} and D_{n+1} to B_{n+2} . $\text{ZMP}_{\text{initial}}$ and $\text{ZMP}_{\text{final}}$ are not necessarily equal to B_1 and C_{n+2} respectively.

3.5.2 Local ZMP trajectories

During DSP, both robot’s foot are in contact with the floor with its own CoP. Those CoPs are not necessarily in the same plane as ZMP and the projection of CoP_1 and CoP_2 in that plane along their respective GRF are named ZMP_1 and ZMP_2 . When walking on a flat ground CoP_i is equivalent to ZMP_i .

To define ZMP_1 and ZMP_2 trajectories, we added the via-points B'_q and C'_q assigned to both trajectories respectively. To find these polynomials, we interpolated them between $B_q \rightarrow B'_q$ and between $C'_q \rightarrow C_q$.

Using the ZMP definition, we obtain:

$$\Gamma(\mathbf{P}_{\text{ZMP}}/\mathbf{F}_{\text{ZMP}_1}) + \Gamma(\mathbf{P}_{\text{ZMP}}/\mathbf{F}_{\text{ZMP}_2}) = \mathbf{F}_{\text{ZMP}_1} \times (\mathbf{P}_{\text{ZMP}} - \mathbf{P}_{\text{ZMP}_1}) + \mathbf{F}_{\text{ZMP}_2} \times (\mathbf{P}_{\text{ZMP}} - \mathbf{P}_{\text{ZMP}_2}) = 0 \quad (3.12)$$

where $\Gamma(\mathbf{P}_{\text{ZMP}}/\mathbf{F}_{\text{ZMP}_i})$ is the torque of the GRF $\mathbf{F}_{\text{ZMP}_i}$ under foot $i \in \{1, 2\}$ computed with respect to ZMP.

Solving (3.12) in the direction \vec{y} we can write:

$$\sum_{i=1}^2 (x_{\text{ZMP}_i} - x_{\text{ZMP}}) F_{\text{ZMP}_i}^z = 0 \quad (3.13)$$

where x_{ZMP} is the component x of the ZMP position and $F_{ZMP_i}^z$ is the component z of the reaction force under the foot $i \in \{1, 2\}$. As the ZMP, ZMP_1 is defined as a 5th order polynomial.

From (3.13), we obtain the following relationship between ZMP_1 and ZMP_2 :

$$x_{ZMP_2} = x_{ZMP} - \frac{F_{ZMP_1}^z}{F_{ZMP_2}^z} (x_{ZMP_1} - x_{ZMP}) \quad (3.14)$$

From (3.14), if ZMP_1 trajectories and the repartition between $F_{ZMP_1}^z$ and $F_{ZMP_2}^z$ are known, we do not need to interpolate polynomials to obtain ZMP_2 trajectories.

Based on the model in Fig. 3.1a and related hypotheses, the relationship between $F_{ZMP_1}^z$ and $F_{ZMP_2}^z$ can be found:

$$\begin{aligned} F_{ZMP_1}^z + F_{ZMP_2}^z &= F_{ZMP}^z = Mg \\ F_{ZMP_1}^z &= Mg - F_{ZMP_2}^z \end{aligned} \quad (3.15)$$

where the reaction force $F_{ZMP_2}^z$ in (3.15) is defined by:

$$F_{ZMP_2}^z = d \cdot F_{ZMP}^z = d \cdot Mg \quad (3.16)$$

d in (3.16) is a 5th order polynomial representing the distribution of ZMP force under each foot.

From (3.14), (3.15) and (3.16), we obtain:

$$x_{ZMP_2} = x_{ZMP_1} - \frac{1}{d} (x_{ZMP_1} - x_{ZMP}) \quad (3.17)$$

The boundary conditions at the start of the DSP of phase j during a walking cycle are:

$$\begin{cases} F_{ZMP_2}^{z(j)}(t_{j-1}) = 0 \\ F_{ZMP_1}^{z(j)}(t_{j-1}) = F_{ZMP}^{z(j)}(t_{j-1}) = Mg \\ x_{ZMP_1}^{(j)}(t_{j-1}) = x_{ZMP}^{(j)}(t_{j-1}) = x_B^{(j)} \\ \dot{x}_{ZMP_1}^{(j)}(t_{j-1}) = \dot{x}_{ZMP}^{(j)}(t_{j-1}) = \dot{x}_B^{(j)} \\ \ddot{x}_{ZMP_1}^{(j)}(t_{j-1}) = \ddot{x}_{ZMP}^{(j)}(t_{j-1}) = \ddot{x}_B^{(j)} \end{cases} \quad (3.18)$$

where $x_B^{(j)}$, $\dot{x}_B^{(j)}$ and $\ddot{x}_B^{(j)}$ are the boundary conditions values between ZMP and ZMP_1 at the via-point B_j .

Deriving (3.13) and using (3.18), we obtain that $F_{ZMP_1}^{z(j)}$ and $F_{ZMP_2}^{z(j)}$ must satisfy:

$$\begin{bmatrix} F_{ZMP_1}^{z(j)}(t_{j-1}) \\ \dot{F}_{ZMP_1}^{z(j)}(t_{j-1}) \\ \ddot{F}_{ZMP_1}^{z(j)}(t_{j-1}) \end{bmatrix} = \begin{bmatrix} Mg \\ 0 \\ 0 \end{bmatrix} \quad \text{and} \quad \begin{bmatrix} F_{ZMP_2}^{z(j)}(t_{j-1}) \\ \dot{F}_{ZMP_2}^{z(j)}(t_{j-1}) \\ \ddot{F}_{ZMP_2}^{z(j)}(t_{j-1}) \end{bmatrix} = \begin{bmatrix} 0 \\ 0 \\ 0 \end{bmatrix} \quad (3.19)$$

Similarly, we obtain for the end of the DSP:

$$\begin{bmatrix} F_{ZMP_1}^{z(j)}(t_j) \\ \dot{F}_{ZMP_1}^{z(j)}(t_j) \\ \ddot{F}_{ZMP_1}^{z(j)}(t_j) \end{bmatrix} = \begin{bmatrix} 0 \\ 0 \\ 0 \end{bmatrix} \quad \text{and} \quad \begin{bmatrix} F_{ZMP_2}^{z(j)}(t_j) \\ \dot{F}_{ZMP_2}^{z(j)}(t_j) \\ \ddot{F}_{ZMP_2}^{z(j)}(t_j) \end{bmatrix} = \begin{bmatrix} Mg \\ 0 \\ 0 \end{bmatrix} \quad (3.20)$$

Equations (3.19) and (3.20) represent the initial and final conditions to interpolate d in (3.17). d is a function which varies from 0 to 1.

During the starting and the stopping sequences, we noticed the need to add parameters to ZMP₁ and ZMP₂ trajectories in order to satisfy better constraints. In particular, we added two via-points: B_q'' between $B_q \rightarrow B_q'$ and C_q'' between $C_q \rightarrow C_q'$. On these new via-points, ZMP₁ and ZMP₂ trajectories fulfill the boundary conditions in position, speed and acceleration

To define the function d during starting and stopping sequences, we took into consideration experimental studies on human walking [3]. During the starting sequence, humans move their COM laterally to be under the stance limb (we noted foot 2). The starting sequence begins with an equal repartition of load in each limb (under each foot in our case). Then, the lateral movement is induced by a momentary load of the swing limb (we noted foot 1). To finish, the stance limb is fully loaded and the swing limb is unloaded to begin the first SSP. For this reason, we chose the function k equal to 0.5 on C_1' , 0.25 on C_1'' and 1 on C_1 .

The human behavior to stop walking is symmetrical to the starting sequence [3]. During the stopping sequence, humans move laterally their COM and decelerate their movement. This lateral movement begins with a full load of the stance limb (foot 1) from the end of the SSP. Then, the deceleration is induced by a momentary load of the swing limb (foot 2). The stopping sequence ends with the same load repartition on each limb (under each foot in our case) [3]. For this reason, we chose the function k equal to 0 on B_{n+2} , 0.75 on B_{n+2}'' and 0.5 on B_{n+2}' .

$\dot{x}_{ZMP}^{(j)}$, $\ddot{x}_{ZMP}^{(j)}$, $\dot{x}_{ZMP_1}^{(j)}$ and $\ddot{x}_{ZMP_1}^{(j)}$ in DSP are easily obtained by deriving their 5th degree polynomials. Deriving (3.17), we obtain:

$$\dot{x}_{ZMP_2}^{(j)} = \dot{x}_{ZMP_1}^{(j)} - \frac{1}{d^{(j)}}(\dot{x}_{ZMP_1}^{(j)} - \dot{x}_{ZMP}^{(j)}) + \frac{\dot{d}^{(j)}}{d^{2(j)}}(x_{ZMP_1}^{(j)} - x_{ZMP}^{(j)}) \quad (3.21)$$

and

$$\ddot{x}_{ZMP_2}^{(j)} = \ddot{x}_{ZMP_1}^{(j)} - \frac{1}{d^{(j)}}(\ddot{x}_{ZMP_1}^{(j)} - \ddot{x}_{ZMP}^{(j)}) + 2\frac{\dot{d}^{(j)}}{d^{2(j)}}(\dot{x}_{ZMP_1}^{(j)} - \dot{x}_{ZMP}^{(j)}) + \left(\frac{\ddot{d}^{(j)}}{d^{2(j)}} - \frac{\dot{d}^{2(j)}}{2d^{3(j)}}\right)(x_{ZMP_1}^{(j)} - x_{ZMP}^{(j)}) \quad (3.22)$$

3.5.3 COM trajectories

We present here how COM trajectories are obtained from ZMP trajectories. Based on Morisawa *et al.* [34], (3.1) can be rewritten as:

$$\dot{x}_{\text{COM}}^{(j)} = \frac{g}{z_{\text{COM}}} (x_{\text{COM}}^{(j)} - x_{\text{ZMP}}^{(j)}) \quad (3.23)$$

Solving the differential equation (3.23) for x_{COM} when x_{ZMP} is given by (3.11), we obtain the analytical solution [34]:

$$x_{\text{COM}}^{(j)}(t) = V^{(j)} ch_j + W^{(j)} sh_j + \sum_{i=0}^5 C_i^{(j)} (\Delta t_j)^i \quad (3.24)$$

where:

$$\begin{aligned} ch_j &= \cosh(\omega_j \Delta t_j) \\ sh_j &= \sinh(\omega_j \Delta t_j) \\ \omega_j &= \sqrt{g/z_{\text{COM}}} \\ C_i^{(j)} &= \begin{cases} c_i^{(j)} + \sum_{k=1}^{(5-i)/2} b_{i+2k}^{(j)} c_{i+2k}^{(j)} & \text{for } i = 0 \dots 3 \\ c_i^{(j)} & \text{for } i = 4, 5 \end{cases} \\ b_{i+2k}^{(j)} &= \prod_{l=1}^k \frac{(i+2l)(i+2l-1)}{w_j^2} \\ \Delta t_j &= t - T_{j-1} \\ j &\in [1 \dots m] \end{aligned}$$

$V^{(j)}$ and $W^{(j)}$ are the unknowns of the system. In (3.24), $c_i^{(j)}$ coefficients are known. In comparison to the equation system in [34], our system is limited to 5th order polynomials and allow to write the COM trajectory in function of the ZMP trajectory, initial and final boundary conditions of COM trajectory.

Equation (3.24) has $2m$ unknowns with $m = 3n + 2$ phases. These unknowns satisfy the following boundary conditions for the COM position and velocity:

1. Initial

$$x^{(1)}(t_0) = V^{(1)} + C_0^{(1)} \quad (3.25)$$

$$\dot{x}^{(1)}(t_0) = W^{(1)} + C_1^{(1)} \quad (3.26)$$

2. Relationship between two successive sequences with $j \in [1 \dots (m-1)]$

$$VW^{(j)} + \sum_{i=0}^5 C_i^{(j)} (\Delta T_j)^i = V^{(j+1)} + C_0^{(j+1)} \quad (3.27)$$

$$VW\boldsymbol{\omega}^{(j)} + \sum_{i=1}^5 iC_i^{(j)}(\Delta T_j)^{i-1} = W^{(j+1)}\boldsymbol{\omega}_j + C_1^{(j+1)} \quad (3.28)$$

3. Final

$$x^{(m)}(T_m) = VW^{(m)} + \sum_{i=0}^5 C_i^{(m)}(\Delta T_m)^i \quad (3.29)$$

$$\frac{dx^{(m)}}{dt}(T_m) = VW\boldsymbol{\omega}^{(m)} + \sum_{i=1}^5 iC_i^{(m)}(\Delta T_m)^{i-1} \quad (3.30)$$

where

$$\begin{aligned} VW^{(j)} &= V^{(j)}Ch_j + W^{(j)}Sh_j \\ VW\boldsymbol{\omega}^{(j)} &= V^{(j)}\boldsymbol{\omega}_jSh_j + W^{(j)}\boldsymbol{\omega}_jCh_j \\ Ch_j &= \cosh(\boldsymbol{\omega}_j\Delta T_j) \\ Sh_j &= \sinh(\boldsymbol{\omega}_j\Delta T_j) \\ \Delta T_j &= T_j - T_{j-1} \end{aligned}$$

From the boundary conditions (3.25)-(3.29), the total conditions are $2m + 2$. Removing COM velocity conditions on initial and final phases (they are solved at the pattern optimization level), $2m$ conditions remain. The unknowns can be calculated then by the following system obtained by concatenation of previous equations:

$$\mathbf{G} \cdot \mathbf{vw} = \mathbf{N} \cdot \mathbf{x} + \mathbf{H} \cdot \mathbf{l} \quad (3.31)$$

where

$$\begin{aligned} \mathbf{vw} &= \left[V^{(1)} W^{(1)} \dots V^{(j)} W^{(j)} \dots V^{(m)} W^{(m)} \right]^T \\ \mathbf{x} &= \left[x_{\text{COM}}^{(1)}(T_1) \ 0 \ \dots \ 0 \ x_{\text{COM}}^{(m)}(T_m) \right]^T \\ \mathbf{l} &= \left[C_0^{(1)} \ \dots \ C_5^{(1)} \ \dots \ C_0^{(m)} \ \dots \ C_5^{(m)} \right]^T \\ \mathbf{G}_{h,q} &= \begin{cases} \begin{bmatrix} 1 & 0 \end{bmatrix} & \text{for } (h,q) = (1,1) \\ \begin{bmatrix} Ch_m & Sh_m \end{bmatrix} & \text{for } (h,q) = (m+2,m) \\ G_{1,h} & \text{for } q = h-1 \\ G_{2,h} & \text{for } q = h \\ 0 & \text{otherwise} \end{cases} \\ \mathbf{N}_{h,q} &= \begin{cases} 1 & \forall (h,q) \in \{(1,1); (2m,2m)\} \\ 0 & \text{otherwise} \end{cases} \end{aligned}$$

$$\mathbf{H}_{h,q} = \begin{cases} - \begin{bmatrix} 1 & 0 & 0 & 0 & 0 & 0 \end{bmatrix} & \text{for } (h,q) = (1,1) \\ - \begin{bmatrix} (\Delta T_m)^0 & \dots & (\Delta T_m)^5 \end{bmatrix} & \text{for } (h,q) = (m+2,m) \\ H_{1,h} & \text{for } q = h-1 \\ H_{2,h} & \text{for } q = h \\ 0 & \text{otherwise} \end{cases}$$

with

$$h = 1, \dots, m+2,$$

$$q = 1, \dots, m$$

$$\mathbf{G}_{1,h} = \begin{bmatrix} Ch_h & Sh_h \\ \omega_h Sh_h & \omega_h Ch_h \end{bmatrix},$$

$$\mathbf{G}_{2,h} = \begin{bmatrix} -1 & 0 \\ 0 & -\omega_h \end{bmatrix},$$

$$\mathbf{H}_{1,h} = - \begin{bmatrix} (\Delta T_m)^0 & (\Delta T_m)^1 & \dots & (\Delta T_m)^5 \\ 0 & (\Delta T_m)^0 & \dots & 5(\Delta T_m)^4 \end{bmatrix},$$

$$\mathbf{H}_{2,h} = \begin{bmatrix} 1 & 0 & 0 & 0 & 0 & 0 \\ 0 & 1 & 0 & 0 & 0 & 0 \end{bmatrix}.$$

3.6 WPG validation with experiments on HRP-2

Now we present and analyze the results of our WPG. We implemented and tested our obtained walking motion in experiments conducted with the HRP-2 robot: first with the built-in feet including an ankle flexibility, then with our specially designed feet with flexible sole.

For the experiments with HRP-2, we considered only straight line walking for 1m with 10 steps. This is enough to have non-biased results and to assess the WPG before its use with the sole deformation estimator in Chapter 4. In addition, we use a simple robot controller which doesn't take into account the trajectories of ZMP_1 and ZMP_2 .

The criteria weight μ of $E(3.5)$ has a low impact on the ZMP trajectory behavior. In this section, μ is set to zero to see the influence of the weight λ .

In later experiments when the trajectories of ZMP_1 and ZMP_2 are taken into account, we chose μ equal to 15 which experimentally gave us the best compromise to generate a ZMP going from heel to toe under each foot.

3.6.1 Walking pattern behaviors

The Fig. 3.4a shows part of the obtained ZMP and COM reference trajectories for different values of λ (3.5):

- $\lambda \rightarrow 1$: minimization of COM force only
- $\lambda \rightarrow 0$: minimization of ankle torque only
- $\lambda = 0.5$: minimization with equal weights on COM force and on ankle torque

As expected, for $\lambda = 0$ we obtain ZMP and COM trajectories similar to [28, 33] with large lateral variations of the COM. For $\lambda \rightarrow 1$ trajectories are similar to [29, 35] with small lateral variations of the COM and with a ZMP close to the feet edge. The mid-compromise solution $\lambda = 0.5$ gives limited lateral variations of the COM with a ZMP similar to that of a human walk [3]. All solutions result in walk with right and left feet as close as possible, so as to minimize lateral variations of COM (and hence COM force) and to minimize variation of ZMP in DSP. We did not consider the case $\lambda = 1$ since it is not well-posed: COM force criteria does not depend on ZMP of each foot in the DSP which could then be any trajectory in the feet.

The Fig. 3.4b shows the ZMP_1 and ZMP_2 trajectories during the DSP. Both ZMP_2 and ZMP_1 go from toe to heel. Considering only one foot contact, this gives a toe-heel-toe-heel ZMP trajectory, which is different from the human heel-toe ZMP trajectory [36]. This result is a direct consequence of minimizing ankle torque with our reduced model. indeed, it is better that the ZMP of the landing foot goes through the foot's center to minimize the ankle torque instead of remaining in the heel (same reasoning stands for take-off foot). For a flexible sole this means first foot contact is on the toe, then the foot rotates around the heel, the toe and the heel again. We believe that taking into account foot rotation with a flexible sole, would allow to write a better ankle energy consumption criterion to penalize this behavior.

3.6.2 Experiments with ankle flexibilities

We tested our walking patterns on the HRP-2 humanoid robot, see the accompanying video¹. Each time we compared with the 'test' pattern from [34].

Fig. 3.5 shows the evolution of the torques in the right foot ankle (results are similar to the left part). Theoretical ankle torques increase with λ since the weight associated to the ankle in the torque criterion is decreased. More precisely:

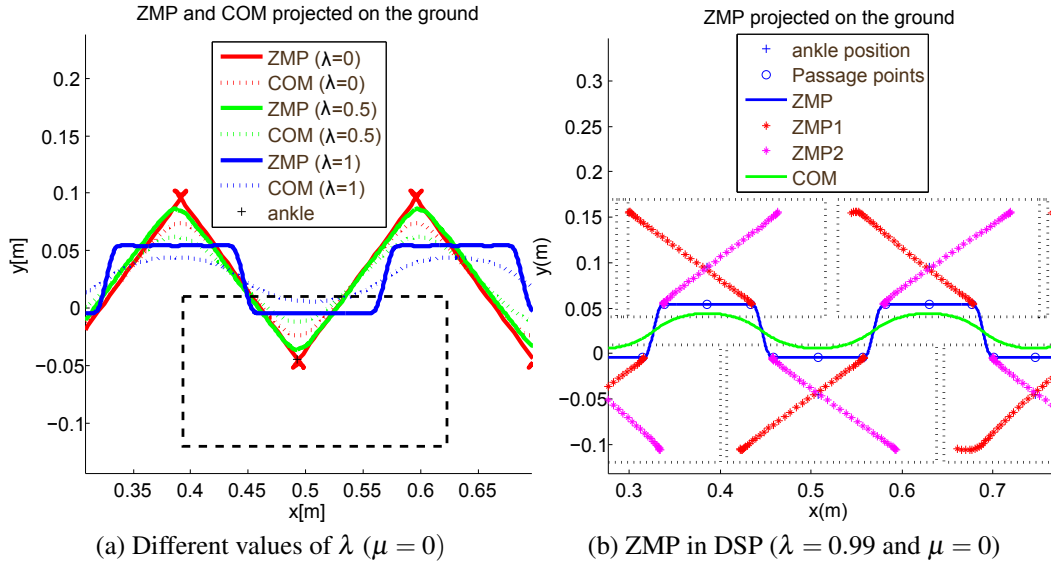


Figure 3.4 ZMP and COM trajectories

- From $\lambda = 0$ to 0.2, torques are larger than the theoretical ones. This might be due to the difficulty to compensate for the flexibility deformation;
- From $\lambda = 0.3$ to 0.5, torques are close to theoretical ones;
- From $\lambda = 0.6$ to 0.99, torques are larger than the theoretical ones. Indeed, important deformation happens when ZMP is close to the edge of the foot, which is a difficult situation to stabilize.

Fig. 3.6 shows the evolution of the COM acceleration in the lateral direction (which is also the image of force on COM). We do not show the COM acceleration in the walking direction as it is almost not varying with λ . Theoretical COM acceleration decreases with λ since the ankle's weight in the torque criterion is increased:

- From $\lambda = 0$ to 0.5, the evolution of COM acceleration is similar to the theoretical one, yet with additional variations, that might be due to the stabilization;
- From $\lambda = 0.6$ to 0.99, as for torques in ankle, the COM acceleration is not decreasing because of the instability when the ZMP is close to the foot's edge.

The energy consumption for the whole walk can be estimated by:

$$E = \int_{t_i}^{t_f} \left(\sum_j \dot{q}_j(t) \cdot \Gamma_j(t) \right) dt \quad (3.32)$$

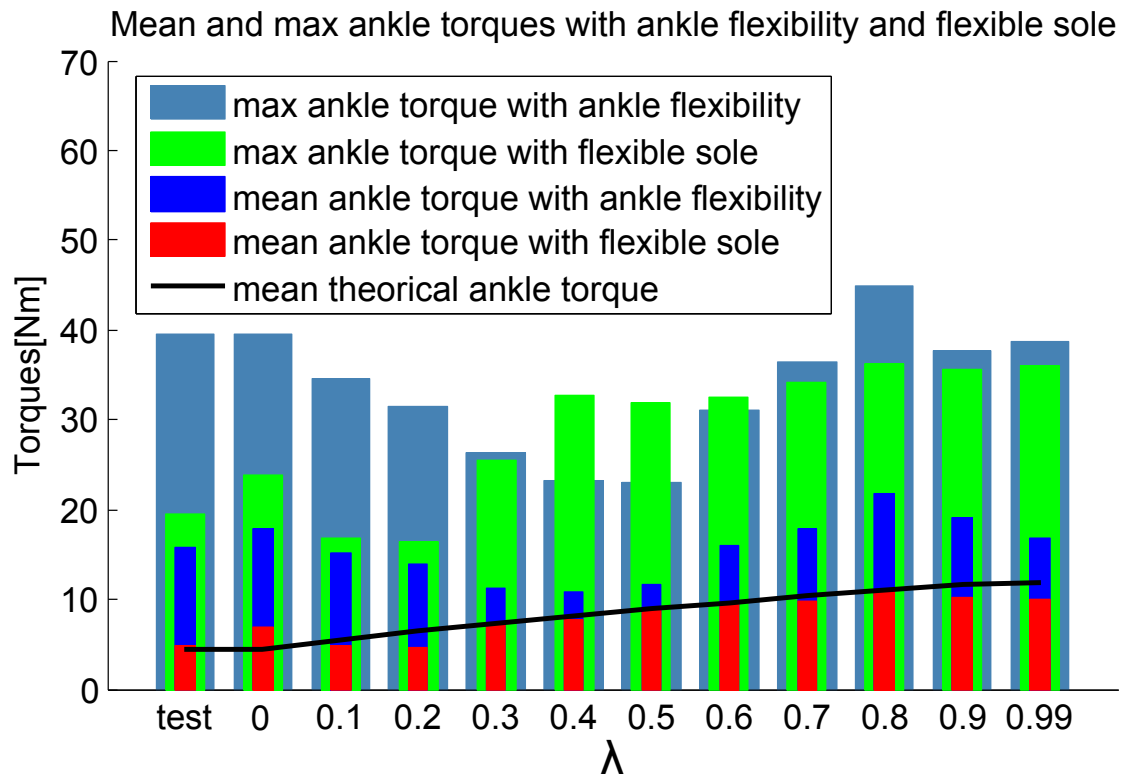


Figure 3.5 Ankle torque with flexible soles and ankle flexibilities

where s_j is the actuator's angular velocity j and Γ_j its torque.

Fig. 3.7 shows the evolution of the energy needed by the left leg of the robot to achieve the whole walk (it is similar for the right leg). We observe a minimum in the energy consumption for $\lambda = 0.2, 0.3$, which is the best compromise between our criteria. In addition, we obtain a 15% decrease of energy consumption compared to [34].

3.6.3 Experiment with flexible sole

We did the same experiments as previously with different feet of the HRP-2, see accompanying video¹. We removed the springs in ankle and added a flexible sole to absorb the landing impact shock. Fig. 3.8 shows HRP-2's new feet.

Fig. 3.5 shows the evolution of torques in right foot ankle with new feet (results are similar in left foot ankle). For all λ , evolution of experimental torques is similar to the theoretical ones, even for λ from 0.6 to 0.99, when the walk becomes unstable (see video¹). In comparison to previous ankle flexible foot, the mean values of torques in ankle with new feet have almost been reduced by 5Nm. However, for lateral COM acceleration of Fig. 3.6,

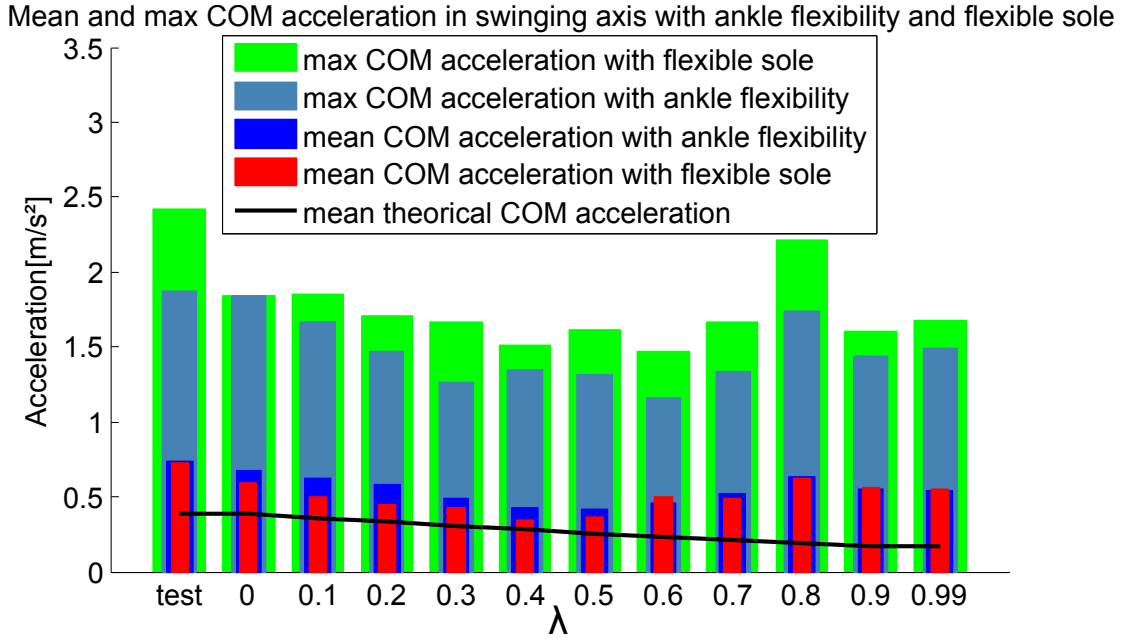


Figure 3.6 COM acceleration in the swinging direction with flexible soles and ankle flexibilities

mean COM acceleration with new feet is still more than the theoretical one, but is slightly better than ankle flexible foot.

Additionally, some instability can be observed in the video¹ with new feet when the ZMP is close to the foot edge, while with old feet it is more stable. Later in Chapter 5 we improve the sole flexibility stabilization control scheme that here is tuned for the old feet system. We also hope to reduce part of this instability with soles design.

We looked at the impact force: when the walk is stable, maximum force is about 650N for old feet and 630N for new feet, while for unstable walk it can reach 700N for both types of feet. The minimum energy consumption for $\lambda = 0.2, 0.3$ is still valid for new feet with flexible soles, Fig. 3.7.

3.6.4 WPG optimization results

In later experiments, we chose μ equal to 15 which experimentally gave us the best compromise to have ZMP going from heel to toe under each foot. By comparing Fig. 3.4a and Fig. 3.9a, we can see that μ has a low impact on the ZMP and COM trajectory behaviors.

The Fig. 3.9b shows also ZMP_1 and ZMP_2 trajectories during the DSP. ZMP_1 and ZMP_2 are local ZMPs in DSP. When we have ZMP_1 under one foot, we have a ZMP_2 under the opposite one. In Fig. 2.9b several foot steps are drawn and each foot step has a ZMP_1 and

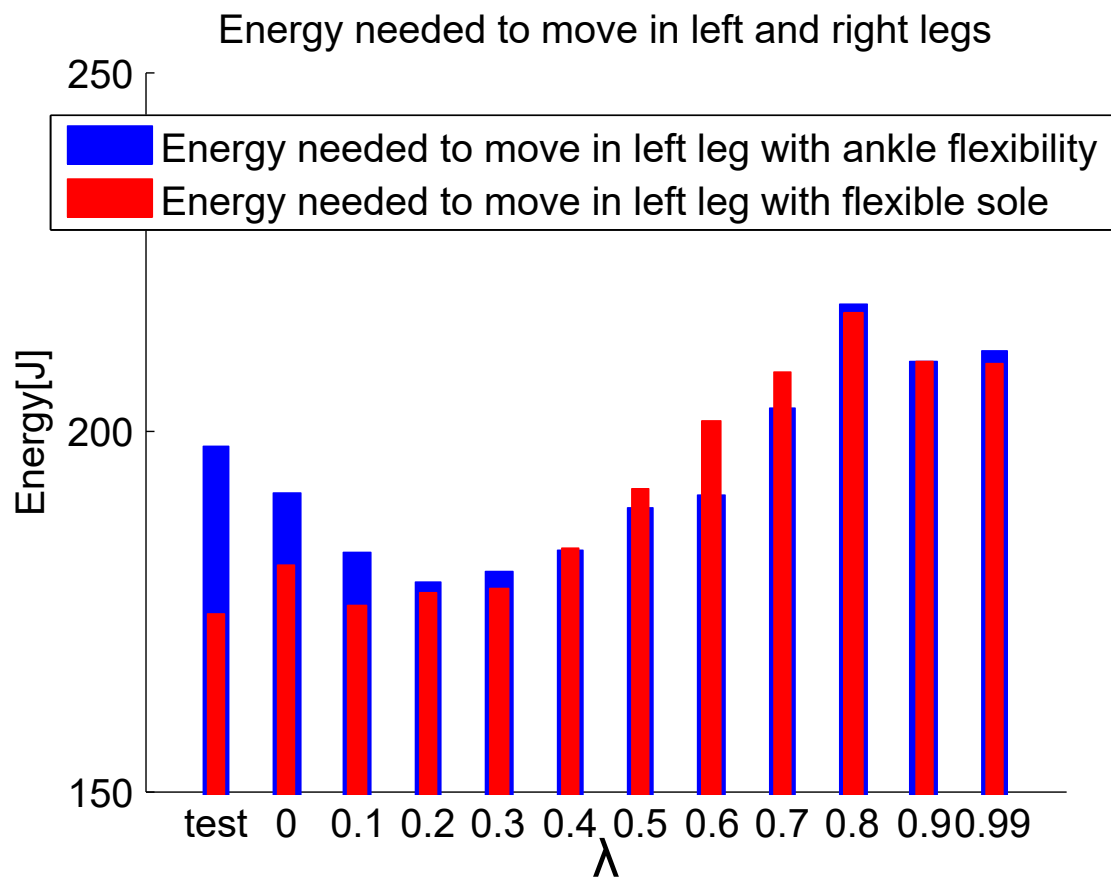


Figure 3.7 Energy needed by left leg to achieve the whole walk



Figure 3.8 Photo of HRP-2's feet with flexible soles

ZMP_2 but they don't exist during the same phase. By setting μ at 15, we obtain heel to toe trajectories, close to human.

By setting different constraint in the QP optimization, it is possible to generate different kind of paths. Fig. 3.10a shows an example of walking generated with optional constraints. In Figures 3.10a to 3.10b, the foot steps number $\{6, 17, 23\}$ have a given fixed position. In

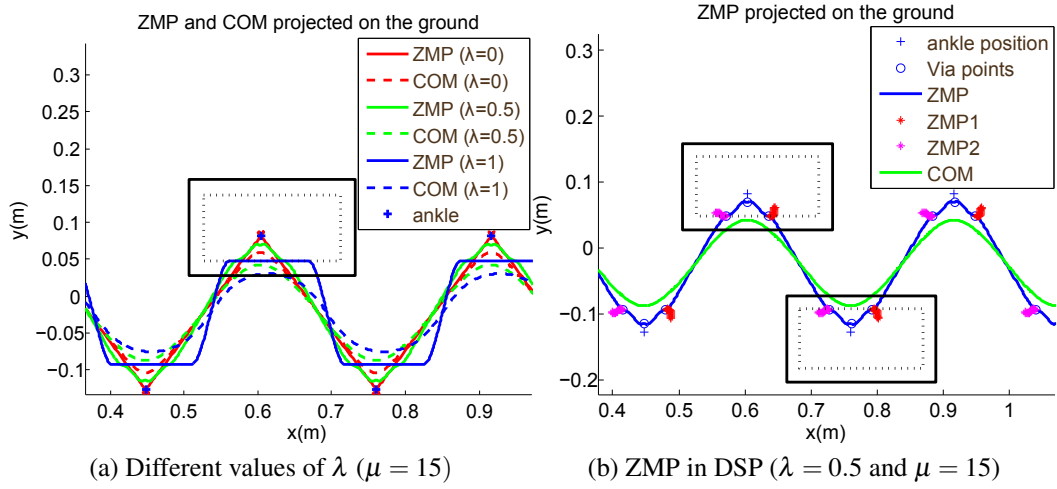


Figure 3.9 ZMP and COM trajectories

Fig. 3.10b, the foot steps number $\{6 - 17, 23 - 30\}$ also have a given orientation. The QP optimization choose the optimal foot placement for the rest of the walk.

3.7 Conclusion

We devised a WPG based on the minimization of energy consumption simplified by the minimization of COM forces and torques at the ankle level. Our WPG computes smooth ZMP and COM trajectories from 5th-order polynomials and also generates ZMP under each foot during the double support phase (DSP). Using a ZMP under each foot, we check the stability conditions in the DSP and write them in a linear form. In addition, this formulation is useful for a quasi-static sole deformation model as the orientation of the foot is directly linked to these parameters. Thus, it allows computing human-like foot rolling depending on the sole shape design.

HRP-2's experiments showed that the flexibility in the ankles (due to the built-in shock-absorbing mechanism) induces relatively high torques. Without these *springs*, torques in ankle were reduced. Therefore, as an alternative to each ankle shock-absorbing mechanism to protect the robot structure and improve its stability during walking, we can now consider using flexible soles.

The experimental comparison between the latter options, revealed the effects of ZMP and COM trajectories on the walking motion and impacts on the robots. Indeed, by choosing the weights of the optimization criterion, it was possible to tune the walking gait.

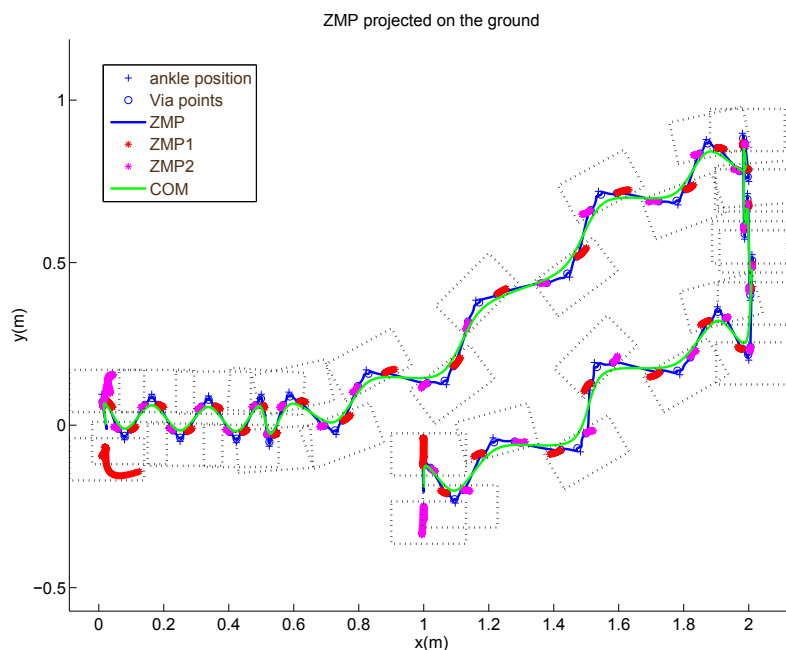
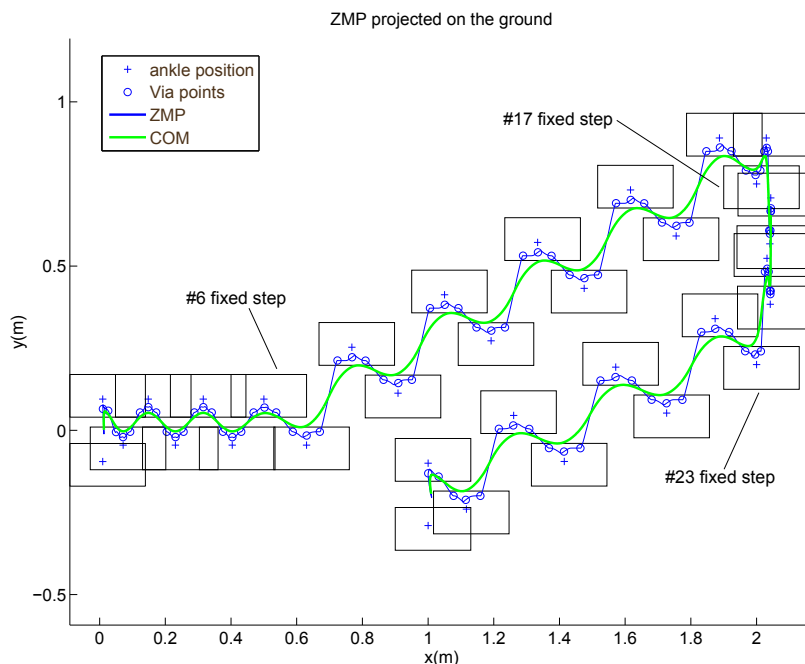


Figure 3.10 Examples of a generated walking gait

Based on the observations in Chapter 2, the human take into account the floor stiffness property when walking. The resulting parameters given by the WPG developed in this chapter will be used jointly to predict and take into account the sole deformation to balance and

control the humanoid robots. Such deformation will be predicted by a deformation estimator (Chapter 4) and will be taken into account in a closed-loop controller (Chapter 5).

Chapter 4

Soft sole deformation estimator

When looking at human balance strategy on soft surface in Chapter 2, we observed a combined control of center of pressure (CoP) and ground reaction force (GRF) under each foot. In Chapter 3, we devised a walking pattern generator (WPG) in order to generate an optimal walking motion for humanoid robot. This WPG manage, in addition to the common COM and ZMP to walk on flat floor, the local zero moment point (ZMP) under each foot equivalent to local CoP.

In order to control more efficiently the feet-ground interaction of humanoid robots during walking, this chapter investigate adding outer soft (i.e. compliant) soles to the feet. The deformation subsequent to the contact of the soles with the ground is taken into account using the new walking pattern generator (Chapter 3) and a deformation estimator (DE) [37, 17]. This novel humanoid walking approach ensures that the desired ZMP is better followed with soft soles.

Abstract

In this Chapter, we investigate the effect of removing ankle flexibilities and adding thick soft soles in humanoid walking. By doing this, we keep the same heel strike impact absorption while improving stiffness in flat foot position by a better contact-surface casting. But such a soft sole has a varying compliance due to change of contact area and needs to be considered in the attitude stabilization. In order to improve balance of the robot during walk and to cope with such varying compliance, we developed in this chapter a sole deformation estimator (DE) that outputs feet position and orientation compatible with ZMP and ground reaction force. Those feet position and orientation used as reference improves ZMP tracking. Such DE is based on algorithms that combine a FEM model of the soles and handle the contact

with the floor in function of the foot movement. Then an iterative algorithm find the good foot position and orientation to match the desired ZMP force and position.

We validate our new controller using the HRP-4 humanoid robot performing walking experiments with and without the estimator. Also, to test the robustness of our simulator and to obtain low-energy walking, we performed different walking behaviors.

4.1 Problem formulation

Gaited or non-gaited walking is generated by alternating phases of contact creation and breaking with the environment [38]. With rigid links and without shock absorbing mechanism, impact forces with the ground must be thresholded through contact transitions with nearly zero speed. This considerably limits the walking dynamics. Therefore, compliant mechanisms are used in humanoid robotics to absorb shocks at impacts and prohibit their propagation along the entire structure that results in non-desirable vibrations and eventually unstable behaviors. One common solution is to add flexible mechanisms at the robot ankles [39, 40] that also protect the feet embedded force sensors. Unfortunately, such compliant mechanisms also act as passive joints whose deformations are hardly measurable [41]. In this way, the robot attitude is difficult to control, especially in complex maneuvers [42]. Another solution is to add the compliance between the foot and ground contact, see early work by [43]. In fact, humanoid robots have generally a thin rubber sole attached under each robot foot. Due to the thinness of this sole, the impacts are mainly absorbed by the ankle flexibility.

Alternatively, we favor removing the ankle flexibilities and investigate the use of thick soft soles under each foot of a humanoid robot (see Fig. 4.1). These soles not only absorb the impacts due to contact transitions, they also cast ground unevenness resulting in a relative increase of the contact surface. During walking, the compliance of these soles depends on the contact area variations. Also, since the compliance is put outside, it can be decoupled from the rigid dynamics.

In most simplified model-based planning and control, the ankle flexibility and the sole compliance are not modeled. They are left as ‘perturbations’ or ‘uncertainties’ to be tackled by the closed-loop controller. Therefore, controllers have to compensate for the errors in the attitude (i.e. free-floating orientation and position) due to the deformations of the flexible parts. In our control framework, we consider the model of the deformation that results from the contact of the soft sole with the ground using the Finite Element Model (FEM) and the mechanical laws of compliant contacts.

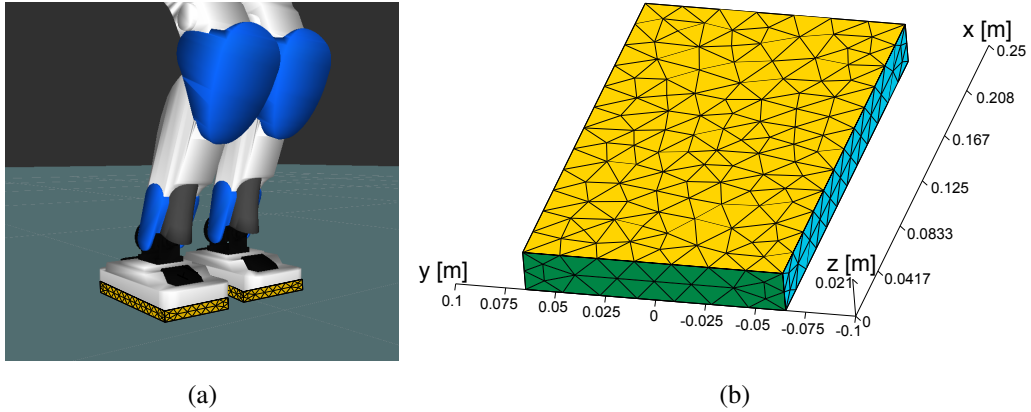


Figure 4.1 (a): Rectangular parallelepiped soles mounted on HRP-4's feet; (b): meshed sole with 1494 tetrahedron elements

To control the humanoid robot attitude during walking, we use the multi-objective Quadratic Programming (QP) control scheme illustrated in Fig. 4.2. The developed WPG of Chapter 3 is coupled with a sole DE that allows to predict feet positions and orientations.

For the remainder of the paper, we denote with superscript d the desired value generated by the WPG.

4.2 Deformation estimator

In this section, we develop an algorithm that calculates the ankle position/orientation and the deformation of the flexible sole [37] to match the interaction force $\mathbf{F}_{\text{ZMP}}^d(t)$ and the ZMP trajectory $\mathbf{P}_{\text{ZMP}}^d(t)$ given by the WPG (see the control scheme 4.2).

The Fig. 4.5 shows this algorithm. It is divided in two main blocks: frictional contact problem (see section 4.2.3) and update sole position and orientation (see section 4.2.4). For a more detailed presentation, see also [44].

4.2.1 Feet trajectories

The ankle position and orientation during the contact phase can be calculated using the following equation:

$$\mathbf{P}_a = \mathbf{O}_l + \mathbf{R}^l \mathbf{P}_a \quad (4.1)$$

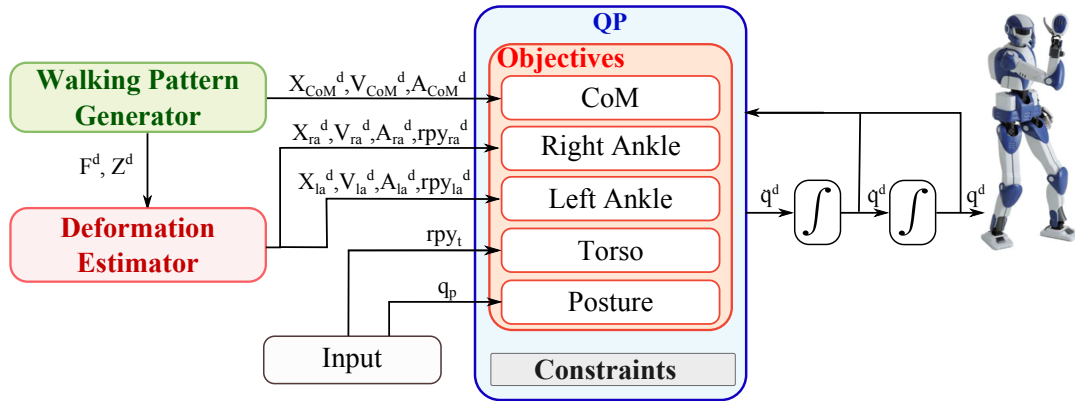


Figure 4.2 Control scheme. The ankle reference trajectories change according to sole deformations.

where \mathbf{P}_a is the ankle position in the world frame, \mathbf{O}_l is the sole frame origin position in world frame, \mathbf{R} is the rotation matrix from the sole frame to the world frame and ${}^l\mathbf{P}_a$ is the ankle position in the sole frame.

During the SSP, ankle positions and orientations of the foot in the air are computed by interpolating with 5th order polynomials the absolute ankle orientation, position, velocity and acceleration between take-off and landing phases.

4.2.2 Soft sole model

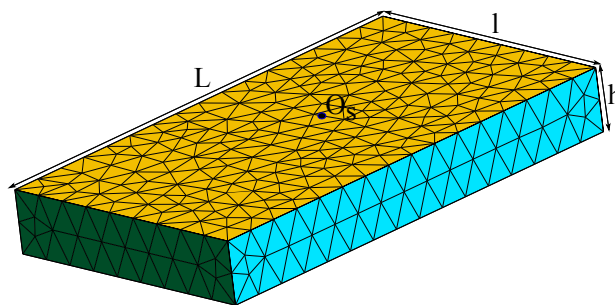


Figure 4.3 Simple sole shape. \mathbf{O}_s is the center of the surface attached to the foot

To simulate the flexible behavior of the sole, a static linear FEM is used [45] under the assumption of small deformations [46]. This model is valid when the node displacements

relative to the object size is relatively low and the system response is fast enough to neglect the dynamic phenomena. Nevertheless, static simulation is a good approximation since \mathbf{F}_{ZMP}^d and \mathbf{P}_{ZMP}^d variations are negligible w.r.t the sole dynamic response. In this chapter, we assume that under a given force, the dynamic sole deformations are faster than the dynamic forces exerted on the sole and the sole has not big deformations.

Ω is the sole shape meshed with 1494 tetrahedron elements (see meshed sole in Fig. 4.3), Ω_I is the interior volume of Ω , $\partial\Omega$ gather the surface S_D attached to the rigid robot foot (Dirichlet surface) and the surface S_S that could be in contact with the ground. S_D and S_S contain two disjoint set of nodes:

$$\partial\Omega = S_D \cup S_S, \quad \text{with } S_D \cap S_S = \emptyset \quad (4.2)$$

where S_D is the surface attached to the lower part of the robot foot and S_S is the surface that could be in contact with the ground.

To simulate the foot movement, we divide the foot in two attached subsystems: a rigid and a flexible part. The position of each point of the sole is the sum of the movement of the rigid part and the deforming motion induced by sole flexibility.

To simulate the deforming motion given by the flexible sole, we use FEM and contact handling respecting mechanical laws to obtain a desired ZMP force and position.

The mechanical structures are susceptible to a variety of behaviors depending on the characteristics of their materials, loads, connections between structural elements, etc. The FEM provides a generic framework for approximate calculation of different structures with complex geometries and various behaviors.

In the static case for linear elasticity, a characteristic stiffness matrix is extracted from each element. These elementary matrices are then assembled in a large stiffness matrix K of the sole.

Once the sole is discretized by the finite element method, the displacements at each point of the mesh depend on external forces applied to those points. From the static linear FEM, we can write a relationship between the node displacements of Ω and the external forces:

$$\mathbf{K} \underline{\mathbf{U}} = \underline{\mathbf{F}} \quad (4.3)$$

where $\underline{\mathbf{F}} \in \mathbb{R}^N$ is the vector of nodal forces and $\underline{\mathbf{U}} \in \mathbb{R}^N$ is the vector of the node displacements. The superscript l before a letter denotes a vector expressed in the sole frame and no superscript means that the vector is expressed in the world frame.

Bro-Nielsen and Cotin [47] introduce the static FEM in real-time applications condensing (4.3) to the surface nodes. For this reason, we divide the nodes of the sole in three parts:

1. **Possible contact nodes:** nodes that could be in contact with the ground in case of collision detection (denoted by the subscript S)
2. **Dirichlet's nodes:** surface nodes on the upper part of the sole. This part is attached to the lower surface of the robot foot (denoted by the subscript D)
3. **Internal nodes:** nodes inside the contact surface and the surface attached to the robot (denoted by the subscript I)

From the definition, the Dirichlet nodes have a known null displacement. Thus, the system (4.3) can be rewritten as:

$$\begin{bmatrix} \mathbf{K}_{DD} & \mathbf{K}_{DI} & \mathbf{K}_{DS} \\ \mathbf{K}_{ID} & \mathbf{K}_{II} & \mathbf{K}_{IS} \\ \mathbf{K}_{SD} & \mathbf{K}_{SI} & \mathbf{K}_{SS} \end{bmatrix} \begin{bmatrix} \underline{\mathbf{0}} \\ \underline{\mathbf{U}}_I \\ \underline{\mathbf{U}}_S \end{bmatrix} = \begin{bmatrix} \underline{\mathbf{F}}_D \\ \underline{\mathbf{F}}_I \\ \underline{\mathbf{F}}_S \end{bmatrix} \quad (4.4)$$

where I , D and S denotes respectively nodes of Ω_I , S_D and S_S .

As in [47], we suppose that the internal interaction forces $\underline{\mathbf{F}}_I$ are zeros and therefore S_D is the only surface with nodal forces.

The system (4.4) can be rewritten:

$$\begin{bmatrix} \mathbf{K}_{II} & \mathbf{K}_{IS} \\ \mathbf{K}_{SI} & \mathbf{K}_{SS} \end{bmatrix} \begin{bmatrix} \underline{\mathbf{U}}_I \\ \underline{\mathbf{U}}_S \end{bmatrix} = \begin{bmatrix} \underline{\mathbf{0}} \\ \underline{\mathbf{F}}_S \end{bmatrix} \quad (4.5)$$

Based on [47] and (4.5), a condensed linear elasticity law is defined:

$$\left\{ \begin{array}{l} \underline{\mathbf{U}}_S = (\mathbf{K}_{SS} - \mathbf{K}_{SI}\mathbf{K}_{II}^{-1}\mathbf{K}_{IS})^{-1} \underline{\mathbf{F}}_S \\ \quad = \mathbf{K}_S^{-1} \underline{\mathbf{F}}_S \\ \quad = \mathbf{C}_S \underline{\mathbf{F}}_S \\ \underline{\mathbf{U}}_I = -\mathbf{K}_{II}^{-1}\mathbf{K}_{IS} \underline{\mathbf{U}}_S \end{array} \right. \quad (4.6)$$

where \mathbf{K}_S is the stiffness surface matrix and \mathbf{C}_S is the compliance surface matrix.

In order to obtain the shape deformation from (4.6), the contact with the ground directly induces $\underline{\mathbf{U}}_S$, which engender the computation of $\underline{\mathbf{U}}_I$. Based on [47], we consider that \mathbf{F}_S are only applied on the surface nodes of the object and those would be the only points in contact with the ground. For this reason, to find the displacement of each nodes, we divide the simulation in two steps:

1. Find the displacement of the surface nodes induced by the contact with the ground (see section 4.2.3)
2. Based on the displacement of the surface nodes, we compute the displacement of the internal nodes using the second equation of (4.6)

4.2.3 Frictional contact problem

In this section, we illustrate how we handle the contact between deformable object (sole) and rigid object (ground). To model the contact, we use a relationship between the two unknowns of the system (4.6): the contact space displacement vector $\underline{\delta}$ and contact force vector \underline{F} at each time step t_s (see figure 4.4). This problem must be constrained to verify the Signorini's and Coulomb's laws.

The *inputs* of this algorithm are:

1. ${}^l\underline{P}^{\text{free}}$: node positions for free sole
2. \mathbf{C}_S : surface compliance matrix from (4.6)
3. ${}^l\underline{P}^{t_s-1}$: node positions at the previous time step
4. \mathbf{O}_J : foot position vector
5. $\mathbf{Y} = (\theta, \phi, \psi)$: Euler rotation angles of the foot

The *outputs* of this algorithm are:

1. $\underline{\delta}$: relative position of the sole nodes with respect to the ground reference \mathbf{Q}_α (see Fig. 4.4). It is called node contact space displacement vector
2. \underline{F} : node contact force vector

For a contact point α , $\underline{\delta}_\alpha$ is defined by:

$$\underline{\delta}_\alpha = \mathbf{P}_\alpha - \mathbf{Q}_\alpha \quad (4.7)$$

where \mathbf{Q}_α is a reference point on the ground detailed later.

The normal component of a vector is denoted by the subscript n such as $\mathbf{v}_n = \mathbf{n}\mathbf{v}$ where $\mathbf{n} = \begin{bmatrix} 0 & 0 & 1 \end{bmatrix}$; the tangential components of a vector are denoted by the subscript t such as $\mathbf{v}_t = \mathbf{t}\mathbf{v}$, where $\mathbf{t} = \begin{bmatrix} 1 & 0 & 0 \\ 0 & 1 & 0 \end{bmatrix}$. The superscript T denotes the transpose operator.

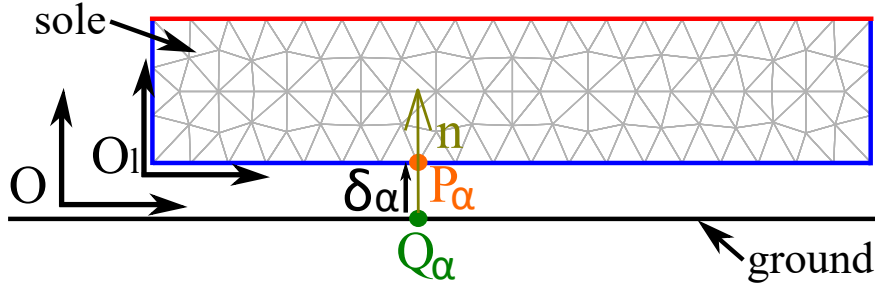


Figure 4.4 Contact between the sole and the ground

The contact model used for calculating the deformation of the sole takes into account two very important mechanical laws: (i) the **Signorini's law** is used to enforce the non-interpenetration (in the computation) of the sole with the ground, and (ii) the **Coulomb's law** which defines the dry friction. Based on (4.7), we have:

1. **Signorini's law** establishes the complementarity between the contact force \mathbf{F} and the interpenetration distance vector $\boldsymbol{\delta}$ along with the normal component [48]:

$$\mathbf{0} \leq \mathbf{F}_{n,\alpha} \perp \boldsymbol{\delta}_{n,\alpha} \geq \mathbf{0} \quad (4.8)$$

where \mathbf{F}_α is the contact force applied to a contact node α , subscript n is its normal component. In case of contact between objects, the interpenetration distance is zero and the contact force is positive otherwise the interpenetration distance is positive and the contact force is zero.

2. **Coulomb's law** characterizes the dry friction. If \mathbf{F}_c is the contact force, F_n is its normal component, \mathbf{F}_t are its tangential components and μ the friction coefficient, we can distinguish two state conditions: *stick* and *slip* motion.

(a) **Stick condition:**

$$\|\mathbf{F}_{t,\alpha}\| < \mu |F_{n,\alpha}|, \boldsymbol{\delta}_{t,\alpha} = \mathbf{0} \quad (4.9)$$

(b) **Slip condition:**

$$\mathbf{F}_{t,\alpha} = -\mu F_{n,\alpha} \frac{\boldsymbol{\delta}_{t,\alpha}}{\|\boldsymbol{\delta}_{t,\alpha}\|} \quad (4.10)$$

where μ is the friction coefficient.

Based on the framework in figure 4.5, we want to find a possible configuration of the contact points to obtain \mathbf{F}_{ZMP}^d and \mathbf{P}_{ZMP}^d given by the walking pattern generator.

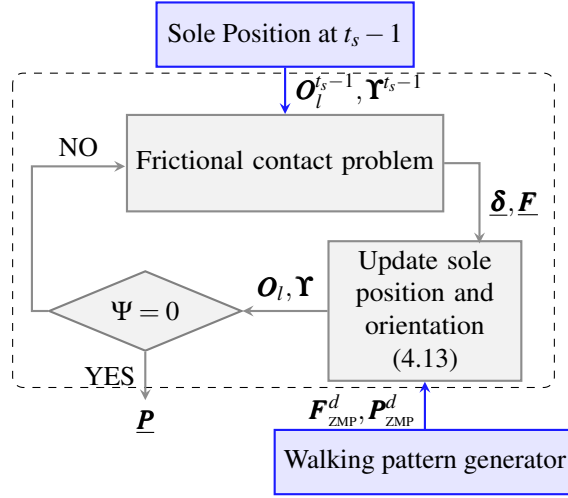


Figure 4.5 Framework for contact handling to obtain \mathbf{F}_{ZMP}^d and \mathbf{P}_{ZMP}^d . $t_s - 1$ is the previous time step and $\Psi = [\mathbf{F}_{ZMP} - \mathbf{F}_{ZMP}^d, \mathbf{P}_{ZMP} - \mathbf{P}_{ZMP}^d, \Gamma_{\mathbf{P}_{ZMP}, n}]^T$

The foot velocity is not considered in the static case. In the quasi-static case taking into account the slippage, the foot velocity is considered by computing the state just after the sole stop to slip. Therefore, slip occur until a static state is reached. This gives a non-reversible sole simulation and a sole state that depends on the history of its deformation.

Finally, an iterative Gauss-Seidel method in [49, 50] is used to solve the system (4.7). This method is very fast and applicable for real-time solution [49].

The Signorini's and Coulomb's laws and the Gauss-Seidel method are detailed in Appendix B.

4.2.4 ZMP force and position algorithm

In the frictional contact problem of the previous section, the foot position and orientation are the inputs when the contact forces and the contact space displacements are the outputs. Here, a new algorithm is developed to find the good foot position and orientation to match a desired ZMP force $\mathbf{F}_{ZMP}^d(t)$ and position $\mathbf{P}_{ZMP}^d(t)$ (see Fig. 4.5). Seeing the sole as a (complex 6-dof) spring, the principle is to invert the relation between the spring deformation and the force applied to it.

The *inputs* of this algorithm are the geometric and mechanical properties of the sole and the desired ZMP: i) ${}^l\mathbf{P}^{\text{free}}$, ii) \mathbf{C}_S , iii) ${}^l\mathbf{P}^{t_s-1}$, iv) $(\mathbf{F}_{ZMP}^d, \mathbf{P}_{ZMP}^d)$.

The *outputs* of this algorithm are the foot position and orientation: i) \mathbf{O}_l , ii) $\mathbf{Y} = (\theta, \phi, \psi)$. Recall that the contact node forces \mathbf{F} and the displacements δ are computed solving the frictional contact problem explained in the previous section.

Then we need to find a relationship between $(\mathbf{F}_{ZMP}^d, \mathbf{P}_{ZMP}^d)$ and $(\mathbf{O}_l, \mathbf{R})$:

$$\begin{bmatrix} \mathbf{F}_{ZMP}^d - \mathbf{F}_{ZMP}^{(t_s-1)} \\ \mathbf{P}_{ZMP}^d - \mathbf{P}_{ZMP}^{(t_s-1)} \\ \Gamma_{\mathbf{P}_{ZMP},n}^d - \Gamma_{\mathbf{P}_{ZMP},n}^{(t_s-1)} \end{bmatrix} = \begin{bmatrix} d\mathbf{F}_{tot} \\ d\mathbf{Z} \\ d\Gamma_{Z,n} \end{bmatrix} = \mathbf{K} \begin{bmatrix} d\mathbf{O}_l \\ d\mathbf{Rot} \end{bmatrix} = \mathbf{K} \begin{bmatrix} \mathbf{O}_l^{(t_s)} - \mathbf{O}_l^{(t_s-1)} \\ \mathbf{Rot}^{(t_s)} - \mathbf{Rot}^{(t_s-1)} \end{bmatrix} \quad (4.11)$$

where \mathbf{F}_{ZMP}^d and \mathbf{P}_{ZMP}^d are respectively the desired force at ZMP and ZMP position at t_s , we impose null vertical torque on ZMP ($\Gamma_{\mathbf{P}_{ZMP},n}^d = 0$) at t_s , $\mathbf{F}_{ZMP}^{(t_s-1)}$, $\mathbf{P}_{ZMP}^{(t_s-1)}$ and $\Gamma_{\mathbf{P}_{ZMP},n}^{(t_s-1)}$ are respectively the force at ZMP, the ZMP position and the resultant torque on ZMP at $t_s - 1$, $\mathbf{Rot} = [\theta \ \phi \ \psi]^T$ and \mathbf{K} is the stiffness matrix of the soft sole.

From the ZMP definition, we have:

$$\Gamma_{\mathbf{P}_{ZMP}} = \begin{bmatrix} \Gamma_{\mathbf{P}_{ZMP},t_1} = 0 \\ \Gamma_{\mathbf{P}_{ZMP},t_2} = 0 \\ \Gamma_{\mathbf{P}_{ZMP},n} \end{bmatrix} = \sum_{\beta=1}^{c_n} \begin{bmatrix} (P_{\beta,t_2} - P_{ZMP,t_2}) \cdot F_{\beta,n} \\ -(P_{\beta,t_1} - P_{ZMP,t_1}) \cdot F_{\beta,n} \\ (P_{\beta,t_1} - P_{ZMP,t_1}) \cdot F_{\beta,t_2} - (P_{\beta,t_2} - P_{ZMP,t_2}) \cdot F_{\beta,t_1} \end{bmatrix} \quad (4.12)$$

where the subscripts t_1 and t_2 denote respectively the first and second component of the vector.

To solve the problem (4.11), we use a Newton's method. A differential relationship between $(\mathbf{F}_{ZMP}, \mathbf{P}_{ZMP}, \Gamma_{\mathbf{P}_{ZMP},n})$ and $(\mathbf{O}_l, \mathbf{Y})$ is used to derive a Newton step:

$$\begin{bmatrix} \mathbf{O}_l^{(t_s)} \\ \mathbf{Y}^{(t_s)} \end{bmatrix} = \begin{bmatrix} \mathbf{O}_l^{(t_s-1)} \\ \mathbf{Y}^{(t_s-1)} \end{bmatrix} - \mathbf{K}^{-1} \begin{bmatrix} \mathbf{F}_{ZMP}^{(t_s-1)} - \mathbf{F}_{ZMP}^d \\ \mathbf{P}_{ZMP}^{(t_s-1)} - \mathbf{P}_{ZMP}^d \\ \Gamma_{\mathbf{P}_{ZMP},n} \end{bmatrix} \quad (4.13)$$

Considering \mathbf{F}_α , δ_α , \mathbf{O}_l and (θ, ϕ, ψ) as variables, the differential of (B.8) is:

$$\begin{aligned} d\delta_\alpha &= d\mathbf{O}_l + \sum_{\beta=1}^m \mathbf{W}_{\alpha\beta} d\mathbf{F}_\beta \\ &+ \left(\frac{\partial \mathbf{R}}{\partial \theta} \mathbf{P}_\alpha^{free} + \sum_{\beta=1}^m \left(\frac{\partial \mathbf{R}}{\partial \theta} \mathbf{C}_{\alpha\beta} \mathbf{R}^T + \mathbf{R} \mathbf{C}_{\alpha\beta} \frac{\partial \mathbf{R}^T}{\partial \theta} \right) \mathbf{F}_\beta \right) d\theta \\ &+ \left(\frac{\partial \mathbf{R}}{\partial \phi} \mathbf{P}_\alpha^{free} + \sum_{\beta=1}^m \left(\frac{\partial \mathbf{R}}{\partial \phi} \mathbf{C}_{\alpha\beta} \mathbf{R}^T + \mathbf{R} \mathbf{C}_{\alpha\beta} \frac{\partial \mathbf{R}^T}{\partial \phi} \right) \mathbf{F}_\beta \right) d\phi \\ &+ \left(\frac{\partial \mathbf{R}}{\partial \psi} \mathbf{P}_\alpha^{free} + \sum_{\beta=1}^m \left(\frac{\partial \mathbf{R}}{\partial \psi} \mathbf{C}_{\alpha\beta} \mathbf{R}^T + \mathbf{R} \mathbf{C}_{\alpha\beta} \frac{\partial \mathbf{R}^T}{\partial \psi} \right) \mathbf{F}_\beta \right) d\psi \\ &= d\mathbf{O}_l + \sum_{\beta=1}^m \mathbf{W}_{\alpha\beta} d\mathbf{F}_\beta + v^\theta + v^\phi + v^\psi \end{aligned} \quad (4.14)$$

Following the Coulomb's law, we can distinguish two contact cases for each contact node α :

1. **Stick:**

$$\boldsymbol{\delta}_\alpha = \mathbf{0} \rightarrow d\boldsymbol{\delta}_\alpha = \mathbf{0} \quad (4.15)$$

2. **Slip:** For each contact, we have three equations given by (4.14) and three equations given by the differential of the Coulomb's law (B.12).

Using these considerations, we can write the following system that relates contact forces and distance of interpenetration to the foot position and orientation:

$$\begin{bmatrix} \mathbf{A}_{11} & \mathbf{A}_{12} \\ \mathbf{A}_{21} & \mathbf{A}_{22} \end{bmatrix} \begin{bmatrix} d\mathbf{F} \\ d\boldsymbol{\delta} \end{bmatrix} = \mathbf{A} \begin{bmatrix} d\mathbf{F} \\ d\boldsymbol{\delta} \end{bmatrix} = \mathbf{B} \begin{bmatrix} d\mathbf{O}_l \\ d\mathbf{Rot} \end{bmatrix} = \begin{bmatrix} \mathbf{B}_{11} & \mathbf{B}_{12} \\ \mathbf{0}_{3s \times 3} & \mathbf{0}_{3s \times 3} \end{bmatrix} \begin{bmatrix} d\mathbf{O}_l \\ d\mathbf{Rot} \end{bmatrix} \quad (4.16)$$

where m is the number of contacts, s is the number of contacts in slip case, $p(j)$ $j \in [1 \dots s]$ is the j^{th} slip contact and:

$$\left\{ \begin{array}{l} \mathbf{A}_{11} = -\mathbf{W}, \mathbf{A}_{12} = [\mathbf{a}_1 \dots \mathbf{a}_j \dots \mathbf{a}_s], \\ \mathbf{a}_j = [\mathbf{0}_{3 \times 3}^1 \dots \mathbf{I}_{3 \times 3}^{p(j)} \dots \mathbf{0}_{3 \times 3}^s]^T, \forall j \in [1 \dots s] \\ \mathbf{A}_{21} = [\mathbf{c}_1^T \dots \mathbf{c}_j^T \dots \mathbf{c}_s^T]^T, \forall j \in [1 \dots s] \\ \mathbf{c}_j = \left[\mathbf{0}_{3 \times 3}^1 \dots \begin{bmatrix} \frac{\partial \Phi_3}{\partial \mathbf{F}_t} & \frac{\partial \Phi_3}{\partial \mathbf{F}_n} \end{bmatrix}^{p(j)} \dots \mathbf{0}_{(3 \times 3)}^m \right] \\ \mathbf{A}_{22} = \text{diag}(d_j), d_j = \begin{bmatrix} \frac{\partial \Phi_3}{\partial \boldsymbol{\delta}_t} & \mathbf{0}_{2 \times 1} \\ \mathbf{0}_{1 \times 2} & q_n \end{bmatrix} \\ \mathbf{B}_{11} = [\mathbf{I} \dots \mathbf{I}]^T \\ \mathbf{B}_{12} = [\mathbf{b}_1 \dots \mathbf{b}_i \dots \mathbf{b}_m]^T, \text{ with } \forall i \in [1 \dots m] \\ \mathbf{b}_i = \begin{bmatrix} v_i^\theta \\ v_i^\phi \\ v_i^\psi \end{bmatrix} \end{array} \right.$$

Using (4.16), we can find the following relationship:

$$\begin{aligned}
\begin{bmatrix} d\mathbf{F}_{tot} \\ d\mathbf{Z} \\ d\Gamma_{Z,n} \end{bmatrix} &= \begin{bmatrix} \mathbf{D}_{11} & \mathbf{0}_{3 \times 3s} \\ \mathbf{D}_{21} & \mathbf{D}_{22} \end{bmatrix} \begin{bmatrix} d\mathbf{F} \\ d\boldsymbol{\delta} \end{bmatrix} \\
&= \mathbf{DA}^{-1}\mathbf{B} \begin{bmatrix} d\mathbf{O}_l \\ d\mathbf{Rot} \end{bmatrix} \\
&= \mathbf{K} \begin{bmatrix} d\mathbf{O}_l \\ d\mathbf{Rot} \end{bmatrix}
\end{aligned} \tag{4.17}$$

To compute the Stiffness matrix $\mathbf{K} = \mathbf{DA}^{-1}\mathbf{B}$, we need to find the matrix \mathbf{D} .

The differential of (4.12) is:

$$\left\{ \begin{array}{l} \sum_{\beta=1}^m \frac{\partial \mathbf{P}_{\beta,t_2}}{\partial \delta_{\beta,t_2}} d\delta_{\beta,t_2} \mathbf{F}_{\beta,n} + \sum_{\beta=1}^m (\mathbf{P}_{\beta,t_2} - \mathbf{Z}_{t_2}) dF_{\beta,n} - d\mathbf{Z}_{t_2} \sum_{\beta=1}^m F_{\beta,n} = 0 \\ - \sum_{\beta=1}^m \frac{\partial \mathbf{P}_{\beta,t_1}}{\partial \delta_{\beta,t_1}} d\delta_{\beta,t_1} \mathbf{F}_{\beta,n} - \sum_{\beta=1}^m (\mathbf{P}_{\beta,t_1} - \mathbf{Z}_{t_1}) dF_{\beta,n} + d\mathbf{Z}_{t_1} \sum_{\beta=1}^m F_{\beta,n} = 0 \\ \left(\sum_{\beta=1}^m \frac{\partial \mathbf{P}_{\beta,t_1}}{\partial \delta_{\beta,t_1}} d\delta_{\beta,t_1} \mathbf{F}_{\beta,t_2} + \sum_{\beta=1}^m (\mathbf{P}_{\beta,t_1} - \mathbf{Z}_{t_1}) dF_{\beta,t_2} - d\mathbf{Z}_{t_1} \sum_{\beta=1}^m F_{\beta,t_2} + \right. \\ \left. - \sum_{\beta=1}^m \frac{\partial \mathbf{P}_{\beta,t_2}}{\partial \delta_{\beta,t_2}} d\delta_{\beta,t_2} \mathbf{F}_{\beta,t_1} - \sum_{\beta=1}^m (\mathbf{P}_{\beta,t_2} - \mathbf{Z}_{t_2}) dF_{\beta,t_1} + d\mathbf{Z}_{t_2} \sum_{\beta=1}^m F_{\beta,t_1} \right) = d\Gamma_{Z,n} \end{array} \right. \tag{4.18}$$

where $\frac{\partial \mathbf{P}_{\beta,t}}{\partial \delta_{\beta,t}} = I$.

Therefore, each block component of the matrix \mathbf{D} in (4.17) is $\forall i \in [1 \cdots m]$:

$$\left\{ \begin{array}{l} \mathbf{D}_{11} = \begin{bmatrix} I_{3 \times 3}^1 & \cdots & I_{3 \times 3}^i & \cdots & I_{3 \times 3}^m \end{bmatrix} \\ \mathbf{D}_{21} = \begin{bmatrix} d_1 & \cdots & d_i & \cdots & d_m \end{bmatrix}, \\ d_i = \begin{bmatrix} 0 & 0 & \frac{1}{\mathbf{F}_{tot,n}} (\mathbf{P}_{i,t_1} - \mathbf{Z}_{t_1}) \\ 0 & 0 & \frac{1}{\mathbf{F}_{tot,n}} (\mathbf{P}_{i,t_2} - \mathbf{Z}_{t_2}) \\ (-\mathbf{P}_{i,t_2} + \mathbf{Z}_{t_2}) & (\mathbf{P}_{i,t_1} - \mathbf{Z}_{t_1}) & 0 \end{bmatrix} \\ \mathbf{D}_{22} = \begin{bmatrix} \mathbf{e}_1 & \cdots & \mathbf{e}_i & \cdots & \mathbf{e}_s \end{bmatrix}, \\ \mathbf{e}_i = \begin{bmatrix} \frac{1}{\mathbf{F}_{tot,n}} F_{i,n} & 0 & 0 \\ 0 & \frac{1}{\mathbf{F}_{tot,n}} F_{i,n} & 0 \\ F_{i,t_2} & -F_{i,t_1} & 0 \end{bmatrix} \end{array} \right.$$

where $\mathbf{F}_{tot,n} = \sum_{\beta=1}^m \mathbf{F}_{\beta,n}$.

Algorithm 1: ZMP force and position algorithm. $\varepsilon_4, \varepsilon_5$ are respectively the desired accuracy for ZMP position and force

Input: $\delta^{free}, \mathbf{W}$
Output: \mathbf{F}
if $q = 1$ **then**
 $\mathbf{F} = \mathbf{0}$
if $q = 2 \dots h$ **then**
 $\mathbf{F} = \mathbf{F}^{(q-1)}$
do
 Friction contact algorithm (2)

$$\begin{bmatrix} d\mathbf{O}_l \\ d\mathbf{Rot} \end{bmatrix} = \mathbf{K}^{-1} \begin{bmatrix} \mathbf{F}_{des} - \mathbf{F}_{tot} \\ \mathbf{Z}_{des} - \mathbf{Z} \\ -\Gamma_{Z,n} \end{bmatrix}$$
 $\mathbf{O}_l = d\mathbf{O}_l + \mathbf{O}_l$
 $\boldsymbol{\theta} = d\boldsymbol{\theta} + \boldsymbol{\theta}$
 $\boldsymbol{\phi} = d\boldsymbol{\phi} + \boldsymbol{\phi}$
 $\boldsymbol{\psi} = d\boldsymbol{\psi} + \boldsymbol{\psi}$
while $\|\mathbf{Z}_{des} - \mathbf{Z}\| > \varepsilon_4$ **OR** $\|\Gamma_{Z,n}\| > \varepsilon_4$ **OR** $\|\mathbf{F}_{des} - \mathbf{F}_{tot}\| > \varepsilon_5$

The algorithm in Fig. 4.5 loops on frictional contact problem followed by a Newton step that gives a new foot position and orientation. To increase the speed of the algorithm, the precision of the frictional contact problem is increased with the convergence of the Newton steps.

4.2.5 Initial conditions

During the SSP, ankle positions and orientations of the foot in the air are computed by interpolating with 5th order polynomials the absolute ankle orientation, position, velocity and acceleration between take-off and landing phases.

The previous problem is solved by imposing the initial conditions on position $\mathbf{O}_l^{\text{init}}$ and yaw orientation $\boldsymbol{\psi}^{\text{init}}$ of the foot. They are set at $t_s = 0$ to compute the first reference contact position \mathbf{Q} . Initial roll and pitch orientation could be discontinuous to fulfill the desired ZMP position. Thus initial roll and pitch orientation of the foot are set as those obtained from the desired ZMP position. The Newton step (4.13) at the first time is changed accordingly to the tangential reference contact positions:

$$\mathbf{Q}_t = t\mathbf{O}_l^{\text{init}} + t\mathbf{R}^{\text{init}}(\boldsymbol{\theta}, \boldsymbol{\phi}, \boldsymbol{\psi}^{\text{init}}) {}^l\mathbf{P}_\alpha^{\text{free}} \quad (4.19)$$

4.3 DE validation with experiments on HRP-4

Now we present and analyze the results of our DE. We implemented and tested our obtained walking motion in experiments conducted with the HRP-4 robot wearing our specially designed feet with soft sole.

For the experiments with HRP-4, we considered only straight line walking for 0.5m with 10 steps. This is enough to have non-biased results and to assess the DE model which takes into account the trajectories of ZMP_1 and ZMP_2 .

4.3.1 Multi-objective quadratic program controller

The reference trajectories for the COM, the ankle position and orientation are obtained offline. Those references are online tracked as good as possible by a QP that takes also into account the robot constraints. The obtained motions are then compatible with the COM dynamics and the model of the flexibility. A task-space QP formulation with a weighted hierarchy [42] is used to generate the whole body motion. The optimization variables are $\mathbf{x} = [\dot{\mathbf{q}}^T \boldsymbol{\lambda}^T]^T$ where $\dot{\mathbf{q}}$ is the joint acceleration vector and $\boldsymbol{\lambda}$ is the force intensity along with the linearized friction cone.

The QP is formulated as follows:

$$\min_{\mathbf{x}} \left(\frac{1}{2} \mathbf{x}^T \mathbf{M} \mathbf{x} + \mathbf{c}^T \mathbf{x} \right) = \min_{\mathbf{x}} \sum_{i=1}^N \alpha_i \|E_i(\mathbf{x})\|^2 + \alpha_\lambda \|\boldsymbol{\lambda}\|^2$$

where N is the number of tasks put in the cost part, $E_i(\mathbf{x})$ is the task errors, α_i is the task weight and $\alpha_\lambda \|\boldsymbol{\lambda}\|^2$ is a damping term to ensure positive definite Hessian matrix.

From [42], the tasks put as constraints are:

1. **Joint torque limits**
2. **Joint position/velocity limits**
3. **No-sliding contacts:** zero acceleration for the contact body i
4. **Collision avoidance**

More specifically, the tasks we used are:

1. **Ankle:** desired ankle trajectories in position and orientation given by the DE
2. **COM:** tracking of the desired COM position, velocity and acceleration given by the WPG

3. **Torso:** fixed torso absolute orientation
4. **Posture:** fixed posture for the whole upper body (torso, head, and arms)

Such tracking results into a kinematic motion and an open-loop walking control of the robot.

4.3.2 HRP-4 walking with soft sole using the new controller

Here, we show the results of walking experiments with the HRP-4's new feet illustrated in Fig. 4.6. We removed the original shock absorbing springs located in the ankle (hence the ankle leg link is rigid) and added a flexible sole to absorb the landing impact shock and eventually cast terrain uncertainties. To do this experiments we used the WPG (chapter 3) and DE (chapter 4) explained before.



Figure 4.6 (a): new HRP-4's feet; (b): photo of HRP-4's feet with flexible soles

The sole material is a flexible foam. Coupling compression test and FEM simulation, we obtained the Young's modulus $E = 0.32\text{MPa}$ and Poisson's ratio $\nu = 0.31$ of the sole (which is softer than flexible soles used in [16] where Young's modulus were 5MPa , so that an estimator was not necessary).

Experiments consisted of HRP-4's straightforward walking for 10 footsteps (distance of 0.5 m) with average speeds of 3.5 cm/s and 4.2 cm/s. To validate our control framework in Fig. 4.2, we used ZMP and COM trajectories obtained using the WPG described in chapter 3 with $\lambda = 0.8$ and $\mu = 15$ in (3.5). These trajectories are shown in Fig. 4.7a. Fig. 4.7b shows the ankle trajectories when the foot is not in contact with the floor.

From the inverse pendulum model and the ZMP equation in [28], the COM acceleration is an image of the ZMP position in the COM frame (ignoring a multiplication factor). To avoid noisy force measurements due to the impact-shock at the landing phase or drift from

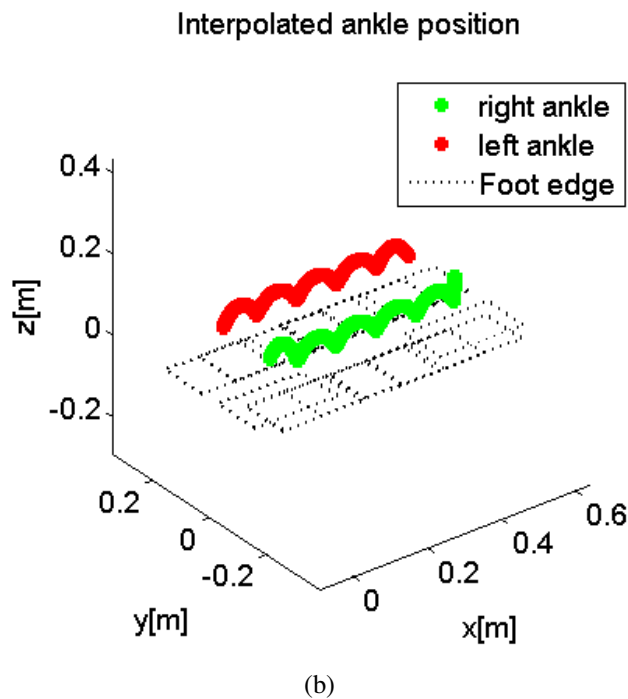
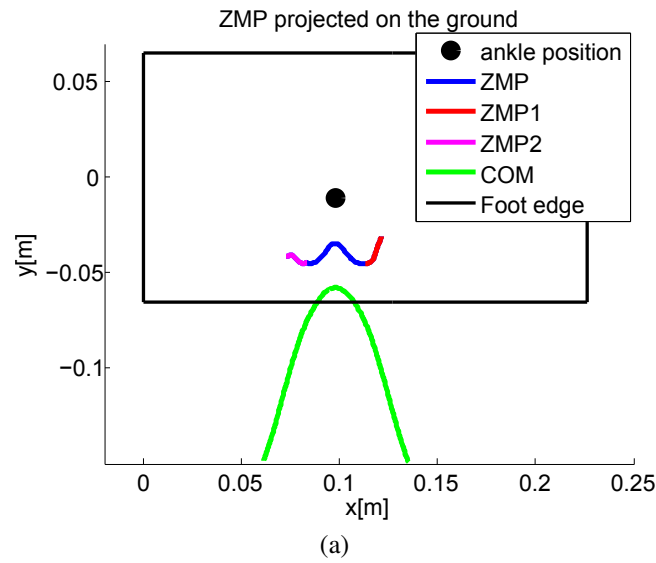


Figure 4.7 (a): ZMP trajectory under the left foot and COM trajectory during the 6th foot step (SSP+DSP); (b): ankle trajectories when the foot is not in contact with the floor

acceleration integration, we focused on the analysis of the COM acceleration given by the robot Inertia Measurement Unit (IMU).

Finally, to find the best weight values in (3.5), we performed experiments on the HRP-4 with different weights using the new control framework in Fig. 4.2. Experiments consisted of humanoid walking with four different values of $\lambda = \{0.2, 0.4, 0.6, 0.8\}$ in (3.5), robot

performed a straightforward walking for 10 footsteps (distance of 0.5 m) with average speed of 3.5 cm/s.

4.3.3 Results

Fig. 4.8 shows the COM acceleration given by the robot Inertia Measurement Unit (IMU) for the experiment with the flexible foam. When we used the DE, the COM acceleration along the y -axis is close to the reference acceleration (see Fig. 4.8b). On the contrary, the COM acceleration along x -axis and z -axis are quite different from the reference acceleration (see Figs. 4.8a and 4.8c).

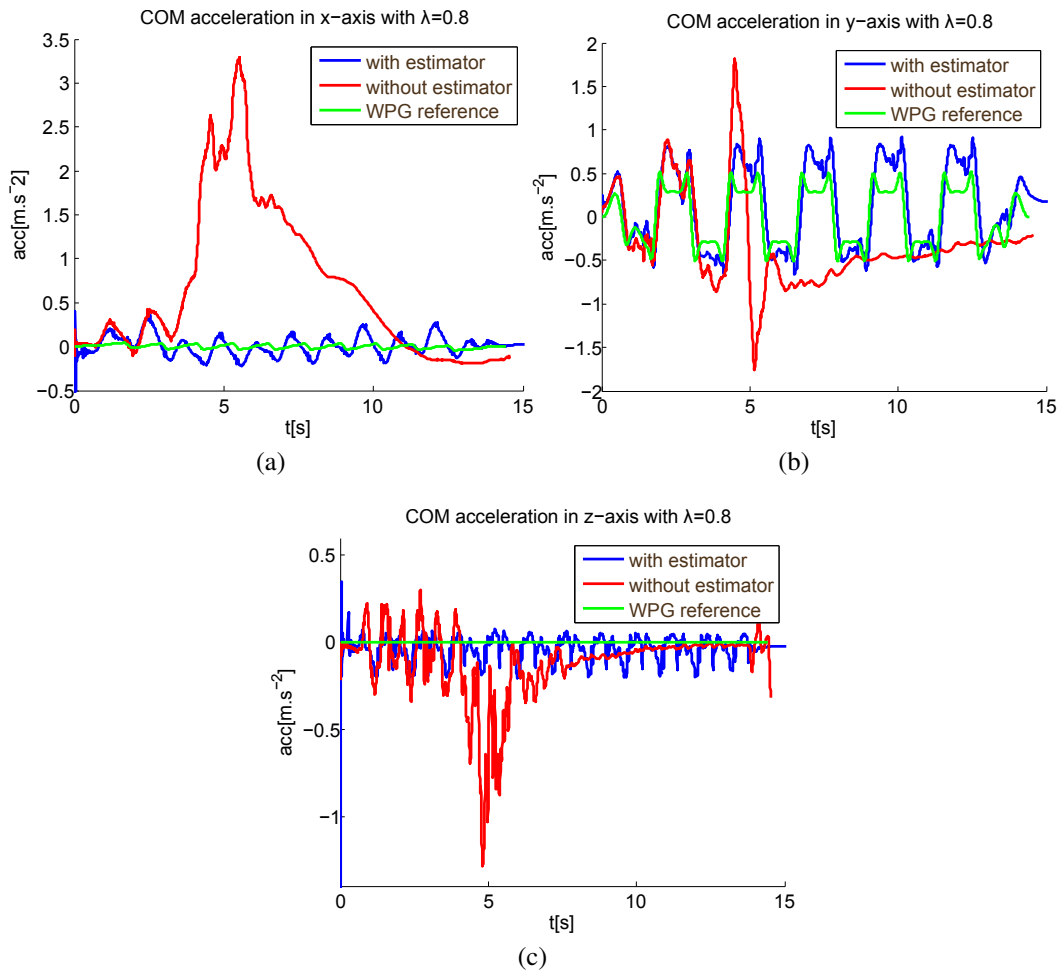


Figure 4.8 COM acceleration compared to the reference acceleration along $x/y/z$ axes with and without the deformation estimator (DE).

Fig. 4.9 shows the norm of horizontal ground reaction forces (GRF) and the vertical GRF measured with and without the DE. We can see that the forces measured are closed to the reference when using the DE.

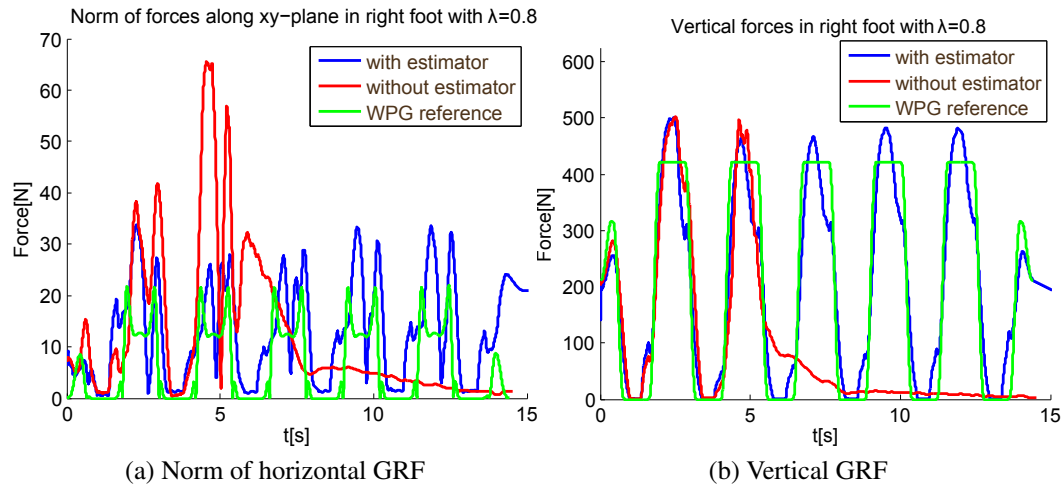


Figure 4.9 Norm of horizontal ground reaction forces and the vertical ground reaction forces measured with and without the DE in right foot.

Fig. 4.10 shows the right ankle position along $x/y/z$ axes in the COM frame to avoid acceleration integration drift of the robot position in the world frame. The measures are almost confound with the reference when using the DE.

Fig. 4.11 shows the ankle angle orientation along $x/y/z$ axes with and without the DE. The measurements are closed to the reference when using DE.

When we did not use the DE, the robot fell down. The problem of the reference tracking is clearly identifiable around 4 s in any Figures 4.8 to 4.11.

The Fig. 4.12 shows the right foot ankle torques for different values of the WPG (results are similar for the left foot). Theoretical ankle torques increase with λ since the weight given to the criterion dependent on the ankle torque decreases. Analyzing the Fig. 4.12, we can make the following observations:

- For $\lambda = 0.2$, the mean torque is bigger than the theoretical one. In this case, the ZMP trajectory of each foot is shorter than for $\lambda > 0.2$ and it is close to the ankle position (see Fig. 4.7a). This position of the ZMP must be more difficult to stabilize because it is the position of minimum sole flexibility when all the foam is equally (fully) compressed.
- From $\lambda = 0.4$ to $\lambda = 0.6$, mean torques are close to theoretical ones.

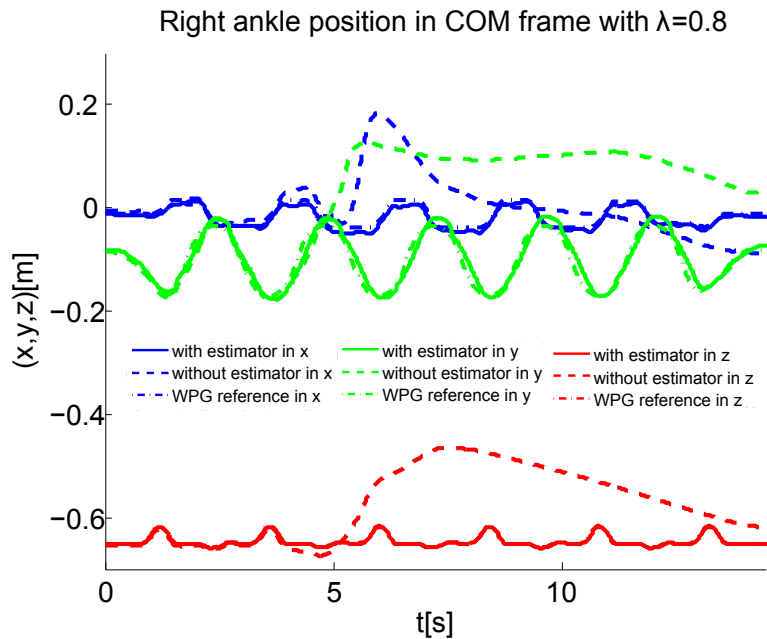


Figure 4.10 Right ankle position along x/y/z axes in the COM frame.

- For $\lambda = 0.8$, mean torques are lower than theoretical one. In this case, the ZMP trajectory of each foot is closer to the edge of the feet, which makes it difficult to move it further to the edge to stabilize the robot. Hence this walk is not as stable as for $\lambda = 0.4$ and $\lambda = 0.6$. Maximum ankle torques are then larger, but we have no explanation why the mean torque is lower than the theoretical one.
- Maximum ankle torques have a similar evolution to the theoretical mean ankle torques.

Fig. 4.13 shows the COM accelerations (which is also the image of COM force). In (3.5), λ mainly affect the COM acceleration in the lateral direction. Theoretical COM acceleration decreases with λ since the weight given to the minimization of the criterion depends on the COM force increase. Analyzing the Fig. 4.13, we can make the following observations:

- From $\lambda = 0.2$ to $\lambda = 0.6$, the evolution of COM acceleration is similar to the theoretical one, albeit with some variations due to the HRP-4 built-in stabilizer
- For $\lambda = 0.8$, the COM acceleration is not decreasing for the same reason as before; it is a case more difficult to stabilize.

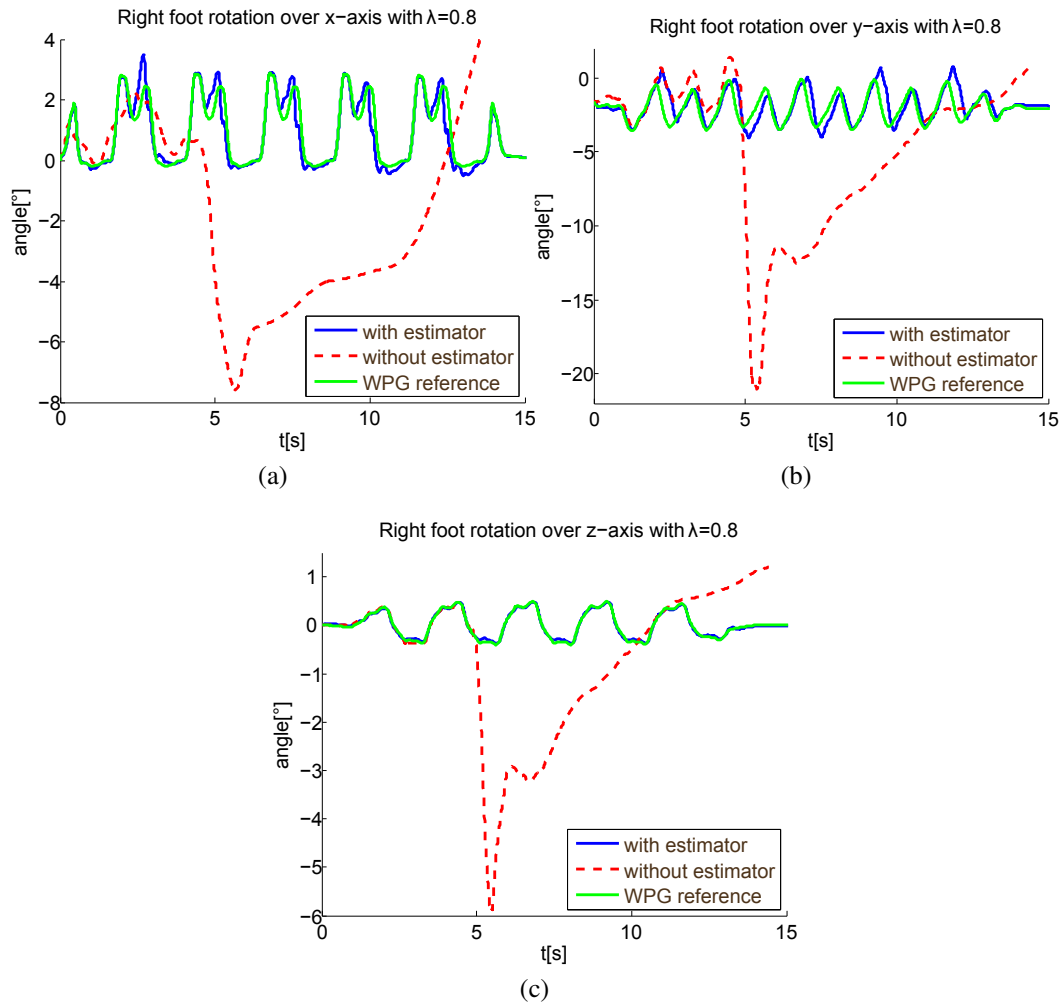


Figure 4.11 Ankle orientation along x/y/z axes with and without the DE.

4.3.4 Discussion

The video² and Figures 4.8 to 4.11 clearly show the improvements given by the control scheme in Fig. 4.2. Indeed, without the DE, it is impossible to walk with the soft soles under the robot feet which induce too much instabilities that cannot be compensated by the HRP-4's built-in stabilizer: a black box that adjust the desired robot state from the ones we compute and tuned for the original feet design. Hence, it does not take into account the new sole flexibilities.

When we don't use the DE, the built-in stabilizer effect is clearly visible in Fig. 4.11. In that case, the foot rotation reference is constant and equal to 0 rad along any axes. However, foot rotation is generated far from the predicted stable reference given by the DE. This effect is clearly visible in Figures 4.11a to 4.11b along x- and y-axes.

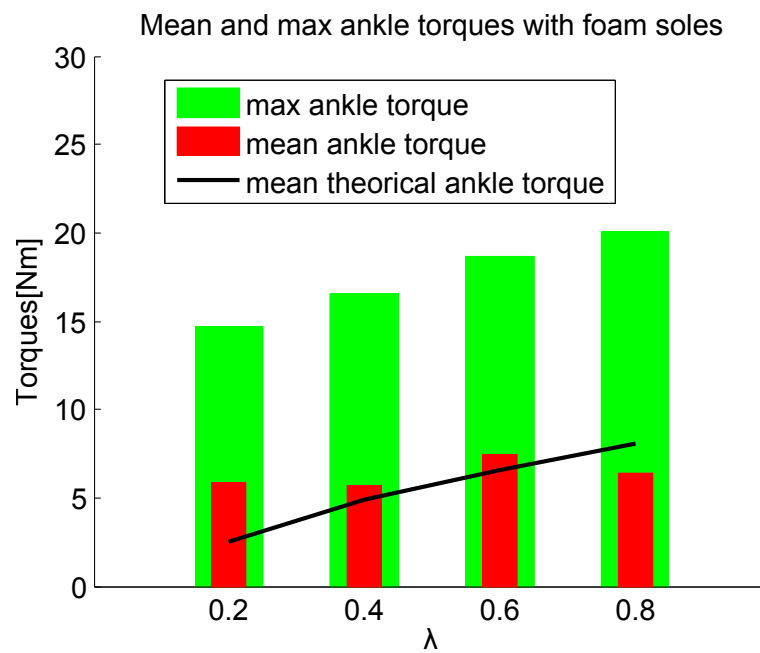


Figure 4.12 Ankle torque for different cost functions.

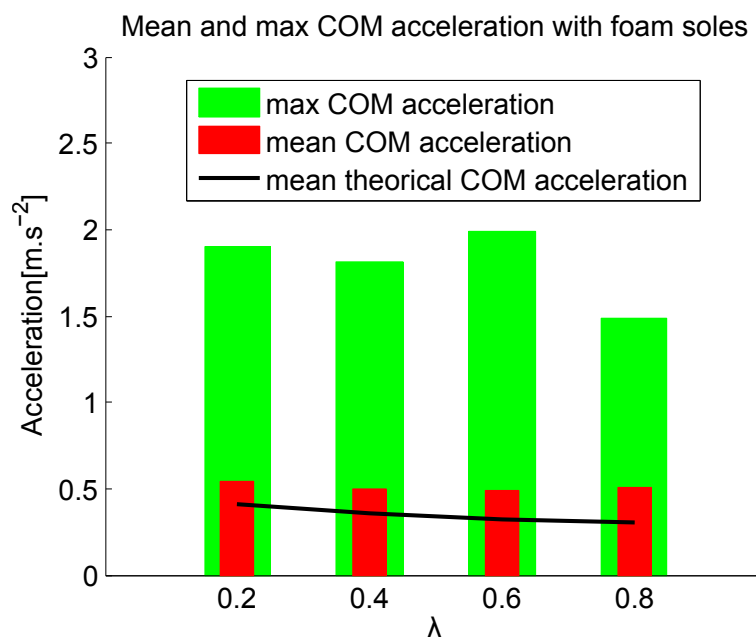


Figure 4.13 COM acceleration for different cost functions.

We looked also at the ankle force to validate our control framework in Fig. 4.2. As we can see from Figs. 4.9a and 4.9b, our controller estimates well the forces. As we can see in Fig. 4.10, we also obtained ankle positions close to reference, which shows that the stabilizer does not need to change a lot the relative feet and waist positions to obtain stability, and this is thanks to the estimator.

The most important estimation of our new controller to enhance ZMP stabilization is given on foot orientations in Figs. 4.11a, 4.11b and 4.11c (in particular along x - and y -axes) that are well followed by the robot and are used to help the built-in stabilizer. We can therefore state that our novel WPG and DE are a good model of the robot with flexible foam soles and enhances the native stabilizer to keep the desired robot attitude during the walking task.

To choose experimentally the best weight λ of the cost function (3.5), we analyzed the ankle torques (Fig. 4.12) and COM accelerations (Fig. 4.13). The theoretical values are obtained from the WPG without taking into account the flexibility.

With hard soles, we don't need the deformation estimator to perform humanoid walking [16]. Using the soft sole in Fig. 4.6 (flexible foam with a low elastic modulus), we need the deformation estimator to enhance the robot stabilization.

Additionally, some instability can be observed in the video² with new feet when the ZMP is close to the foot edge, while with old feet it is more stable. In chapter 5, we will improve the sole flexibility stabilization control scheme that was tuned for the old feet system.

4.4 Conclusion

We investigated adding only flexible soles to a humanoid robot as compliant elements. Using a new control framework, we validate our approach on the HRP-4 robot. Experiments showed how our new WPG and deformation estimator (DE) enhances the ZMP stabilization during humanoid walking with flexible/soft soles. We modeled the contact between the sole and the ground using a FEM model of the sole and a contact model accounting for both Signorini's and Coulomb's laws. These models are taken into account in the DE and experimentally validated.

However, the computation time of our DE is slow which implies that all the motion is generated offline and directly played on the robot. Such method inhibits the robot reactivity to correct errors on trajectory and deal with perturbations which can both induce instabilities. In chapter 5, we developed a new closed-loop framework with a simplification of our DE to obtain online computation of sole deformation compensation and stabilize the robot during walking.

Chapter 5

A closed-loop controller to walk with soft soles

In order to take into account the deformation of soft soles during walking, we developed a deformation estimator (DE in chapter 4) coupled with a corresponding Walking Pattern Generator (WPG in chapter 3). This DE has been experimentally validated by successfully walking in open-loop with HRP-4 performing different experiments 4.3. However, its time-consuming computations prevented its application to online motion generation and to deal with perturbations. Hence, we need to develop a closed-loop controller to track the reference motion and obtain a robust walk with soft soles.

Abstract

Soft soles absorb impacts and cast ground unevenness during locomotion on rough terrains. However, they introduce passive degrees of freedom (deformations under the feet) that complexify the tasks of state estimation and overall robot stabilization.

In this chapter, we develop a closed-loop controller for biped robots walking with soft soles on flat and uneven terrain. The goal of this controller is to minimize the tracking error in terms of COM velocity, COM and ZMP position with an admittance control of the feet based on a simple deformation estimator of materials under the feet. This results into an admittance control at the ankles whose gains are based on the sole stiffness in a nominal state from the FEM model.

We tested our approach on a humanoid robot HRP-4 walking on gravel, as depicted in Figure 5.1.

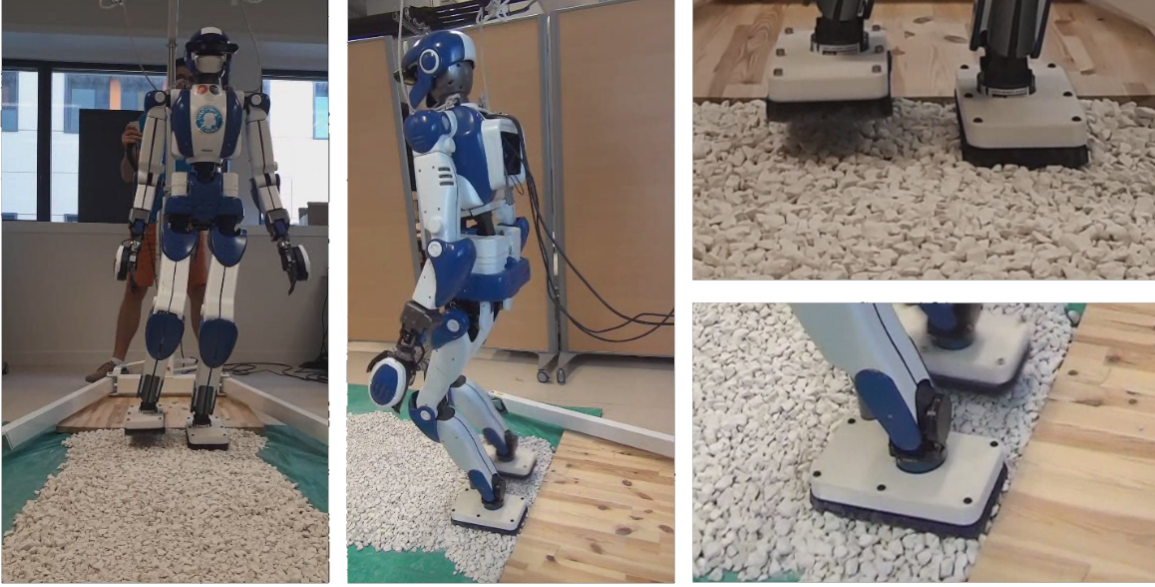


Figure 5.1 Different views of HRP-4 walking on gravel with soft soles.

5.1 Control framework structure

The control framework 4.2 used in chapter 4 has no control feedback and all the motion is planned offline which inhibit reactivity to correct the motion.

A new control pipeline with closed loop is illustrated in Figure 5.2. Superscripts d are used to denote desired references and i control references when the subscript $i \in \{R, L\}$ denotes in this chapter right or left foot references. This pipeline goes as follows:

- A walking pattern generator (WPG) [16, 17] outcomes desired COM $\mathbf{P}_{\text{COM}}^d$ and ZMP $\mathbf{P}_{\text{ZMP}}^d$ trajectories, along with the desired COM velocity $\dot{\mathbf{P}}_{\text{COM}}^d$ and the stiffness matrix of the soft sole \mathbf{J}_i .
- A ZMP-COM tracking controller (Section 5.2) generates a control whole-body ZMP $\mathbf{P}_{\text{ZMP}}^c$ that compensates both COM and ZMP errors between measurements and their respective WPG references.
- A ZMP-force distribution layer (Section 5.3) converts it into centers of pressure (CoP) under each foot in contact $\mathbf{P}_{\text{CoP}_i}^c$, while the net reaction forces \mathbf{F}^c is similarly distributed into contact forces \mathbf{F}_i^c .
- A reaction-force control layer (Section 5.4) updates foot positions \mathbf{P}_i^d and orientations Θ_i^d to achieve the desired $\mathbf{P}_{\text{CoP}_i}^c$ and \mathbf{F}_i^c using admittance control [51].

Finally, a quadratic-programming (QP) whole-body controller finally produces joint motions that track the CoM and foot reference trajectories [52] from the force control layer and the COM trajectory.

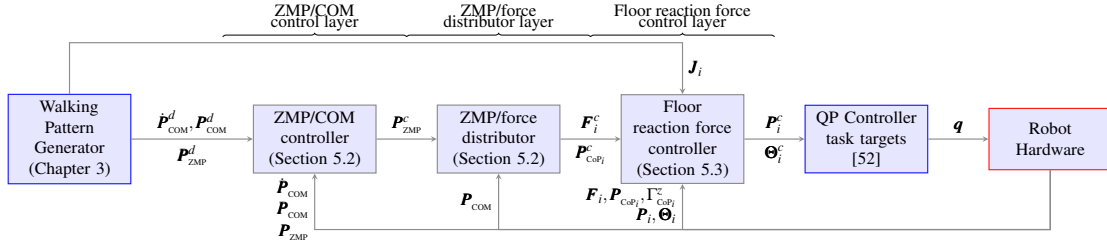


Figure 5.2 *Overview of the control loop.* Superscripts d and c denote desired and control references, respectively, while robot measurements have none. $i \in \{R, L\}$ stands for right or left foot. \mathbf{P} refers to positions, \mathbf{F} to forces and Θ to orientations.

Such control framework is inspired by those in [53, 54]. Our different layers are detailed in the followed sections. In the ZMP-COM control layer, instead of a proportional and integral control feedback on the capture point, we chose to use a proportional control feedback on COM position and velocity when we use an integral control feedback only on COM position. This allow us to suppress the residual COM static error. The ZMP-force distributor layer is based on the minimization of torques in ankles instead of a simple heuristics. Finally, instead of a damping control of foot force and torque decoupled, we use an admittance control of the foot where the force and CoP under each foot (equivalent to torque in ankle) are coupled with a 6×6 stiffness matrix.

5.2 ZMP-COM control layer

Our ZMP-COM control layer is based on [55, 53, 54]. We define a feedback controller on the state $\mathbf{x} = [x_{\text{COM}} \dot{x}_{\text{COM}} x_{\text{ZMP}}]^T$ of COM position, COM velocity and ZMP position. We then proceed by pole placement in order to obtain the best COM-ZMP regulator [55], which is equivalent to a capture-point tracking controller [54].

5.2.1 Linear inverted pendulum model

The trajectories output by our WPG are:

$$\mathbf{P}_{\text{COM}}^d(t) = \begin{bmatrix} x_{\text{COM}}^d(t) \\ y_{\text{COM}}^d(t) \\ z_c \end{bmatrix}, \mathbf{P}_{\text{ZMP}}^d(t) = \begin{bmatrix} x_{\text{ZMP}}^d(t) \\ y_{\text{ZMP}}^d(t) \\ 0 \end{bmatrix} \quad (5.1)$$

where z_c is the COM height above the ground. As the COM and ZMP are bound by a holonomic constraint to stay inside horizontal planes, all computations on the x -axis can be readily reproduced for the y -axis. In this model, the relationship between ZMP position and COM acceleration is given by the cart-table model [28]:

$$\begin{aligned} \ddot{x}_{\text{COM}}(t) &= \frac{g}{z_c}(x_{\text{COM}}(t) - x_{\text{ZMP}}(t)) \\ &= \omega_c^2(x_{\text{COM}}(t) - x_{\text{ZMP}}(t)) \end{aligned} \quad (5.2)$$

with $g = 9.81 \text{ m}\cdot\text{s}^{-2}$ is the gravity constant.

To account for joint flexibilities and sole compliance, we assume that the real ZMP of the robot (\mathbf{P}_{ZMP}) lags behind the control ZMP ($\mathbf{P}_{\text{ZMP}}^c$). As in [53, 54], we model this delay as a low-pass filter whose transfer function is:

$$\mathbf{P}_{\text{ZMP}}(s) = \frac{1}{1 + sT_p} \mathbf{P}_{\text{ZMP}}^c(s) \quad (5.3)$$

where T_p is the low-pass time constant.

Let $\mathbf{x} = [x_{\text{COM}} \quad \dot{x}_{\text{COM}} \quad x_{\text{ZMP}}]^T$ denote the state vector for the x -axis. Combining (5.2) and (5.3) yields the linear time-invariant system in state-space representation:

$$\dot{\mathbf{x}}(t) = \mathbf{A}\mathbf{x}(t) + \mathbf{B}x_{\text{ZMP}}^c(t) \quad (5.4)$$

$$\text{with } \mathbf{A} = \begin{bmatrix} 0 & 1 & 0 \\ \omega_c^2 & 0 & -\omega_c^2 \\ 0 & 0 & -1/T_p \end{bmatrix} \text{ and } \mathbf{B} = \begin{bmatrix} 0 \\ 0 \\ 1/T_p \end{bmatrix}.$$

5.2.2 Pole placement for ZMP-COM tracking control

The following controller tracks the robot state \mathbf{x} following desired state \mathbf{x}^d given by the WPG. It eliminates the residual COM static error:

$$x_{\text{ZMP}}^c(t) = \mathbf{K}_I \mathbf{x}^d(t) - \mathbf{K}_r \mathbf{x}(t) - k_i \int_0^t (x_{\text{COM}}^d(t) - x_{\text{COM}}(t)) dt \quad (5.5)$$

with $\mathbf{K}_I = [k_{I1} \ k_{I2} \ k_{I3}]$, $\mathbf{K}_r = [k_{r1} \ k_{r2} \ k_{r3}]$ and k_i the state feedback gains. Figure 5.3 represents the block diagram of the controller. The system enhanced by the integrator is:

$$\begin{cases} \dot{\mathbf{x}}(t) = \mathbf{A}\mathbf{x}(t) + \mathbf{B}x_{\text{ZMP}}^c(t) \\ x_{\text{COM}}(t) = \mathbf{C}\mathbf{x}(t) \\ \dot{v}(t) = x_{\text{COM}}(t) - \mathbf{C}\mathbf{x}^d(t) \end{cases} \quad (5.6)$$

with $\mathbf{C} = [1 \ 0 \ 0]$. Taking $\bar{\mathbf{x}}(t) = [\mathbf{x}(t) \ v(t)]^T$, Equation (5.6) with the controller writes:

$$\begin{cases} \dot{\bar{\mathbf{x}}}(t) = \bar{\mathbf{A}}\bar{\mathbf{x}}(t) + \bar{\mathbf{B}}x_{\text{ZMP}}^c(t) + \bar{\mathbf{C}}\mathbf{x}^d(t) \\ x_{\text{ZMP}}^c(t) = -\bar{\mathbf{K}}\bar{\mathbf{x}}(t) + \mathbf{K}_I \mathbf{x}^d(t) \end{cases} \quad (5.7)$$

with

$$\begin{aligned} \bar{\mathbf{A}} &= \begin{bmatrix} \mathbf{A} & (0) \\ -\mathbf{C} & (0) \end{bmatrix} & \bar{\mathbf{B}} &= \begin{bmatrix} \mathbf{B} \\ (0) \end{bmatrix} \\ \bar{\mathbf{C}} &= \begin{bmatrix} (0) \\ \mathbf{C} \end{bmatrix} & \bar{\mathbf{K}} &= [\mathbf{K}_r \ k_i] \end{aligned} \quad (5.8)$$

The extended Equation (5.7) can then be rewritten:

$$\dot{\bar{\mathbf{x}}}(t) = (\bar{\mathbf{A}} - \bar{\mathbf{B}}\bar{\mathbf{K}})\bar{\mathbf{x}}(t) + (\bar{\mathbf{B}}\mathbf{K}_I + \bar{\mathbf{C}})\mathbf{x}^d(t) \quad (5.9)$$

In static mode, we have:

$$\begin{cases} \lim_{t \rightarrow +\infty} \bar{\mathbf{x}}(t) = \bar{\mathbf{x}}^\infty = [x_{\text{COM}}^\infty \ \dot{x}_{\text{COM}}^\infty \ x_{\text{ZMP}}^\infty \ v^\infty (=0)]^T \\ \lim_{t \rightarrow +\infty} \mathbf{x}^d(t) = \mathbf{x}^d = [x_{\text{COM}}^d \ x_{\text{COM}}^d \ x_{\text{ZMP}}^d]^T \\ 0 = (\bar{\mathbf{A}} - \bar{\mathbf{B}}\bar{\mathbf{K}})\bar{\mathbf{x}}^\infty + (\bar{\mathbf{B}}\mathbf{K}_I + \bar{\mathbf{C}})\mathbf{x}^d \end{cases}$$

This implies the gain relationships $k_{l1} = k_{r1}$, $k_{l2} = k_{r2}$ and $k_{l3} = 1 + k_{r3}$. Meanwhile, in a dynamic mode, we define the error as: $\bar{\mathbf{e}}(t) = \bar{\mathbf{x}}(t) - \bar{\mathbf{x}}^\infty$, so that:

$$\dot{\bar{\mathbf{e}}}(t) = (\bar{\mathbf{A}} - \bar{\mathbf{B}}\bar{\mathbf{K}})\bar{\mathbf{e}}(t) \quad (5.10)$$

In order to have a stable dynamic error that goes to zero in a limited amount of time, we need to choose the gains $\bar{\mathbf{K}}$ so that the matrix $(\bar{\mathbf{A}} - \bar{\mathbf{B}}\bar{\mathbf{K}})$ is stable. The choice of the gains $\bar{\mathbf{K}}$ are based on the eigenvalues $(\lambda_1, \lambda_2, \lambda_3, \lambda_4)$ of this matrix. From square matrices properties:

$$\begin{aligned} \text{Tr}(\bar{\mathbf{A}} - \bar{\mathbf{B}}\bar{\mathbf{K}}) &= -\frac{1+k_{r3}}{T_p} = \sum_{j=1}^4 \lambda_j \\ \det(\bar{\mathbf{A}} - \bar{\mathbf{B}}\bar{\mathbf{K}}) &= -\frac{\omega_c^2 k_i}{T_p} = \prod_{j=1}^4 \lambda_j \end{aligned} \quad (5.11)$$

Next, the eigenvalues of a square matrix being the roots of its characteristic polynomial $\det(\bar{\mathbf{A}} - \bar{\mathbf{B}}\bar{\mathbf{K}} - \lambda \mathbf{I})$, we have:

$$\begin{aligned} -\omega_c^2 - \frac{k_{r2}\omega_c^2}{T_p} &= -(\lambda_1\lambda_2 + \dots + \lambda_3\lambda_4) \\ -\frac{\omega_c^2}{T_p} - (k_{r1} + k_{r3})\frac{\omega_c^2}{T_p} &= (\lambda_1\lambda_2\lambda_3 + \dots + \lambda_2\lambda_3\lambda_4) \end{aligned}$$

The relation between eigenvalues and feedback gains is finally:

$$\begin{aligned} k_{r1} &= -k_{r3} - T_p \left(\frac{1}{T_p} - \frac{\lambda_1\lambda_2\lambda_3 + \dots + \lambda_2\lambda_3\lambda_4}{\omega_c^2} \right) \\ k_{r2} &= -T_p \left(1 + \frac{\lambda_1\lambda_2 + \dots + \lambda_3\lambda_4}{\omega_c^2} \right) \\ k_{r3} &= -T_p \sum_{j=1}^4 \lambda_j - 1 \\ k_i &= -\frac{T_p}{\omega_c^2} \prod_{j=1}^4 \lambda_j \end{aligned}$$

We conclude by noting that these eigenvalues are equal to the poles of the transfer function. From [55], in order to obtain the best ZMP-COM regulator, one eigenvalue must be equal to ω_c .

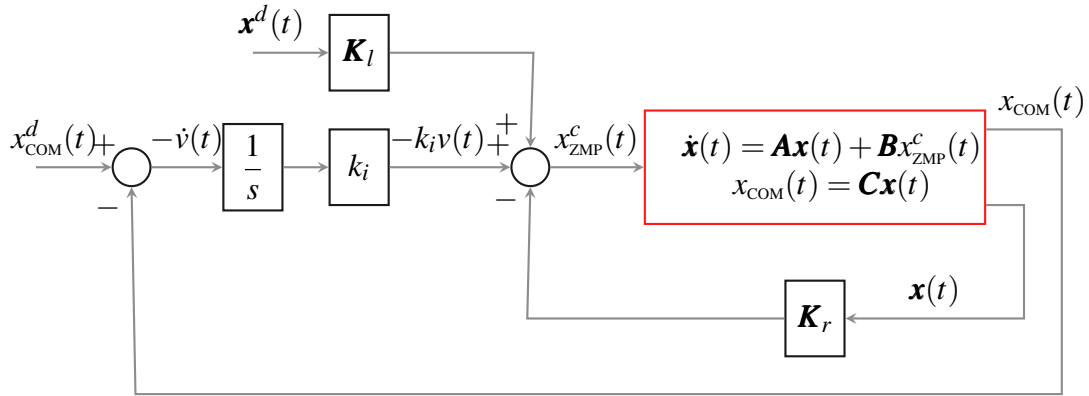


Figure 5.3 ZMP-COM tracking controller: the state reference \mathbf{x}^d of COM velocity, COM and ZMP position is compared to the measured state \mathbf{x} in order to control the system (in red) with a ZMP control x_{ZMP}^c

5.3 ZMP-force distribution layer

The ZMP-COM controller issues control through a single whole-body ZMP, regardless of contact-stability constraints, that is to say, without enforcing the conditions thanks to which contacts neither slip nor tilt during locomotion. The goal of the ZMP-force distribution layer is two-fold: (1) distribute whole-body ZMP and resultant force at each contact, so as to (2) enforce contact-stability conditions on a per-contact basis.

It is worth noting that optimal force distribution and zmp placement is only for DSP and is close to the solution in [56].

5.3.1 Optimal force distribution and ZMP placement

From (5.2), the whole-body ZMP commands both the resultant moment and resultant force applied onto the robot. The latter is written as follows:

$$\mathbf{F} = M(\ddot{\mathbf{P}}_{\text{COM}} - \vec{g}) = M \begin{bmatrix} \omega_c^2(x_{\text{COM}} - x_{\text{ZMP}}) \\ \omega_c^2(y_{\text{COM}} - y_{\text{ZMP}}) \\ g \end{bmatrix} \quad (5.12)$$

where M is the robot mass. From the ZMP definition, we have the relations:

$$\begin{cases} (x_{\text{ZMP}_R} - x_{\text{ZMP}})F_R^z + (x_{\text{ZMP}_L} - x_{\text{ZMP}})F_L^z = 0 \\ (y_{\text{ZMP}_R} - y_{\text{ZMP}})F_R^z + (y_{\text{ZMP}_L} - y_{\text{ZMP}})F_L^z = 0 \\ F_R^z + F_L^z = Mg \end{cases} \quad (5.13)$$

We split this resultant force into forces \mathbf{F}_i^c at each contact, and similarly the whole-body ZMP $\mathbf{P}_{\text{ZMP}}^c$ into ZMPs $\mathbf{P}_{\text{ZMP}_i}$ at each contact. This ZMP-force distribution problem being underdetermined from an optimization standpoint, one can select solutions based on a desired cost function. Following [56], we define this function as the minimization of ankle torques. The torques in foot i at the ankles \mathbf{P}_i are:

$$\begin{aligned}\Gamma(\mathbf{P}_i) &= \overrightarrow{\mathbf{P}_i \mathbf{P}_{\text{ZMP}_i}} \times \mathbf{F}_i \\ &= \begin{bmatrix} (y_{\text{ZMP}_i} - y_i)F_i^z - (z_{\text{ZMP}_i} - z_i)F_i^y \\ (z_{\text{ZMP}_i} - z_i)F_i^x - (x_{\text{ZMP}_i} - x_i)F_i^z \\ (x_{\text{ZMP}_i} - x_i)F_i^y - (y_{\text{ZMP}_i} - y_i)F_i^x \end{bmatrix} \\ &\equiv \begin{bmatrix} (y_{\text{ZMP}_i} - y_i)F_i^z \\ -(x_{\text{ZMP}_i} - x_i)F_i^z \\ 0 \end{bmatrix}\end{aligned}\quad (5.14)$$

the simplification comes from the assumption that:

$$\begin{aligned}(y_{\text{ZMP}_i} - y_i)F_i^z &\gg (z_{\text{ZMP}_i} - z_i)F_i^y \\ (x_{\text{ZMP}_i} - x_i)F_i^z &\gg (z_{\text{ZMP}_i} - z_i)F_i^x\end{aligned}\quad (5.15)$$

Thus we limit the optimization problem to a planar problem in the ZMP plane.

We choose to minimize ankle torques at the position \mathbf{P}_i , which yields the following optimization problem:

$$\begin{aligned}\min_{x_{\text{ZMP}_i}, y_{\text{ZMP}_i}, F_i^z} &\left(\sum_{i=R,L} \Gamma^T(\mathbf{P}_i) \Gamma(\mathbf{P}_i) \right) \\ &\sum_{i=R,L} x_{\text{ZMP}_i} F_i^z = x_{\text{ZMP}} M g \\ &\sum_{i=R,L} y_{\text{CoP}_i} F_i^z = y_{\text{ZMP}} M g \\ &\sum_{i=R,L} F_i^z = M g\end{aligned}\quad (5.16)$$

From which we can eliminate $x_{\text{ZMP}_R}, y_{\text{ZMP}_R}$ and F_R^z as variables and obtain:

$$\begin{aligned}\min_{x_{\text{ZMP}_L}, y_{\text{ZMP}_L}, F_L^z} &(\zeta) \\ &\sum_{i=R,L} F_i^z = M g\end{aligned}\quad (5.17)$$

with:

$$\zeta = \begin{pmatrix} ((y_{\text{ZMP}_L} - y_L)^2 + (x_{\text{ZMP}_L} - x_L)^2) F_L^z{}^2 \\ + ((y_{\text{ZMP}} - y_R) M g - (y_{\text{ZMP}_L} - y_R) F_L^z)^2 \\ + ((x_{\text{ZMP}} - x_R) M g - (x_{\text{ZMP}_L} - x_R) F_L^z)^2 \end{pmatrix}\quad (5.18)$$

From the gradient of ζ in equation (5.18), we look for critical points:

$$\frac{\partial \zeta}{\partial F_L^z} = 0, \frac{\partial \zeta}{\partial x_{ZMP_L}} = 0, \frac{\partial \zeta}{\partial y_{ZMP_L}} = 0 \quad (5.19)$$

with:

$$\begin{aligned} \frac{\partial \zeta}{\partial z_{F_L}} &= \begin{pmatrix} 2((y_{ZMP_L} - y_L)^2 + (x_{ZMP_L} - x_L)^2)z_{F_L} \\ -2((y_{ZMP} - y_R)Mg - (y_{ZMP_L} - y_R)z_{F_L})(y_{ZMP_L} - y_R) \\ -2((x_{ZMP} - x_R)Mg - (x_{ZMP_L} - x_R)z_{F_L})(x_{ZMP_L} - x_R) \end{pmatrix} \\ \frac{\partial \zeta}{\partial x_{ZMP_L}} &= \begin{pmatrix} 2(x_{ZMP_L} - x_L)z_{F_L}^2 \\ -2((x_{ZMP} - x_R)Mg - (x_{ZMP_L} - x_R)z_{F_L})z_{F_L} \end{pmatrix} \\ \frac{\partial \zeta}{\partial y_{ZMP_L}} &= \begin{pmatrix} 2(y_{ZMP_L} - y_L)z_{F_L}^2 \\ -2((y_{ZMP} - y_R)Mg - (y_{ZMP_L} - y_R)z_{F_L})z_{F_L} \end{pmatrix} \end{aligned} \quad (5.20)$$

From (5.19), we obtain the following system:

$$\begin{cases} x_{ZMP_L} - \frac{x_L + x_R}{2} = \frac{(x_{ZMP} - x_R)Mg}{2F_L^z} \\ y_{ZMP_L} - \frac{y_L + y_R}{2} = \frac{(y_{ZMP} - y_R)Mg}{2F_L^z} \\ F_L^z[(x_L - x_R)^2 + (y_L - y_R)^2] = -Mg \begin{pmatrix} x_{ZMP} - x_R)(x_R - x_L) \\ +(y_{ZMP} - y_R)(y_R - y_L) \end{pmatrix} \end{cases} \quad (5.21)$$

The combination of equations (5.17) and (5.21) yields an analytical solution with a purely geometric construction:

$$\begin{cases} F_L^z = Mg \frac{\|\mathbf{P}_R \mathbf{P}_{ZMP}^o\|}{\|\mathbf{P}_R \mathbf{P}_L\|} \\ \overrightarrow{\mathbf{NP}}_{ZMP_L} = \overrightarrow{\mathbf{P}_R \mathbf{P}_{ZMP}} \times \frac{\|\mathbf{P}_R \mathbf{N}\|}{\|\mathbf{P}_R \mathbf{P}_{ZMP}^o\|} \\ \overrightarrow{\mathbf{NP}}_{ZMP_R} = \overrightarrow{\mathbf{P}_L \mathbf{P}_{ZMP}} \times \frac{\|\mathbf{P}_L \mathbf{N}\|}{\|\mathbf{P}_R \mathbf{P}_{ZMP}^o\|} \\ F_R^z = Mg - F_L^z \end{cases} \quad (5.22)$$

where \mathbf{P}_{ZMP}^o is the orthogonal projection of \mathbf{P}_{ZMP} on the line $(\mathbf{P}_R \mathbf{P}_L)$, \mathbf{N} is the middle of the segment $[\mathbf{P}_R \mathbf{P}_L]$ and F_i^z is the vertical component of \mathbf{F}_i . Fig. 5.4 shows the graphical representation of these equations. We define (L) and (R) as the perpendiculars of $[\mathbf{P}_L \mathbf{P}_R]$ from \mathbf{P}_L to \mathbf{P}_R .

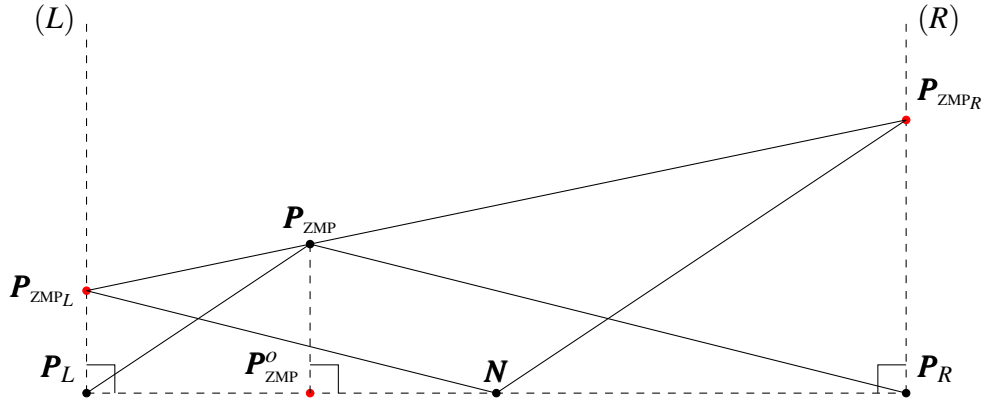


Figure 5.4 Graphical description of the optimal \mathbf{P}_{ZMPL} and \mathbf{P}_{ZMPR} in DSP from (5.22).

From (5.22), we can define the force distribution d_L in foot L and by extension the force distribution d_R in foot R as:

$$\begin{aligned} d_L &= \frac{F_L^z}{Mg} \\ d_R &= 1 - d_L \end{aligned} \quad (5.23)$$

When \mathbf{P}_{ZMP} is inside the area between lines (L) and (R) , we obtain $1 > d_L > 0$ which implies a pure DSP case with the force distributed under each foot.

When \mathbf{P}_{ZMP} is outside the area between lines (L) and (R) , we obtain $d_L > 1$ or $d_L < 0$ which implies that the GRF under one foot is over Mg and lower than 0 under the other. Because the feet cannot be pulled by the floor, a negative vertical GRF is impossible to obtain (the foot get off the floor). This implies a saturation of $d_i \in [0, 1]$. From (5.23), when the force distribution under one foot is equal to 1 the other is 0 which yields a GRF that no longer exist. Therefore, we are equivalent to a SSP case on the foot with the force distribution at 1. During such SSP case, the GRF is fully considered under the support foot for the admittance control.

5.3.2 Satisfaction of ZMP constraints

The non-tilting condition for feet contacts is characterized by the *ZMP support area*. This area is state-varying in general [57], notably when friction is limited. However, in our setting (cart-table model and larger friction over uneven ground thanks to sole compliance) we can safely approximate it by the convex hull of ground contact points [28].

When compensation terms in the COM-ZMP control law are too high, the whole-body control ZMP \mathbf{P}_{ZMP}^c will lie outside this convex hull. In such cases and to ensure the maximum dynamic control of the inverse pendulum model, we project \mathbf{P}_{ZMP}^c back to the point \mathbf{P}_{ZMP}^s closest to it on the edge of the ZMP support area.

During single support phases (SSP), \mathbf{P}_{ZMP}^c is projected at the closest point on the foot shape in contact with the ground. Examples of projection in these phases are shown in Fig. 5.5.

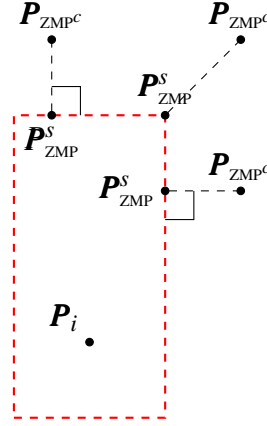


Figure 5.5 Examples of control ZMP \mathbf{P}_{ZMP}^c projected at the point \mathbf{P}_{ZMP}^s on the edge of the ZMP support area equivalent to the foot shape in contact with the ground (dashed red) in SSP.

In DSP, the classical convex hull is defined by the feet and the space in between. Fig. 5.6 shows this convex hull. However, following our choice to minimize ankle torques during ZMP-force distribution, \mathbf{P}_{ZMP_L} and \mathbf{P}_{ZMP_R} during double support phases (DSP) are defined on the lines (L) and (R). They also must be inside their respective foot polygon. Those constraints delimit the existence of \mathbf{P}_{ZMP_i} into the segment $[\mathbf{P}_i^1 \mathbf{P}_i^2]$ where \mathbf{P}_i^1 and \mathbf{P}_i^2 are the intersections of line (i) with the foot shape i . The ZMP definition induces the equation system (5.13) which constrain the alignment of \mathbf{P}_{ZMP} , \mathbf{P}_{ZMP_L} and \mathbf{P}_{ZMP_R} . Hence, a reduced convex hull can be defined during DSP to constraint \mathbf{P}_{ZMP}^c . The latter is defined by the convex polygon delimited by $(\mathbf{P}_R^1 \mathbf{P}_R^2 \mathbf{P}_L^2 \mathbf{P}_L^1)$, as depicted in Figure 5.6.

In the event where \mathbf{P}_{ZMP}^c lies between (L) and (R) during DSP, we project it at the closest point on the reduced convex hull to keep the maximum dynamic on the COM. For \mathbf{P}_{ZMP}^c outside (L) and (R) during DSP, we use the same projection as in a SSP case.

5.3.3 ZMP projection to CoP

In Chapter 4, we assume to walk on a flat plane. Hence, the parameter used in the DE to predict the sole deformation is the ZMP $_i$ in the contact plane equivalent to the CoP $_i$. On a flat horizontal plane, the contact plane of each foot is confound with the ZMP plane. When the contact plane of the foot is not confound with the ZMP plane, the ZMP $_i$ is the projection of CoP $_i$ in that plane along the direction of \mathbf{F}_i .

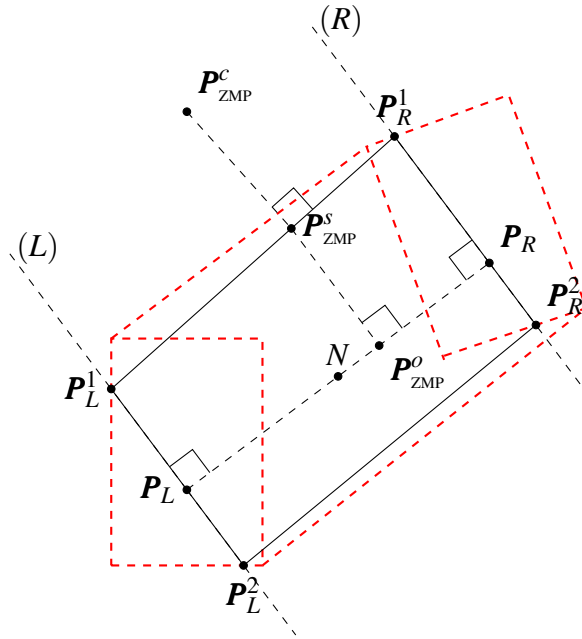


Figure 5.6 Convex hull of ground contact points (dashed red) and reduced ZMP support area (black) in double support phases (DSP) when ZMP-force distribution minimizes ankle torques. The control ZMP \mathbf{P}_{ZMP}^c is projected to \mathbf{P}_{ZMP}^s .

From the equation (5.23), we chose $\mathbf{F}_i = d_i \mathbf{F}$ which imply that the CoP_i is projected as ZMP_i in any plane along the direction of the GRF. Figure 5.7 shows an example of CoP_i projection. Conversely, such projection allows to obtain the CoP_i from a known ZMP_i . Such CoP_i is then used in the admittance control of the foot in Section 5.4.

5.4 Floor reaction force control layer

For humanoid robots that are controlled in position, force distribution control at the feet is realized by admittance control [51]. The output from an admittance controller consists of foot orientations and relative positions, whereas its input is given by the resultant forces and CoP s computed by the ZMP-force distributor. Let us define:

$$\delta_i = \begin{bmatrix} \mathbf{P}_i \\ \Theta_i \end{bmatrix}, \quad \mu_i = \begin{bmatrix} \mathbf{F}_i \\ x_{\text{CoP}_i} \\ y_{\text{CoP}_i} \\ \Gamma_{\text{CoP}_i}^z \end{bmatrix} \quad (5.24)$$

where Θ_i is the orientation vector of the foot i with respect to the ground frame.

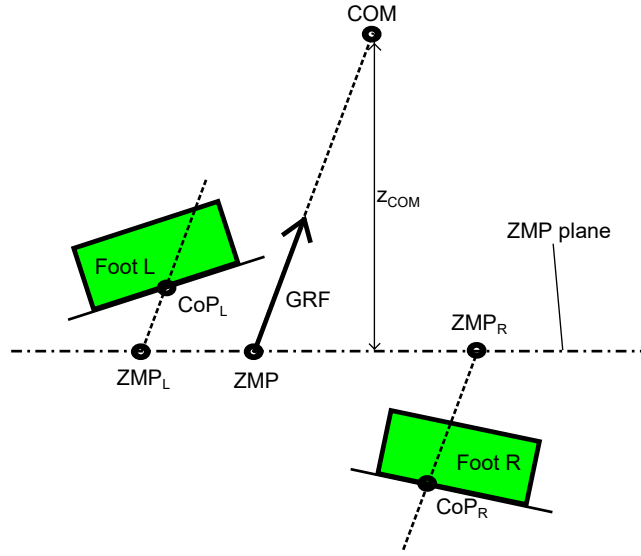


Figure 5.7 Example of CoP projection on ZMP plane.

Our model of the sole stiffness is given by:

$$\dot{\boldsymbol{\mu}}_i = \mathbf{K}_i(\boldsymbol{\mu}_i) \boldsymbol{\delta}_i \quad (5.25)$$

where the stiffness matrix $\mathbf{K}_i(\boldsymbol{\mu}_i)$ is obtained by linearization of a finite element model (FEM) of the soft sole at $\boldsymbol{\mu}_i$, as detailed in Chapter 4. Based on algorithm of the deformation estimator in Section 4.2.4, equation (5.25) is a nonlinear model of the sole contact state. Such method to obtain $\mathbf{K}_i(\boldsymbol{\mu}_i)$ is too slow to perform online admittance control. In order to solve this constraint online, we approximate $\mathbf{K}_i(\boldsymbol{\mu}_i)$ around a nominal $\boldsymbol{\mu}_i^0$ state. $\boldsymbol{\mu}_i^0$ is chosen at the static state where CoP_i is at the vertical of the foot ankle and where:

$$\begin{aligned} \mathbf{F}_i^0 &= \begin{bmatrix} 0 \\ 0 \\ \frac{Mg}{2} \end{bmatrix} \\ \Gamma_{\text{CoP}_i}^{z0} &= 0 \end{aligned} \quad (5.26)$$

However, we noticed in experiments that the rotational stiffness highly depends on the vertical force F_i^z . We chose to take into account this dependence with the following model:

$$\mathbf{K}_i(F_i^z) = \mathbf{K}_i(\boldsymbol{\mu}_i^0) \begin{bmatrix} \mathbf{I} & (0) \\ (0) & k_f(F_i^z)\mathbf{I} \end{bmatrix} \quad (5.27)$$

with $k_f(F_i^z) = F_i^z/F_i^{z0}$ and \mathbf{I} the identity matrix.

Feedback control of such system is equivalent to a damping:

$$\dot{\boldsymbol{\delta}}_i = \mathbf{D}_i^{-1}(\boldsymbol{\mu}_i^c - \boldsymbol{\mu}_i) \quad (5.28)$$

We thus obtain the transfer function of the following closed-loop error $\boldsymbol{\epsilon}_i = \boldsymbol{\mu}_i - \boldsymbol{\mu}_i^\infty$:

$$\dot{\boldsymbol{\epsilon}}_i = -\mathbf{K}_i(F_i^z)\mathbf{D}_i^{-1}\boldsymbol{\epsilon}_i \quad (5.29)$$

with $\lim_{t \rightarrow +\infty} \boldsymbol{\mu}_i = \boldsymbol{\mu}_i^\infty$. We choose the poles as $\lambda_a \mathbf{I}$, so that $\mathbf{D}_i^{-1} = \lambda_a \mathbf{K}_i(F_i^z)^{-1}$.

From the integration of (5.28), we obtain the admittance control:

$$\boldsymbol{\delta}_i^c = \boldsymbol{\delta}_i + dt \lambda_a \mathbf{K}_i(F_i^z)^{-1} \Delta \boldsymbol{\mu}_i \quad (5.30)$$

where dt is the discrete time-step duration and $\Delta \boldsymbol{\mu}_i = \boldsymbol{\mu}_i^c - \boldsymbol{\mu}_i$. This controller couple the force and torques (from the CoP) with tuned gains from the simplified FEM of the soft soles. This implies that only one gain λ_a need to be tuned. Figure 5.8 shows the block diagram of the resulting admittance controller.

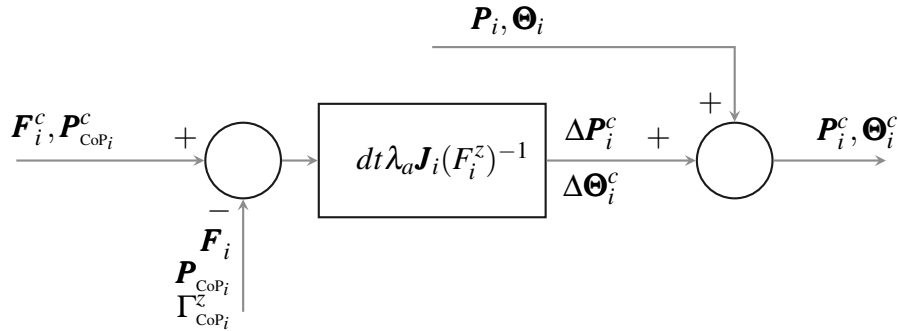


Figure 5.8 *Reaction force controller*: the ZMP $\mathbf{P}_{\text{ZMP}_i}^c$ and contact force \mathbf{F}_i^c under the foot i are compared to the robot state $\mathbf{P}_{\text{ZMP}}^c$ and \mathbf{F}_i^c in order to control in admittance the robot by generating foot i relative position \mathbf{P}_i^c and orientation Θ_i^c control.

Note that, during SSP where the foot i is not in contact with the ground, it is not controlled by the floor reaction force controller directly. Rather, Θ_i is defined to put the foot i horizontal and \mathbf{P}_i is the interpolated trajectory of the ankle in the air to move the foot to the next planed foot-step.

5.5 Experiments

5.5.1 Experimental setup

We perform walking experiments with the HRP-4 humanoid robot wearing the same custom feet (Figure 5.9) as in Chapter 4 to validate the deformation estimator (in Section 4.3). These soles come as a replacement of the ankle shock absorbing system (hence the ankle leg link is rigid). The soles are made of a flexible foam. Combining the results of compression test and FEM simulation, we estimated their Young's modulus as $E = 0.32$ MPa and Poisson ratio as $\nu = 0.31$.



Figure 5.9 (a): new HRP-4's feet; (b): photo of HRP-4's feet with soft soles

Experiments consist in a straightforward walk of 4 footsteps on a distance of 20 cm with an average velocity of 1.1 cm/s. An anti-windup is used to limit the error integration by defining a sliding integration windows of 400 ms. The SSP and DSP durations given to the WPG are respectively set at 1 s and 2 s. No ground information is given preliminary for walking, *i.e.* the whole experiment is *terrain-blind*.

The poles of the ZMP-COM tracking controller are set to $(-4, -4, -3, -\omega_c)$ while $T_p = 0.11$ s and $\omega_c = 3.54$ s⁻¹. In order to minimize robot vibrations, k_f is saturated between $[0.5 - 1.5]$ during DSP and at 0.9 during SSP. HRP-4's low-level control frequency being 200 Hz, we choose $\lambda_a = -200$ Hz. The nominal μ_i^0 states are set to $\mathbf{F}_i^0 = [0 \ 0 \ \frac{Mg}{2}]^T$, $\mathbf{P}_{\text{CoP}_i}^0 = \mathbf{P}_i$ and $\Gamma^{\text{z0}}_{\text{CoP}_i} = 0$.

5.5.2 Robot feedback state estimator

We developed a simple robot feedback state estimator based on joint position measurement (for geometry-based reconstruction), F/T sensors measures and an estimate of the pelvis

orientation frame provided by the robot software and IMU measurements. We define the robot measurement as from the real robot and the reference trajectory as from the QP robot.

The estimate of the pelvis orientation frame provided by the robot software and IMU measurements gives the real robot orientation in the world frame. With the assumption that the vertical axis is well measured, a simple rotation around this axis is used to obtain the robot orientation error along x and y -axis into the QP frame.

Despite recommendation from Carpentier *et al.* [58], we used only the geometry-based reconstruction to estimate the COM and deduce the ankle position of the real robot. Then we make the assumption that the feet in contact with the floor doesn't move much from the reference. In the ZMP-COM controller (5.5), all positions can be expressed relatively to the reference ankle position and thus avoid integration drift from the IMU acceleration measurement. For the same reason, we estimate the COM velocity by finite differentiation of the distance between the feet in contact with the floor and the COM. Hence, we are only subject to position sensors noise.

The COM height is supposed constant and all desired and control references of ZMP are generated with this assumption. Hence, in order to keep the same linear inverse pendulum model (LIPM) as in section 5.2, all ZMPs measured are computed into an horizontal plane at the same vertical distance from the measured COM than in the LIPM.

This simple observer results in little mismatch between measures and actual COM location: in static equilibrium, projected COM and ZMP locations differ by roughly 2 cm. Nonetheless, our closed-loop controller recovers from this static error and achieves walking with soft soles.

5.5.3 Walking on flat floor and gravel

Without a deformation estimator, HRP-4 was unable to walk on gravel without and with soft soles. With an offline deformation estimator, the robot manages to walk on flat floor but not on gravel. Furthermore, it then deals with a very limited range of perturbations/uncertainties.

With our closed-loop controller, the robot succeeded in walking on flat floor and on a bed of gravel with a granularity of 10/20 mm. Figures 5.10 to 5.12 show measurements for walking on flat floor and over gravel.

Figure 5.10 represents the ZMP and COM in the direction of x - and y -axes controlled by the ZMP-COM control layer during walking on flat floor and gravel. Due to the motion dynamics chosen for the experiments, ZMP and COM references are close to each other and are hard to visually differentiate. The ZMP also remains within the support area. Some oscillations on the COM, and by extension the ZMP that controls it, are visible. By comparing the measure on flat floor and gravel, an increase in amplitude on ZMP-COM oscillations is

observable on the later. They are mostly due to gravel irregularities and abrupt changes in contact surface during landing phases. The action of the ZMP control P_{ZMP}^C is clearly visible in the controlled movement of ZMP in order to keep the COM close to its reference.

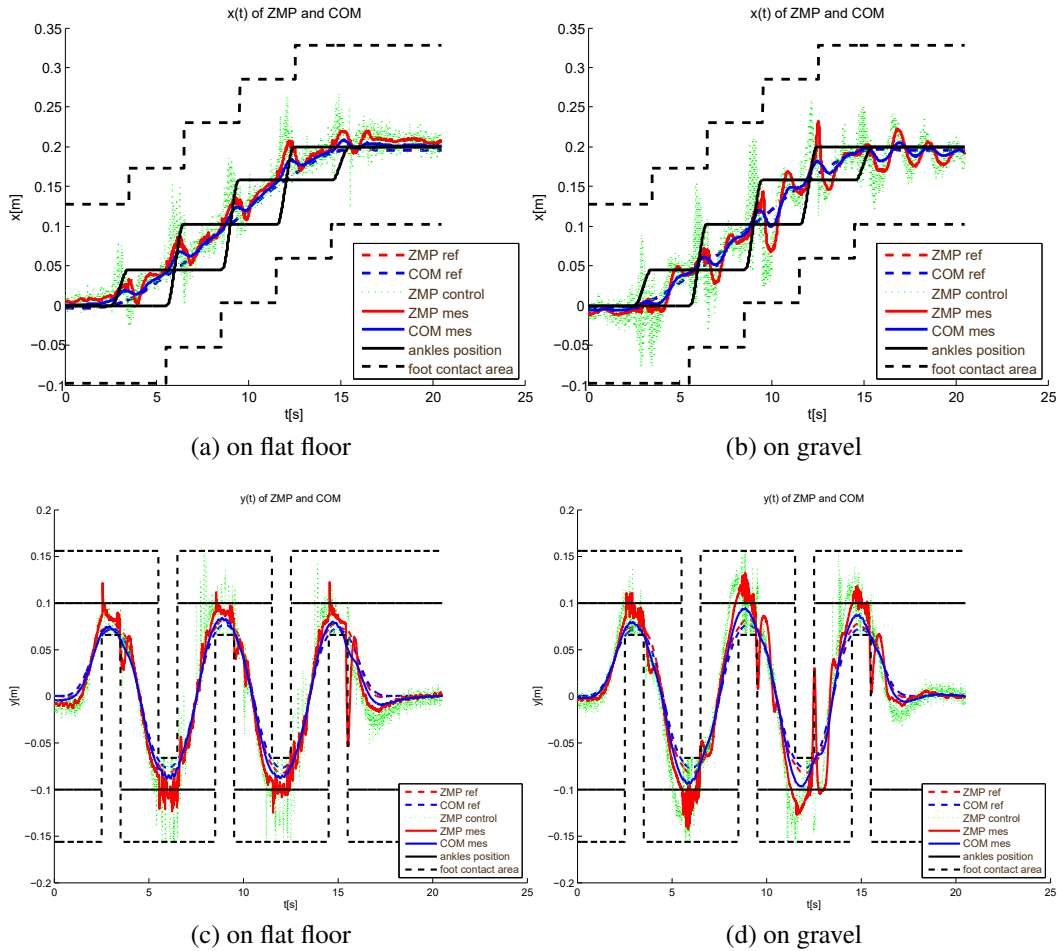


Figure 5.10 *Walking over flat floor and gravel (granulometry: 10/20 mm): ZMP and COM measured compared with the references along x/y axes during a four steps and 20cm long walk.*

Figure 5.11 represents the vertical ground reaction forces (GRF) controlled by the admittance of the reaction force controller. The measure corresponds to the control with irregularities during transition between DSP and SSP when one foot takes off and lands on the floor. Some impacts are visible at landing and are quickly absorbed by the sole and the admittance controller. Due to gravel irregularities and movements under the feet, higher impact are visible during landing phases in comparison with the walking on flat floor. These

observations show the action of our deformation estimator model and floor reaction force controller.

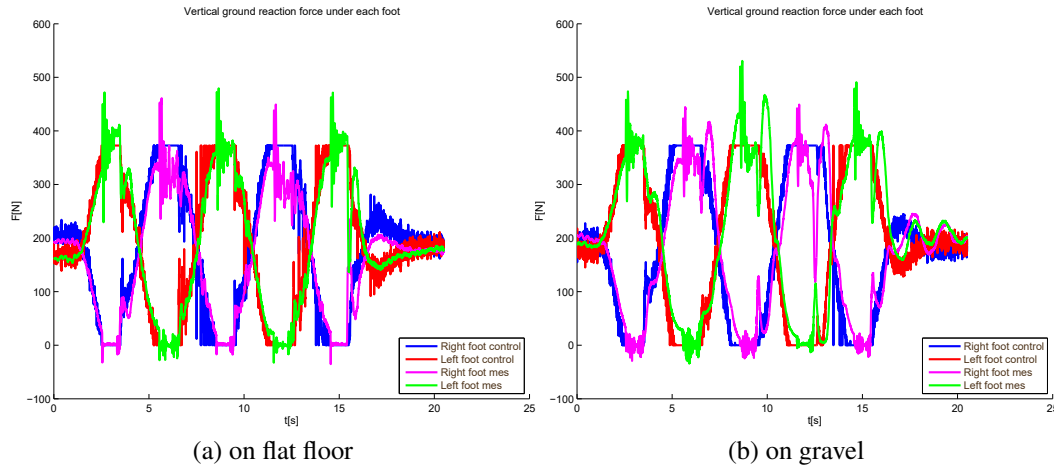


Figure 5.11 *Walking over flat floor and gravel (granulometry: 10/20 mm)*: Vertical ground reaction forces under each foot measured compared with the references along x/y axes during a four steps and 20cm long walk.

Figure 5.12 represents the CoP under each foot, both controlled by the floor reaction control layer. Same as in Figure 5.10, ZMP and COM references are hard to visually differentiate due to the motion dynamics chosen for the experiments. Overall, measurements track well the references. As for the GRF, peaks of ZMP and CoP under the left foot appear due to an early landing foot.

Oscillations in CoP and ZMP controls result from a combination of (1) gravel irregularities and (2) significant noise in COM velocity (see Fig. 5.13) estimation coupled with ZMP-COM controller gains. This noise is well distributed and with the mechanical lag, these vibrations are absorbed and have low impact on the actual measured ZMP.

The accompanying video³ shows experiments on the real robot: eight steps walking fully on gravel, as well as with a transition from wooden plank ground to gravel (Figure 5.1).

5.6 Conclusion

In this chapter, we designed a closed-loop controller based on linear inverted pendulum tracking and an admittance control of ground reaction forces combined with a simple deformation estimator. We achieved walking with HRP-4 on flat and gravel grounds.

Robot stabilization depends on the identification of the mechanical lag time constant T_p of ZMP response and the adaptation of the WPG to this time constant to choose the phase duration. Up to now, the WPG used for our experiments generates motion trajectories offline. We then plan to improve biped locomotion by using an adaptive online WPG (in terms of foot impact detection) coupled with a more precise estimation of the lags time constant and to change the phase durations in order to better stabilize the robot when the ground properties are changing. It would be interesting to test walking on other irregular terrains and larger steps.

In the same way, the robot stabilization depends on the stiffness matrix \mathbf{J} . In our model, it only depend on the soft soles properties but we can extend this stiffness matrix to include the ground properties (if walking on deformable floor). It would also be interesting to develop a method to estimate online \mathbf{J} to adapt the walk to unknown ground properties.

In addition, the robot stabilization depends on the precision of the robot state estimator. Developing a better one would help the controller actions to correct the robot motion.

Finally, the WPG is offline and inhibit the controller reactivity to perturbations like timing errors of foot landing. An adaptation of the WPG would help the robot stabilization.

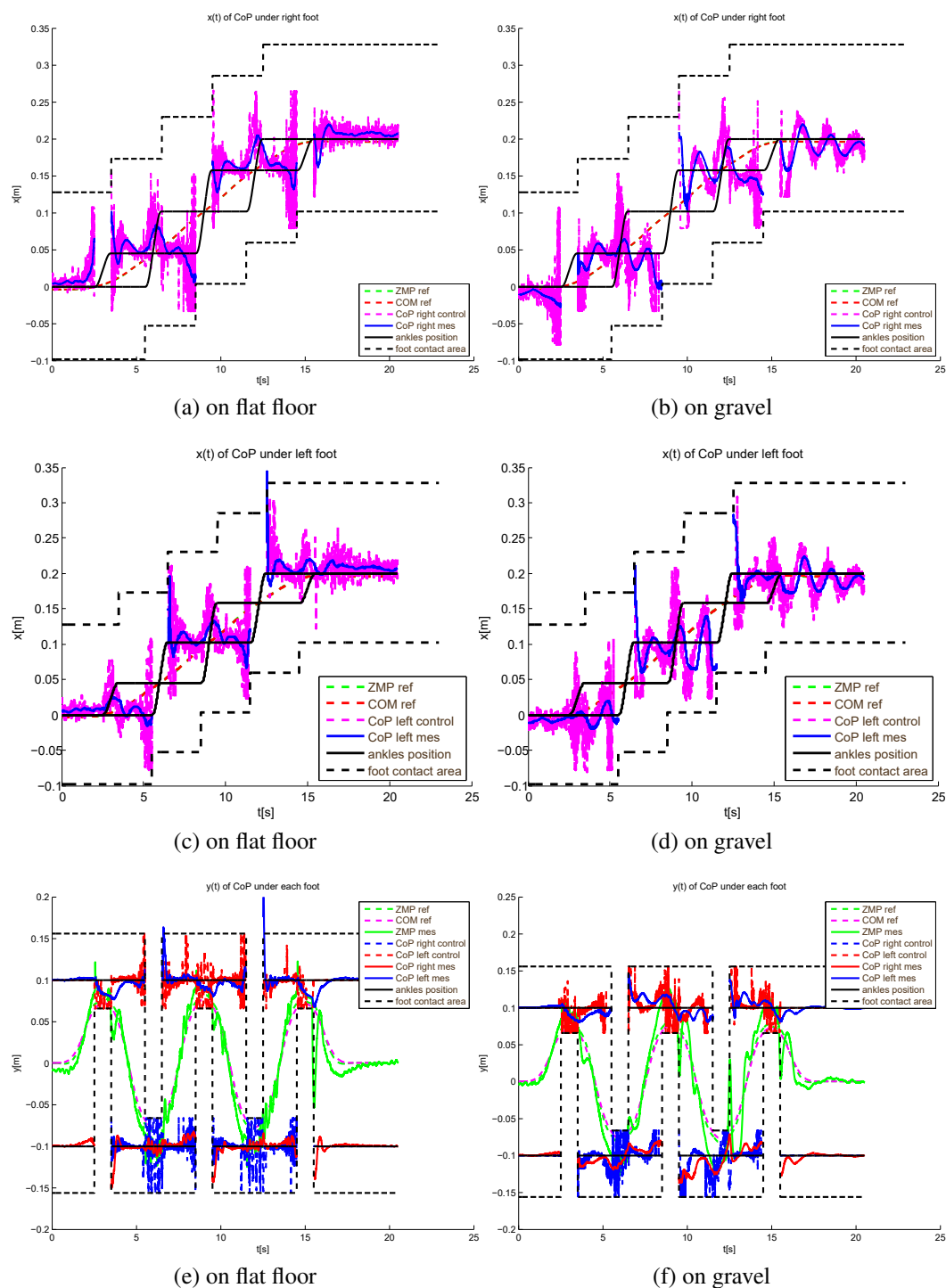


Figure 5.12 Walking over flat floor and gravel (granulometry: 10/20 mm): CoP under each foot measured compared with the references along x/y axes during a four steps and 20cm long walk.

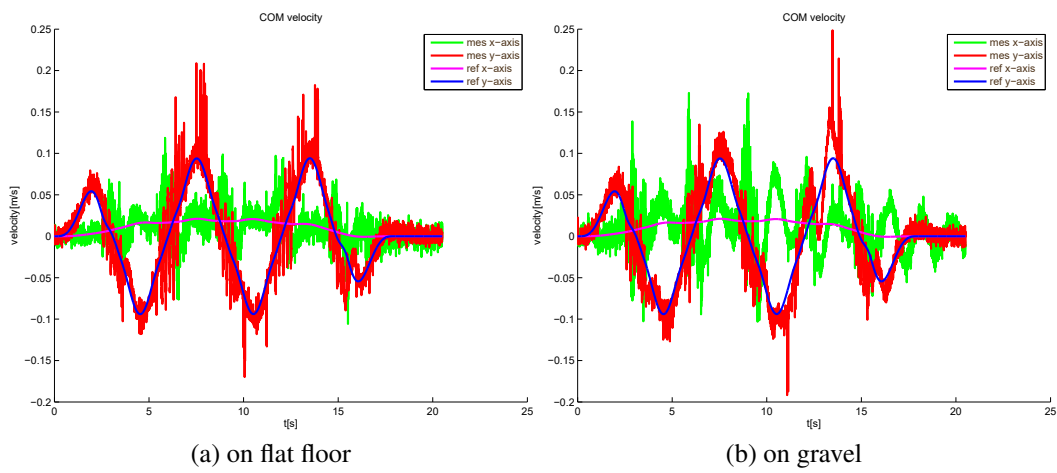


Figure 5.13 *Walking over flat floor and gravel (granulometry: 10/20 mm): COM velocity measured compared with the references along x/y axes during a four steps and 20cm long walk.*

Chapter 6

Conclusion

In this thesis, we investigated adding soft soles under humanoid robots feet. The goal of using such soles is to :

- increase the foot possible movement in contact with the ground
- protect the robot from foot landing impact
- shape the environment to deal with ground unevenness and irregularities during walking.

However, the passive degrees of freedom induced by such soles generate instabilities that have to be taken into account in the walking motion. Inspired by human balance strategy, we addressed this problem by developing a closed-loop controller based on a simple deformation estimator that compensate the sole deformation to stabilize the walking motion generated by a dedicated walking pattern generator. We tested our approach on a humanoid robot HRP-4 walking on gravel, as depicted in Figure 5.1.

In Chapter 2, we looked at the possible strategies that people adopt when unexpectedly stepping onto a soft surface to preserve dynamic stability and avoid loss of balance. We pointed that during walking, humans modulate the ground reaction forces (GRF) and the center of pressure (CoP) under the feet when a surface transition from hard ground to soft ground occurs. We are aware that the current analysis has some limitations and additional analysis are needed to understand better all the mechanics of walking on soft floor. First of all, only the transition step has been analyzed. It would be interesting to also analyze the step anticipating and the one following the transition. These analysis could allow us to validate the main hypothesis that the results of this study suggest, that is that participants exploited the compliant properties of the soft surface to dissipate mechanical energy. However, the control balance strategy on soft floor of human can be seen close to the walk on mattress

(with a lower deformation coefficient). Hence, we chose to adapt and extend those results to bipedal humanoid robot walking.

In Chapter 3, we developed a walking pattern generator (WPG) adapted for soft soles based on the minimization of simplified energy consumption. Inspired by the observation of human walking on soft floor, our WPG generates robot motion and manages zero moment point (ZMP) equivalent to CoP under each foot during the double support phase (DSP) and the force distribution. Experiments on HRP-2 showed that the built-in shock-absorbing mechanism induces relatively high torques. Replacing these *springs* by soft soles reduce torques in ankle and provide an alternative to each ankle shock-absorbing mechanism to protect the robot structure. A comparison between different choice of optimization criteria weights, revealed the effects of ZMP and COM trajectories on the walking motion and impacts on the robots. Indeed, by choosing the weights of the optimization criterion, it was possible to change the walking behaviors (see video¹). Based on the observations in Chapter 2, human deal with floor stiffness property during walking. Our WPG formulation is useful in order to modulate the GRF and CoP with a quasi-static sole deformation model to balance and control the humanoid robots.

In Chapter 4, we developed a deformation estimator (DE) that predict the sole deformation and compute the foot movement to satisfy the ZMP generated by the WPG. Experiments on the HRP-4 robot showed that using jointly our WPG and DE allow to walk with soft soles (see video²). However, due to slow computational time, such method does not allow the robot reactivity and to deal with perturbations and correct errors on trajectory which can both induce instabilities. Hence, an online method is needed to well control the robot walk, as proposed in the next chapter.

In Chapter 5, we developed a closed-loop controller based on linear inverted pendulum tracking and an admittance control of ground reaction forces combined with a simple deformation estimator. We successfully managed HRP-4 to walk on flat and gravel grounds wearing thick soft soles (see video³). However, the robot stabilization highly depends on the identification of mechanical lag and stiffness of the admittance control. Hence, it would be interesting to develop a method to estimate those parameters online to better adapt the walk to unknown ground properties. In addition, the robot stabilization depends on the precision of the robot state estimator. Developing a better one would help the controller actions to correct the robot motion. Finally, the WPG is offline and inhibit the controller reactivity to perturbations like timing errors of foot landing. An adaptation of the WPG would also help the robot stabilization.

In conclusion, we proved the possibility for humanoid robot to walk wearing soft soles on gravel which is an uneven, irregular and deformable ground. Programming efforts have

been done to develop a new control framework for the real robot HRP-4 to walk with soft soles. We learned a lot about stabilization on soft material.

Scientific perspective

In terms of scientific perspective, we want in a short schedule develop the robot stabilization with different walking situations. Notably, in the context of the COMANOID project, we will adapt our developpements to the walk in an industrial area of aviation. The robot will encounter wires, screws and any material that can be found in such place and we hope to deal with them like with gravel.

In a mid-term scientific perspective, we have to improve the tools around the closed-loop controller for a better stabilization. Notably the robot state-estimator which is a crucial part of the tracking error control and which would be useful in a general matter to use HRP-4. In addition, we will improve the WPG to generate online motion and notably detect contact landing to adapt the walking motion.

In a long-term scientific perspective, it would be useful to develop a method to identify online the ground deformation properties. That would improve the stabilization control of the humanoid robot when the ground properties are changing. In addition, incorporating the closed-loop in the QP controller would improve the robot control.

Notes

¹Video of HRP-2 walking with different walking behavior : <https://youtu.be/42J3bevFDPc>

²Video of HRP-4 walking with soft soles : <https://youtu.be/o0Ou82tTqMQ>

³Video of HRP-4 walking in closed-loop with soft soles on flat floor and gravel : <https://youtu.be/CHa5RZn2ON8>

Bibliography

- [1] Yoshihiro Ehara and Sumiko Yamamoto. Introduction to body-dynamics-analysis of gait and gait initiation, 2002.
- [2] Kensuke Harada, Kanako Miura, Mitsuharu Morisawa, Kenji Kaneko, Shin'ichiro Nakaoka, Fumio Kanehiro, Tokuo Tsuji, and Shuuji Kajita. Toward human-like walking pattern generator. In *IEEE/RSJ International Conference on Intelligent Robots and Systems*, pages 1071–1077, St. Louis, USA, October 11 - 15 2009.
- [3] David A Winter. Human balance and posture control during standing and walking. *Gait & posture*, 3(4):193–214, 1995.
- [4] Daniel S Marigold and Aftab E Patla. Strategies for dynamic stability during locomotion on a slippery surface: effects of prior experience and knowledge. *Journal of Neurophysiology*, 88(1):339–353, 2002.
- [5] Janice J Eng, David A Winter, and Aftab E Patla. Strategies for recovery from a trip in early and late swing during human walking. *Experimental Brain Research*, 102(2):339–349, 1994.
- [6] AM Schillings, BMH Van Wezel, TH Mulder, and Jaak Duysens. Muscular responses and movement strategies during stumbling over obstacles. *Journal of Neurophysiology*, 83(4):2093–2102, 2000.
- [7] Jaap H van Dieën, Marcel Spanjaard, Reinier Konemann, Lennart Bron, and Mirjam Pijnappels. Balance control in stepping down expected and unexpected level changes. *Journal of biomechanics*, 40(16):3641–3649, 2007.
- [8] Masahiro Shinya, Shinya Fujii, and Shingo Oda. Corrective postural responses evoked by completely unexpected loss of ground support during human walking. *Gait & posture*, 29(3):483–487, 2009.
- [9] Roy Müller, Kevin Tschiesche, and Reinhard Blickhan. Kinetic and kinematic adjustments during perturbed walking across visible and camouflaged drops in ground level. *Journal of biomechanics*, 47(10):2286–2291, 2014.
- [10] Daniel P Ferris, Kailine Liang, and Claire T Farley. Runners adjust leg stiffness for their first step on a new running surface. *Journal of biomechanics*, 32(8):787–794, 1999.
- [11] Daniel S Marigold and Aftab E Patla. Adapting locomotion to different surface compliances: neuromuscular responses and changes in movement dynamics. *Journal of neurophysiology*, 94(3):1733–1750, 2005.

- [12] Michael J MacLellan and Aftab E Patla. Adaptations of walking pattern on a compliant surface to regulate dynamic stability. *Experimental brain research*, 173(3):521–530, 2006.
- [13] Peter H Veltink, Christian Liedtke, Ed Droog, and Herman van der Kooij. Ambulatory measurement of ground reaction forces. *Neural Systems and Rehabilitation Engineering, IEEE Transactions on*, 13(3):423–427, 2005.
- [14] H Martin Schepers, HFJM Koopman, and Peter H Veltink. Ambulatory assessment of ankle and foot dynamics. *Biomedical Engineering, IEEE Transactions on*, 54(5):895–902, 2007.
- [15] Johnny Nilsson and Alf Thorstensson. Ground reaction forces at different speeds of human walking and running. *Acta Physiologica Scandinavica*, 136(2):217–227, 1989.
- [16] Adrien Pajon, Giovanni De Magistris, Sylvain Miossec, Kenji Kaneko, and Abderrahmane Kheddar. A humanoid walking pattern generator for sole design optimization. In *International Conference on Advanced Robotics (ICAR)*, Istanbul, Turkey, 2015.
- [17] Giovanni De Magistris, Adrien Pajon, Sylvain Miossec, and Abderrahmane Kheddar. Optimized humanoid walking with soft soles. *Robotics and Autonomous Systems*, 95:52–63, 2017.
- [18] Pierre-Brice Wieber, Scott Kuindersma, and Russ Tedrake. Modeling and control of legged robots. In Bruno Siciliano and Oussama Khatib, editors, *Springer Handbook of Robotics*. Springer Berlin Heidelberg, 2nd edition, 2015.
- [19] Antoine Bussy, Abderrahmane Kheddar, André Crosnier, and François Keith. Human-humanoid haptic joint object transportation case study. In *IEEE/RSJ International Conference on Intelligent Robots and Systems*, pages 3633–3638, Vilamoura, Portugal, 7-12 October 2012.
- [20] Kanako Miura, Mitsuhara Morisawa, Shin’ichiro Nakaoka, Fumio Kanehiro, Kensuke Harada, Kenji Kaneko, and Shuuji Kajita. Robot motion remix based on motion capture data –towards human-like locomotion of humanoid robots–. In *IEEE/RAS International conference on Humanoid Robots*, pages 596–603, Paris, France, December 7-10 2009.
- [21] Katja Mombaur, Anh Truong, and Jean-Paul Laumond. From human to humanoid locomotion– an inverse optimal control approach. *Autonomous Robot*, 28:369–383, 2010.
- [22] Martin L. Felis, Katja Mombaur, Hideki Kadone, and Alain Berthoz. Modeling and identification of emotional aspects of locomotion. *Journal of Computational Science*, 4:255–261, 2013.
- [23] P.G. Adamczyk, S.H. Collins, and A.D. Kuo. The advantages of a rolling foot in human walking. *The Journal of Experimental Biology*, 209 (Pt 20):3953–3963, october 2006.
- [24] Seiichi Miyakoshi and Gordon Cheng. Examining human walking characteristics with a telescopic compass-like biped walker model. In *IEEE International Conference on Systems, Man and Cybernetics*, pages 1538–1543, 2004.

- [25] Shuuji Kajita, Hirohisa Hirukawa, Kensuke Harada, and Kazuhito Yokoi. *Humanoid Robot*. Ohmsha, Ltd, 2005.
- [26] Miomir Vukobratovic and Davor Juricic. Contribution to the synthesis of biped gait. *IEEE Transactions on Bio-Medical Engineering*, BME-16(1), January 1969.
- [27] Miomir Vukobratovic and Branislav Borovac. Zero-moment point-thirty five years of its life. *International Journal of Humanoid Robotics*, 1(1):157–173, January 2004.
- [28] Shuuji Kajita and Bernard Espiau. *Handbook of Robotics*, chapter Legged Robots, pages 361–389. Springer-Verlag, 2008.
- [29] Andrei Herdt, Holger Diedam, Pierre-Brice Wieber, Dimitar Dimitrov, Katja Mombaur, and Moritz Diehl. Online walking motion generation with automatic foot step placement. *Advanced Robotics*, 24(5-6):719–737, 2010.
- [30] Hyeok-Ki Shin and Byung Kook Kim. Energy-efficient gait planning and control for biped robots utilizing the allowable zmp region. *Robotics, IEEE Transactions on*, 30(4):986–993, August 2014.
- [31] Marko B. Popovic, Ambarish Goswami, and Hugh Herr. Ground reference points in legged locomotion : definitions, biological trajectories and control implications. *International Journal of Robotics Research*, 24(12):1013–1032, December 2005.
- [32] Pierre-Brice Wieber. On the stability of walking systems. In *Proceedings of the international workshop on humanoid and human friendly robotics*, 2002.
- [33] Kensuke Harada, Shuuji Kajita, Kenji Kaneko, and Hirohisa Hirukawa. An analytical method on real-time gait planning for a humanoid robot. *International Journal of Humanoid Robotics*, october 8 2004.
- [34] Mitsuhashi Morisawa, Kensuke Harada, Shuuji Kajita, Kenji Kaneko, Fumio Kanehiro, Kiyoshi Fujiwara, Shinichiro Nakaoka, and Hirohisa Hirukawa. A biped pattern generation allowing immediate modification of foot placement in real-time. In *IEEE-RAS International Conference on Humanoid Robots*, pages 581 – 586, 2006.
- [35] Pierre-Brice Wieber. Trajectory free linear model predictive control for stable walking in the presence of strong perturbations. In *IEEE-RAS International Conference on Humanoid Robots*, pages 137 – 142, 2006.
- [36] Christopher L Vaughan, Brian L Davis, and Jeremy C O’Connor. *Dynamics of human gait*. Kiboho, 1992.
- [37] Giovanni De Magistris, Adrien Pajon, Sylvain Miossec, and Abderrahmane Kheddar. Humanoid walking with compliant soles using a deformation estimator. In *International Conference on Robotics and Automation (ICRA)*, Stockholm, Sweden, 2016.
- [38] Karim Bouyarmane and Abderrahmane Kheddar. Humanoid robot locomotion and manipulation step planning. *Advanced Robotics*, (26):1099–1126, July/September 2012.

- [39] K. Hirai, M. Hirose, Y. Haikawa, and T. Takenaka. The development of honda humanoid robot. In *IEEE International Conference on Robotics and Automation*, volume 2, pages 1321–1326, Leuven, Belgium, May 1998. IEEE.
- [40] K. Kaneko, F. Kanehiro, S. Kajita, H. Hirukawa, T. Kawasaki, M. Hirata, K. Akachi, and T. Isozumi. Humanoid robot hrp-2. In *IEEE International Conference on Robotics and Automation*, pages 1083–1090, New Orleans, USA, April 2004.
- [41] O. Bruneau, F. B. Ouezdou, and J.-G. Fontaine. Dynamic walk of a bipedal robot having flexible feet. In *IEEE/RSJ International Conference on Intelligent Robots and Systems*, volume 1, pages 512–517, Maui, USA, 29 October 2001. IEEE.
- [42] Joris Vaillant, Abderrahmane Kheddar, Hervé Audren, François Keith, Stanislas Brossette, Adrien Escande, Karim Bouyarmane, Kenji Kaneko, Mitsuharu Morisawa, Pierre Gergondet, Eiichi Yoshida, Suuji Kajita, and Fumio Kanehiro. Multi-contact vertical ladder climbing with an hrp-2 humanoid. *Autonomous Robots*, 40(3):561–580, 2016.
- [43] J. Yamaguchi and A. Takanishi. Multisensor foot mechanism with shock absorbing material for dynamic biped walking adapting to unknown uneven surfaces. In *IEEE International Conference on Multisensor Fusion and Integration for Intelligent systems*, pages 233–240, Washington DC, USA, December 1996.
- [44] Giovanni De Magistris, Sylvain Miossec, Adrien Escande, and Abderrahmane Kheddar. Design of optimized compliant soles for humanoid robots. *Robotics and Autonomous Systems (RAS)*, page 1, 2016.
- [45] Marc Bonnet, Attilio Frangi, and Christian Rey. *The finite element method in solid mechanics*. McGraw Hill Education, 2014.
- [46] Marc Bonnet and Attilio Frangi. *Analyse des solides déformables par la méthode des éléments finis*. Ecole Polytechnique, département de Mécanique, 2005.
- [47] Morten Bro-Nielsen and Stephane Cotin. Real-time volumetric deformable models for surgery simulation using finite elements and condensation. *Computer Graphics Forum (Eurographics’96)*, 15:17, 1996.
- [48] Antonio Signorini. *Sopra alcune questioni di elastostatica*. Atti della Societa Italiana per il Progresso delle Scienze, 1933.
- [49] C Duriez, F Dubois, A Kheddar, and C Andriot. Realistic haptic rendering of interacting deformable objects in virtual environments. *IEEE Transactions on Visualization and Computer Graphics*, 12(1):36–47, 2006.
- [50] F. Jourdan, P. Alart, and M. Jean. A gauss-seidel like algorithm to solve frictional contact problems. *Computer Methods in Applied Mechanics and Engineering*, pages 33–47, 1998.
- [51] Joris De Schutter, Herman Bruyninckx, Wen-Hong Zhu, and Mark Spong. Force control: a bird’s eye view. *Control Problems in Robotics and Automation*, pages 1–17, 1998.

- [52] Karim Bouyarmane, Joris Vaillant, François Keith, and Abderrahmane Kheddar. Exploring humanoid robots locomotion capabilities in virtual disaster response scenarios. In *IEEE-RAS International Conference on Humanoid Robots*, Osaka, 2012.
- [53] Shuuji Kajita, Mitsuharu Morisawa, Kanako Miura, Shin'ichiro Nakaoka, Kensuke Harada, Kenji Kaneko, Fumio Kanehiro, and Kazuhito Yokoi. Biped walking stabilization based on linear inverted pendulum tracking. In *IEEE/RSJ International Conference on Intelligent Robots and Systems*, pages 4489–4496, Taipei, Taiwan, October 18 - 22 2010.
- [54] Mitsuharu Morisawa, Shuuji Kajita, Fumio Kanehiro, Kenji Kaneko, Kanako Miura, and Kazuhito Yokoi. Balance control based on capture point error compensation for biped walking on uneven terrain. In *Humanoid Robots (Humanoids), 2012 12th IEEE-RAS International Conference on*, pages 734–740. IEEE, 2012.
- [55] Tomomichi Sugihara. Standing stabilizability and stepping maneuver in planar bipedalism based on the best com-zmp regulator. In *Robotics and Automation, 2009. ICRA'09. IEEE International Conference on*, pages 1966–1971. IEEE, 2009.
- [56] Patrick M Wensing, Ghassan Bin Hammam, Behzad Dariush, and David E Orin. Optimizing foot centers of pressure through force distribution in a humanoid robot. *International Journal of Humanoid Robotics*, 10(03):1350027, 2013.
- [57] Stéphane Caron, Quang-Cuong Pham, and Yoshihiko Nakamura. Zmp support areas for multicontact mobility under frictional constraints. *IEEE Transactions on Robotics*, 33(1):67–80, 2017.
- [58] Justin Carpentier, Mehdi Benallegue, Nicolas Mansard, and Jean-Paul Laumond. Center-of-mass estimation for a polyarticulated system in contact - a spectral approach. *IEEE Transactions on Robotics*, 32(4):810–822, 2016.
- [59] K.G. Murty. Linear complementarity, linear and nonlinear programming. *Internet Edition*, 1997.
- [60] J.-J. Moreau and M. Jean. Numerical treatment of contact and friction: The contact dynamics method. *Engineering Systems Design and Analysis*, 4(1):201–208, 1996.
- [61] Michel Jean. Numerical methods for three dimensional dynamical problems. In *Conference in Contact Mechanics*, page 71, Southampton, 1993.
- [62] Pierre Alart. Critères d'injectivité et de surjectivité pour certaines applications de \mathbb{R}^n dans lui-même; application à la mécanique du contact. *ESAIM: Mathematical Modelling and Numerical Analysis - Modélisation Mathématique et Analyse Numérique*, 27(2):203–222, 1993.
- [63] Michel Jean. Documentation sur lmgc: Logiciel de mécanique gérant le contact. Technical report, Université la Méditerranée, Marseilles, January 1996.

Publications

Giovanni De Magistris, Adrien Pajon, Sylvain Miossec, and Abderrahmane Kheddar. Humanoid walking with compliant soles using a deformation estimator. In *International Conference on Robotics and Automation (ICRA)*, 2016.

Giovanni De Magistris*, Adrien Pajon*, Sylvain Miossec, and Abderrahmane Kheddar. Optimized humanoid walking with soft soles. *Robotics and Autonomous Systems*, 95:52–63, 2017. *Co-first authors.

Adrien Pajon, Stephane Caron, Giovanni De Magistris, Sylvain Miossec, and Abderrahmane Kheddar. Walking on gravel with soft soles using linear inverted pendulum tracking and reaction force distribution. In *IEEE-RAS International Conference on Humanoid Robots (Humanoids 2017)*. IEEE, november 2017.

Adrien Pajon, Enrico Chiovetto, Colleen Monaghan, Martin Giese, and Abderrahmane Kheddar. Adaptation of walking ground reaction forces to changes in ground stiffness properties. In *6th IEEE RAS & EMBS International Conference on Biomedical Robotics and Biomechatronics (BioRob 2016)*, singapore, jun 2016. IEEE.

Adrien Pajon, Giovanni De Magistris, Sylvain Miossec, Kenji Kaneko, and Abderrahmane Kheddar. A humanoid walking pattern generator for sole design optimization. In *Advanced Robotics (ICAR), 2015 International Conference on*, pages 105–110, Istanbul, Turkey, 2015. IEEE.

Appendix A

WPG : QP formulation

The WPG is formulated as a QP optimization problem to save computational time and solve:

$$\begin{cases} \min_X (E) \\ \text{subject to equality and inequality constraints} \end{cases} \quad (\text{A.1})$$

where the criteria E comes from (3.5) and it is based on a simplification of the energy consumption, and the optimization variables X . In this section, we detail the optimization variables and the different WPG gradients.

A.1 Optimization parameters and optimization criteria

A.1.1 Optimization parameters

The terms of (3.5) (\mathbf{F}_{COM} , $\mathbf{\Gamma}_a$ and $\ddot{\mathbf{P}}_{\text{ZMP}_i}$) are linear functions of optimization variables. They can be written as:

$$\begin{aligned} \mathbf{F}_{\text{COM}} &= \mathbf{A}_{\mathbf{F}_{\text{COM}}} X + \mathbf{B}_{\mathbf{F}_{\text{COM}}}, \\ \mathbf{\Gamma}_a &= \mathbf{A}_{\mathbf{\Gamma}_a} X + \mathbf{B}_{\mathbf{\Gamma}_a}, \\ \ddot{\mathbf{P}}_{\text{ZMP}_i} &= \mathbf{A}_{\ddot{\mathbf{P}}_{\text{ZMP}_i}} X + \mathbf{B}_{\ddot{\mathbf{P}}_{\text{ZMP}_i}} \end{aligned} \quad (\text{A.2})$$

where X is the vector of optimization variables:

$$X = \left[\mathbf{x}_0^{\text{vp}} \quad \mathbf{x}_0^{\text{COM}} \quad \mathbf{x}_0^{\text{step}} \quad \mathbf{x}_0^{\text{vp}'} \right]^T \quad (\text{A.3})$$

\mathbf{x}_0^{vp} represents the boundary conditions in position, speed and acceleration at via-points of ZMP ($3m + 3$ parameters), $\mathbf{x}_0^{\text{COM}}$ represents the initial and final boundary condition in position and speed of COM (4 parameters), $\mathbf{x}_0^{\text{step}}$ represents the foot step positions ($n - 1$

parameters) and $\mathbf{x}_0^{\text{vp}'}$ represents the boundary conditions in position, speed and acceleration at via-points of ZMP_1 ($3m + 6$ parameters). The terms of X have the form:

$$\begin{aligned}\mathbf{x}_0^{\text{vp}} &= \begin{bmatrix} x_0^{(1)} & \dot{x}_0^{(1)} & \ddot{x}_0^{(1)} & \cdots & x_0^{(m+1)} & \dot{x}_0^{(m+1)} & \ddot{x}_0^{(m+1)} \end{bmatrix}^T \\ \mathbf{x}_0^{\text{COM}} &= \begin{bmatrix} x_{\text{COM}}^{(1)}(t_0) & \dot{x}_{\text{COM}}^{(1)}(t_0) & x_{\text{COM}}^{(m+1)}(t_m) & \dot{x}_{\text{COM}}^{(m+1)}(t_m) \end{bmatrix}^T \\ \mathbf{x}_0^{\text{step}} &= \begin{bmatrix} x_1^{\text{step}} & x_2^{\text{step}} & \cdots & x_{n-1}^{\text{step}} \end{bmatrix}^T \\ \mathbf{x}_0^{\text{vp}'} &= \begin{bmatrix} x_1^{(1)} & \dot{x}_1^{(1)} & \ddot{x}_1^{(1)} & \cdots & x_1^{(m+1)} & \dot{x}_1^{(m+1)} & \ddot{x}_1^{(m+1)} \end{bmatrix}^T\end{aligned}$$

A.1.2 Optimization criteria

From (A.2) and (A.3), the energy consumption function can be written in a quadratic way:

$$E = \frac{1}{2} X^T \mathbf{H} X + \mathbf{G} X + \frac{1}{2} C \quad (\text{A.4})$$

Where

$$\begin{aligned}\mathbf{H} &= \lambda \mathbf{A}_{\mathbf{F}_{\text{COM}}}^T \mathbf{A}_{\mathbf{F}_{\text{COM}}} + (1 - \lambda) \mathbf{A}_{\Gamma_{\text{anSSP}}}^T \mathbf{A}_{\Gamma_{\text{anSSP}}} + \frac{1}{2} (1 - \lambda) (\mathbf{A}_{\Gamma_{\text{an}_1}}^T \mathbf{A}_{\Gamma_{\text{an}_1}} + \mathbf{A}_{\Gamma_{\text{an}_2}(t)}^T \mathbf{A}_{\Gamma_{\text{an}_2}(t)}) \\ &\quad + \varepsilon (\mathbf{A}_{\dot{\mathbf{p}}_{\text{ZMP}_1}}^T \mathbf{A}_{\dot{\mathbf{p}}_{\text{ZMP}_1}} + \mathbf{A}_{\dot{\mathbf{p}}_{\text{ZMP}_2}}^T \mathbf{A}_{\dot{\mathbf{p}}_{\text{ZMP}_2}}) \\ \mathbf{G} &= \lambda \mathbf{B}_{\mathbf{F}_{\text{COM}}}^T \mathbf{A}_{\mathbf{F}_{\text{COM}}} + (1 - \lambda) \mathbf{B}_{\Gamma_{\text{anSSP}}}^T \mathbf{A}_{\Gamma_{\text{anSSP}}} + \frac{1}{2} (1 - \lambda) (\mathbf{B}_{\Gamma_{\text{an}_1}}^T \mathbf{A}_{\Gamma_{\text{an}_1}} + \mathbf{B}_{\Gamma_{\text{an}_2}(t)}^T \mathbf{A}_{\Gamma_{\text{an}_2}(t)}) \\ &\quad + \varepsilon (\mathbf{B}_{\dot{\mathbf{p}}_{\text{ZMP}_1}}^T \mathbf{A}_{\dot{\mathbf{p}}_{\text{ZMP}_1}} + \mathbf{B}_{\dot{\mathbf{p}}_{\text{ZMP}_2}}^T \mathbf{A}_{\dot{\mathbf{p}}_{\text{ZMP}_2}}) \\ \mathbf{C} &= \lambda \mathbf{B}_{\mathbf{F}_{\text{COM}}}^T \mathbf{B}_{\mathbf{F}_{\text{COM}}} + (1 - \lambda) \mathbf{B}_{\Gamma_{\text{anSSP}}}^T \mathbf{B}_{\Gamma_{\text{anSSP}}} + \frac{1}{2} (1 - \lambda) (\mathbf{B}_{\Gamma_{\text{an}_1}}^T \mathbf{B}_{\Gamma_{\text{an}_1}} + \mathbf{B}_{\Gamma_{\text{an}_2}(t)}^T \mathbf{B}_{\Gamma_{\text{an}_2}(t)}) \\ &\quad + \varepsilon (\mathbf{B}_{\dot{\mathbf{p}}_{\text{ZMP}_1}}^T \mathbf{B}_{\dot{\mathbf{p}}_{\text{ZMP}_1}} + \mathbf{B}_{\dot{\mathbf{p}}_{\text{ZMP}_2}}^T \mathbf{B}_{\dot{\mathbf{p}}_{\text{ZMP}_2}})\end{aligned}$$

The different terms of \mathbf{H} , \mathbf{G} and \mathbf{C} will be detailed later on.

The optimization is realized along the direction \vec{x} and \vec{y} at the same time. Based on (A.4), the concatenation of E (3.5) along both directions is written in a quadratic way:

$$E = \frac{1}{2} \begin{bmatrix} X^x \\ X^y \end{bmatrix}^T \begin{bmatrix} H^x & 0 \\ 0 & H^y \end{bmatrix} \begin{bmatrix} X^x \\ X^y \end{bmatrix} + \begin{bmatrix} G^x & G^y \end{bmatrix} \begin{bmatrix} X^x \\ X^y \end{bmatrix} + \frac{1}{2} (C^x + C^y) \quad (\text{A.5})$$

A.2 Force and torque computation

The COM forces are defined by:

$$\mathbf{F}_{\text{COM}} = M (\ddot{\mathbf{P}}_{\text{COM}} - g\vec{z}) \quad (\text{A.6})$$

with the COM acceleration defined by:

$$\ddot{x}_{\text{COM}} = \frac{g}{z_{\text{COM}}} (x_{\text{COM}} - x_{\text{ZMP}}) \quad (\text{A.7})$$

and the ZMP and COM of the form:

$$x_{\text{COM}} = \mathbf{A}_{x_{\text{COM}}} X + B_{x_{\text{COM}}}$$

$$x_{\text{ZMP}} = \mathbf{A}_{x_{\text{ZMP}}} X + B_{x_{\text{ZMP}}}$$

Hence, the COM forces (A.6) can be rewritten in a linear way:

$$\begin{aligned} F_{\text{COM}}^x &= \mathbf{A}_{F_{\text{COM}}^x} X + B_{F_{\text{COM}}^x} \\ &= \frac{Mg}{z_{\text{COM}}} (\mathbf{A}_{x_{\text{COM}}} - \mathbf{A}_{x_{\text{ZMP}}}) X + \frac{Mg}{z_{\text{COM}}} (B_{x_{\text{COM}}} - B_{x_{\text{ZMP}}}) \end{aligned} \quad (\text{A.8})$$

The torques in ankle are defined by:

$$\begin{aligned} \Gamma_{an_g} &= \mathbf{F}_{\text{ZMP}_g} \times (\mathbf{P}_{an_g} - \mathbf{P}_{\text{ZMP}_g}) \\ \Gamma_{an_g}^y &= -F_{\text{ZMP}_g}^x \cdot h_{an_g} + F_{\text{ZMP}_g}^z \cdot (x_{an_g} - x_{\text{ZMP}_g}) \end{aligned} \quad (\text{A.9})$$

With h_{an_g} = height of the ankle g , $g \in \{\text{SSP}, 1, 2\}$ and:

$$\mathbf{F}_{\text{ZMP}} = -\mathbf{F}_{\text{COM}},$$

$$\mathbf{F}_{\text{ZMP}} = \mathbf{F}_{\text{ZMP}_1} + \mathbf{F}_{\text{ZMP}_2},$$

$$\mathbf{F}_{\text{ZMP}_2} = d \cdot \mathbf{F}_{\text{ZMP}},$$

d is a 5th order polynomial representing the distribution of ZMP force under each foot. The trajectories of ZMP_g and ankle g position are of the form:

$$\begin{aligned} x_{\text{ZMP}_g} &= \mathbf{A}_{x_{\text{ZMP}_g}} X + B_{x_{\text{ZMP}_g}}, \\ x_{an_g} &= \mathbf{A}_{x_{an_g}} X + B_{x_{an_g}} \end{aligned} \quad (\text{A.10})$$

Hence, the torques in ankle (A.9) can be rewritten in a linear way:

$$\begin{aligned}
\Gamma_{an_{SSP}}^y &= \frac{Mg}{z_{COM}} \cdot h_{an_{SSP}} (\mathbf{A}_{x_{COM}} - \mathbf{A}_{x_{ZMP}}) X - Mg (\mathbf{A}_{x_{an_{SSP}}} - \mathbf{A}_{x_{ZMP}}) X \\
&\quad + \frac{Mg}{z_{COM}} \cdot h_{an_{SSP}} (B_{x_{COM}} - B_{x_{ZMP}}) - Mg (B_{x_{an_{SSP}}} - B_{x_{ZMP}}) \\
\Gamma_{an_1}^y &= \frac{Mg}{z_{COM}} \cdot h_{an_1} \cdot (1-k) (\mathbf{A}_{x_{COM}} - \mathbf{A}_{x_{ZMP}}) X - Mg (\mathbf{A}_{x_{an_1}} - \mathbf{A}_{x_{ZMP_1}}) X \\
&\quad + \frac{Mg}{z_{COM}} \cdot h_{an_1} \cdot (1-k) (B_{x_{COM}} - B_{x_{ZMP}}) - Mg (B_{x_{an_1}} - B_{x_{ZMP_1}}) \\
\Gamma_{an_2}^y &= \frac{Mg}{z_{COM}} \cdot h_{an_2} \cdot k (\mathbf{A}_{x_{COM}} - \mathbf{A}_{x_{ZMP}}) X - Mg (\mathbf{A}_{x_{an_2}} - \mathbf{A}_{x_{ZMP_2}}) X \\
&\quad + \frac{Mg}{z_{COM}} \cdot h_{an_2} \cdot k (B_{x_{COM}} - B_{x_{ZMP}}) - Mg (B_{x_{an_2}} - B_{x_{ZMP_2}})
\end{aligned} \tag{A.11}$$

A.3 Global ZMP detailed

During the sequence number j , ZMP is defined by:

$$x_{ZMP}^{(j)}(t) = \sum_{i=0}^5 c_i^{(j)} (\Delta t_j)^i \tag{A.12}$$

Where c_i is the i^{th} polynomial coefficient, $\Delta t_j = t - T_j$ and T_j is the time at the beginning of the sequence j .

ZMP polynomials are interpolated between two via-points and verify boundary conditions in position, velocity and acceleration. Thus polynomial coefficients of the sequence j are defined by:

$$\begin{bmatrix} c_0^{(j)} \\ c_1^{(j)} \\ \vdots \\ c_5^{(j)} \end{bmatrix} = \begin{bmatrix} \mathbf{C}c_{012}^{(j)} & \mathbf{C}c_{345}^{(j)} \end{bmatrix} \begin{bmatrix} x_0^{(j)} \\ \dot{x}_0^{(j)} \\ \ddot{x}_0^{(j)} \\ x_0^{(j+1)} \\ \dot{x}_0^{(j+1)} \\ \ddot{x}_0^{(j+1)} \end{bmatrix} \tag{A.13}$$

Where $\mathbf{C}\mathbf{c}_{012}^{(j)}$ and $\mathbf{C}\mathbf{c}_{345}^{(j)}$ are 6×3 matrix, $\Delta T_j = T_{j+1} - T_j$ and $x_0^{(j)}$ is the position of the via-point at the beginning of the sequence j . $\mathbf{C}\mathbf{c}_{012}^{(j)}$ and $\mathbf{C}\mathbf{c}_{345}^{(j)}$ are defined by:

$$\begin{bmatrix} \mathbf{C}\mathbf{c}_{012}^{(j)} & \mathbf{C}\mathbf{c}_{345}^{(j)} \end{bmatrix} = \begin{bmatrix} 1 & 0 & 0 & 0 & 0 & 0 \\ 0 & 1 & 0 & 0 & 0 & 0 \\ 0 & 0 & 2 & 0 & 0 & 0 \\ 1 & \Delta T_j & (\Delta T_j)^2 & (\Delta T_j)^3 & (\Delta T_j)^4 & (\Delta T_j)^5 \\ 0 & 1 & 2(\Delta T_j) & 3(\Delta T_j)^2 & 4(\Delta T_j)^3 & 5(\Delta T_j)^4 \\ 0 & 0 & 2 & 6(\Delta T_j) & 12(\Delta T_j)^2 & 20(\Delta T_j)^3 \end{bmatrix}^{-1} \quad (\text{A.14})$$

The boundary conditions of ZMP induce that $\begin{bmatrix} x_0^{(j)} & \dot{x}_0^{(j)} & \ddot{x}_0^{(j)} \end{bmatrix}^T$ correspond to the ending boundary conditions of the phase $j - 1$ and the starting boundary conditions of the phase j . From concatenation of $\mathbf{C}\mathbf{c}_{012}^{(j)}$ and $\mathbf{C}\mathbf{c}_{345}^{(j)}$ matrices (A.14), we obtain the $\mathbf{C}\mathbf{c}$ matrix as:

$$\mathbf{C}\mathbf{c} = \begin{bmatrix} \mathbf{C}\mathbf{c}_{012}^{(1)} & \mathbf{C}\mathbf{c}_{345}^{(1)} & 0 & 0 & \dots & \dots & \dots & 0 \\ 0 & \mathbf{C}\mathbf{c}_{012}^{(2)} & \mathbf{C}\mathbf{c}_{345}^{(2)} & 0 & \dots & \dots & \dots & 0 \\ \vdots & & & \ddots & \ddots & & & \vdots \\ 0 & \dots & \dots & \dots & 0 & \mathbf{C}\mathbf{c}_{012}^{(m-1)} & \mathbf{C}\mathbf{c}_{345}^{(m-1)} & 0 \\ 0 & \dots & \dots & \dots & 0 & 0 & \mathbf{C}\mathbf{c}_{012}^{(m)} & \mathbf{C}\mathbf{c}_{345}^{(m)} \end{bmatrix}_{6m \times 3(2m+1)} \quad (\text{A.15})$$

where $m = 3n + 2$ is the number of sequence.

Thus, the ZMP polynomial coefficients are obtained with:

$$\begin{bmatrix} c_0^{(0)} & c_1^{(0)} & \dots & c_5^{(0)} & \dots & c_5^{(m)} \end{bmatrix}^T = \mathbf{C}\mathbf{c} \cdot \mathbf{x}_0^{vp} \quad (\text{A.16})$$

with the term of the optimization parameters:

$$\mathbf{x}_0^{vp} = \begin{bmatrix} x_0^{(1)} & \dot{x}_0^{(1)} & \ddot{x}_0^{(1)} & x_0^{(2)} & \dots & \ddot{x}_0^{(m+1)} \end{bmatrix}^T \quad (\text{A.17})$$

To discretize the ZMP, the time discretization matrix is defined by:

$$\mathbf{M}_t = \begin{bmatrix} \mathbf{t}(t_1, 1) & 0 & \dots & 0 \\ \mathbf{dt}(1) & 0 & \dots & \vdots \\ 0 & \mathbf{dt}(2) & & \vdots \\ \vdots & & \ddots & 0 \\ 0 & \dots & \dots & \mathbf{dt}(m) \end{bmatrix} \quad (\text{A.18})$$

where dt is the discretization time period of the phase j and:

$$\mathbf{t}(t, j) = \begin{bmatrix} 1 & \Delta t_j & (\Delta t_j)^2 & (\Delta t_j)^3 & (\Delta t_j)^4 & (\Delta t_j)^5 \end{bmatrix},$$

$$\mathbf{dt}(j) = \begin{bmatrix} \mathbf{t}(t + dt, j) \\ \mathbf{t}(t + 2dt, j) \\ \vdots \\ \mathbf{t}(t_{j+1}, j) \end{bmatrix} \quad (\text{A.19})$$

The ZMP trajectory can be written in a linear way:

$$\begin{aligned} x_{\text{ZMP}} &= \mathbf{A}_{x_{\text{ZMP}}} X + \mathbf{B}_{x_{\text{ZMP}}} \\ &= \mathbf{M}_t \cdot \mathbf{C} \mathbf{c} \cdot \mathbf{x}_0^{vP} \end{aligned} \quad (\text{A.20})$$

Thus

$$\begin{aligned} \mathbf{A}_{x_{\text{ZMP}}} &= \mathbf{M}_t \begin{bmatrix} \mathbf{C} \mathbf{c} & 0 \end{bmatrix} \\ \mathbf{B}_{x_{\text{ZMP}}} &= 0 \end{aligned} \quad (\text{A.21})$$

A.4 COM detailed

In section 3.5.3, we detailed the system of equation (3.24) in order to obtain the COM trajectories from the ZMP trajectories. From (3.24), the part related to the ZMP polynomial coefficients is:

$$\begin{bmatrix} C_0^{(j)} \\ C_1^{(j)} \\ \vdots \\ C_5^{(j)} \end{bmatrix} = \begin{bmatrix} \mathbf{C}^{(j)} \end{bmatrix} \begin{bmatrix} c_0^{(j)} \\ c_1^{(j)} \\ \vdots \\ c_5^{(j)} \end{bmatrix} \quad (\text{A.22})$$

with $\mathbf{C}^{(j)}$ define as:

$$\mathbf{C}^{(j)} = \begin{bmatrix} 1 & 0 & 2/w^2 & 0 & 24/w^4 & 0 \\ 0 & 1 & 0 & 6/w^2 & 0 & 120/w^4 \\ 0 & 0 & 1 & 0 & 12/w^2 & 0 \\ 0 & 0 & 0 & 1 & 0 & 20/w^2 \\ 0 & 0 & 0 & 0 & 1 & 0 \\ 0 & 0 & 0 & 0 & 0 & 1 \end{bmatrix} \quad (\text{A.23})$$

From concatenation of $\mathbf{C}^{(j)}$ matrices (A.23), we obtain the \mathbf{C} matrix as:

$$\mathbf{C} = \begin{bmatrix} \mathbf{C}^{(1)} & 0 & \dots & 0 \\ 0 & \mathbf{C}^{(2)} & & \vdots \\ \vdots & & \ddots & \\ 0 & \dots & \dots & \mathbf{C}^{(m)} \end{bmatrix} \quad (\text{A.24})$$

From (3.31), the matrix \mathbf{I} can be written in a linear way:

$$\begin{aligned} \mathbf{I} &= \left[C_0^{(1)} \dots C_5^{(1)} \dots C_0^{(m)} \dots C_5^{(m)} \right]^T \\ &= \mathbf{C} \cdot \mathbf{C} \mathbf{c} \cdot \mathbf{x}_0^{vp} \\ &= \begin{bmatrix} \mathbf{C} \cdot \mathbf{C} \mathbf{c} & 0 \end{bmatrix} X \end{aligned} \quad (\text{A.25})$$

By replacing into (3.31):

$$\begin{aligned} \mathbf{y} &= \left[V^{(1)} \quad W^{(1)} \quad \dots \quad V^{(j)} \quad W^{(j)} \quad \dots \quad V^{(ns)} \quad W^{(ns)} \right]^T \\ &= \mathbf{G}^{-1} (\mathbf{N} \cdot \mathbf{x}_0^{\text{COM}} + \mathbf{H} \cdot \mathbf{C} \cdot \mathbf{C} \mathbf{c} \cdot \mathbf{x}_0^{vp}) \\ &= \mathbf{G}^{-1} \begin{bmatrix} \mathbf{H} \cdot \mathbf{C} \cdot \mathbf{C} \mathbf{c} & \mathbf{N} & 0 \end{bmatrix} X \end{aligned} \quad (\text{A.26})$$

To discretize the COM trajectory, the discretized *cosh* and *sinh* term of (3.24) are:

$$\mathbf{M}_{cs} = \begin{bmatrix} \mathbf{cs}(t_1, 1) & 0 & \dots & 0 \\ \mathbf{dcs}(1) & 0 & \dots & \vdots \\ 0 & \mathbf{dcs}(2) & & \vdots \\ \vdots & & \ddots & 0 \\ 0 & \dots & \dots & \mathbf{dcs}(ns) \end{bmatrix} \quad (\text{A.27})$$

where dt is the discretization time period of the phase j and:

$$\begin{aligned} \mathbf{cs}(t, j) &= \begin{bmatrix} \cosh(\omega_j \Delta t_j) & \sinh(\omega_j \Delta t_j) \end{bmatrix} \\ \mathbf{dcs}(j) &= \begin{bmatrix} \mathbf{cs}(t_j + dt^{(j)}, j) & \mathbf{cs}(t_j + 2dt^{(j)}, j) & \dots & \mathbf{cs}(t_{j+1}, j) \end{bmatrix}^T \end{aligned} \quad (\text{A.28})$$

From (3.31), (A.25) and (A.27), COM can be written in a linear way:

$$\begin{aligned}
x_{\text{COM}} &= \mathbf{A}_{x_{\text{COM}}} X + B_{x_{\text{COM}}} \\
&= \mathbf{M}_{cs} \cdot \mathbf{y} + \mathbf{M}_t \cdot \mathbf{l} \\
&= \mathbf{M}_{cs} \cdot \mathbf{G}^{-1} \left[\mathbf{H} \cdot \mathbf{C} \cdot \mathbf{C}c \quad \mathbf{N} \quad 0 \right] X + \mathbf{M}_t \cdot \left[\mathbf{C} \cdot \mathbf{C}c \quad 0 \right] X \\
&= \left[\mathbf{M}_{cs} \cdot \mathbf{G}^{-1} \cdot \mathbf{H} \cdot \mathbf{C} \cdot \mathbf{C}c + \mathbf{M}_t \cdot \mathbf{C} \cdot \mathbf{C}c \quad \mathbf{M}_{cs} \cdot \mathbf{G}^{-1} \cdot \mathbf{N} \quad 0 \right] X
\end{aligned} \tag{A.29}$$

Thus

$$\begin{aligned}
\mathbf{A}_{x_{\text{COM}}} &= \left[\mathbf{M}_{cs} \cdot \mathbf{G}^{-1} \cdot \mathbf{H} \cdot \mathbf{C} \cdot \mathbf{C}c + \mathbf{M}_t \cdot \mathbf{C} \cdot \mathbf{C}c \quad \mathbf{M}_{cs} \cdot \mathbf{G}^{-1} \cdot \mathbf{N} \quad 0 \right] \\
B_{x_{\text{COM}}} &= 0
\end{aligned} \tag{A.30}$$

A.5 Ankle position detailed

Ankle positions are equivalent to foot step positions:

$$\mathbf{x}_0^{\text{step}} = \left[x_1^{\text{step}} \quad x_2^{\text{step}} \quad \dots \quad x_{nfs}^{\text{step}} \right] \tag{A.31}$$

where $nfs = n + 2$ is the number of foot step.

Foot step positions in SSP can be expressed in a linear way as:

$$\mathbf{A}_{x_{an_{SSP}}} = \mathbf{M}_{an_{SSP}} \cdot \mathbf{x}_0^{\text{step}} = \left[0 \quad \mathbf{M}_{an_{SSP}} \quad 0 \right] X \tag{A.32}$$

with:

$$\mathbf{M}_{an_{SSP}}^{(m,n)} = \begin{cases} 1 & \text{for } m = \text{SSP increments and } n = \text{corresponding SSP foot step} \\ 0 & \text{otherwise} \end{cases} \tag{A.33}$$

Foot 1 step positions in DSP can be expressed in a linear way as:

$$\mathbf{A}_{x_{an_1}} = \mathbf{M}_{an_1} \cdot \mathbf{x}_0^{\text{step}} = \left[0 \quad \mathbf{M}_{an_1} \quad 0 \right] X \tag{A.34}$$

with

$$\mathbf{M}_{an_1}^{(m,n)} = \begin{cases} 1 & \text{for } m = \text{DSP increments and } n = \text{corresponding DSP foot}_1 \text{ step} \\ 0 & \text{otherwise} \end{cases} \tag{A.35}$$

Foot 1 step positions in DSP can be expressed in a linear way as:

$$\mathbf{A}_{x_{an_2}} = \mathbf{M}_{an_2} \cdot \mathbf{x}_0^{\text{step}} = \begin{bmatrix} 0 & \mathbf{M}_{an_2} & 0 \end{bmatrix} X \quad (\text{A.36})$$

with

$$\mathbf{M}_{an_2}^{(m,n)} = \begin{cases} 1 & \text{for } m = \text{DSP increments and } n = \text{corresponding DSP foot}_2 \text{ step} \\ 0 & \text{otherwise} \end{cases} \quad (\text{A.37})$$

Where $n = 1, \dots, nfs$, $m = 1, \dots, nd$, and $nd = 1 + \sum_{i=1}^{ns} \lceil (t_{i+1} - t_i) / dt^{(i)} \rceil$ is the total number of discretized points.

A.6 Local ZMP detailed and force distribution

During the sequence number $j \in \text{DSP}$, ZMP_1 is defined by:

$$x_{\text{ZMP}_1}^{(j)}(t) = \sum_{i=0}^5 c_{1,i}^{(j)} (\Delta t_j)^i \quad (\text{A.38})$$

Where $c_{1,i}$ is the i^{th} polynomial coefficient, $\Delta t_j = t - T_j$ and T_j is the time at the beginning of the sequence j .

As ZMP, ZMP_1 polynomials are interpolated between two via-points and verify boundary conditions in position, velocity and acceleration. Thus polynomial coefficients of the sequence $j \in \text{DSP}$ are defined by:

$$\begin{bmatrix} c_{1,0}^{(j)} \\ c_{1,1}^{(j)} \\ \vdots \\ c_{1,5}^{(j)} \end{bmatrix} = \begin{bmatrix} \mathbf{C}\mathbf{c}_{1,012}^{(j)} & \mathbf{C}\mathbf{c}_{1,345}^{(j)} \end{bmatrix} \begin{bmatrix} x_0^{(j)} \\ \dot{x}_0^{(j)} \\ \ddot{x}_0^{(j)} \\ x_1^{(j)} \\ \dot{x}_1^{(j)} \\ \ddot{x}_1^{(j)} \end{bmatrix} \quad (\text{A.39})$$

Where $\mathbf{C}\mathbf{c}_{1,012}^{(j)}$ and $\mathbf{C}\mathbf{c}_{1,345}^{(j)}$ are 6×3 matrix, $\Delta T_j = t_{j+1} - t_j$, $x_0^{(j)}$ is the position of the via-point at the beginning of the sequence $j \in \text{DSP}$ and $x_1^{(j)}$ is the position of the via-points at the end of the DSP. Because ZMP_1 exist only in DSP, $j \in \text{DSP}$ is equivalent to:

$$j \in \text{DSP} \equiv j \in \{1, 3[1 \dots n], m\} \quad (\text{A.40})$$

To enforce the boundary conditions with the global ZMP, the via-points at the beginning of the sequence $j \in \text{DSP}$ are common for the ZMP and ZMP_1 .

During the starting phase, the robot begins to walk with a DSP and its ZMP between the feet. From the definition, in that case, the ZMP and ZMP_1 have no common boundary conditions and the polynomials coefficient of ZMP_1 are defined by:

$$\begin{bmatrix} c_{1,0}^{(1)} \\ c_{1,1}^{(1)} \\ \vdots \\ c_{1,5}^{(1)} \end{bmatrix} = \begin{bmatrix} \mathbf{C}\mathbf{c}_{1,012}^{(1)} & \mathbf{C}\mathbf{c}_{1,345}^{(1)} \end{bmatrix} \begin{bmatrix} x_1^{(1)} \\ \dot{x}_1^{(1)} \\ \ddot{x}_1^{(1)} \\ x_1^{(2)} \\ \dot{x}_1^{(2)} \\ \ddot{x}_1^{(2)} \end{bmatrix} \quad (\text{A.41})$$

$\mathbf{C}\mathbf{c}_{1,012}^{(j)}$ and $\mathbf{C}\mathbf{c}_{1,345}^{(j)}$ are defined by:

$$\begin{bmatrix} \mathbf{C}\mathbf{c}_{1,012}^{(j)} & \mathbf{C}\mathbf{c}_{1,345}^{(j)} \end{bmatrix} = \begin{bmatrix} 1 & 0 & 0 & 0 & 0 & 0 \\ 0 & 1 & 0 & 0 & 0 & 0 \\ 0 & 0 & 2 & 0 & 0 & 0 \\ 1 & \Delta T_j & (\Delta T_j)^2 & (\Delta T_j)^3 & (\Delta T_j)^4 & (\Delta T_j)^5 \\ 0 & 1 & 2(\Delta T_j) & 3(\Delta T_j)^2 & 4(\Delta T_j)^3 & 5(\Delta T_j)^4 \\ 0 & 0 & 2 & 6(\Delta T_j) & 12(\Delta T_j)^2 & 20(\Delta T_j)^3 \end{bmatrix}^{-1} \quad (\text{A.42})$$

From the concatenation of $\mathbf{C}\mathbf{c}_{1,012}^{(j)}$ and $\mathbf{C}\mathbf{c}_{1,345}^{(j)}$ matrices (A.42), we obtain the $\mathbf{C}\mathbf{c}_1$ matrix as:

$$\mathbf{C}\mathbf{c}_1 = \begin{bmatrix} \mathbf{C}\mathbf{c}_{1,1} & 0 & 0 & \mathbf{C}\mathbf{c}_{1,2} \end{bmatrix} \quad (\text{A.43})$$

with

$$\mathbf{C}\mathbf{c}_{1,1}^{(r,s)} = \begin{cases} \mathbf{C}\mathbf{c}_{1,012}^{(s)} & \text{for } s = 3(r-1) \text{ with } r \in \{2 \dots n+1\} \\ \mathbf{C}\mathbf{c}_{1,012}^{(m+1)} & \text{for } r = n+2 \text{ and } s = m+1 \\ 0 & \text{otherwise} \end{cases}$$

$$\mathbf{C}\mathbf{c}_{1,2} = \begin{bmatrix} \mathbf{C}\mathbf{c}_{1,345}^{(1)} & \mathbf{C}\mathbf{c}_{1,345}^{(2)} & 0 & 0 & \dots & 0 \\ 0 & 0 & \mathbf{C}\mathbf{c}_{1,345}^{(3)} & 0 & & \vdots \\ \vdots & & & \ddots & & \vdots \\ 0 & \dots & & & \dots & \mathbf{C}\mathbf{c}_{1,345}^{(m+1)} \end{bmatrix}$$

Thus, the ZMP_1 polynomial coefficients are obtained with:

$$\begin{bmatrix} c_{1,0}^{(0)} & c_{1,1}^{(0)} & \dots & c_{1,5}^{(0)} & \dots & c_{1,5}^{(n+1)} \end{bmatrix}^T = \mathbf{C}\mathbf{c}_1 \begin{bmatrix} \mathbf{x}_0^{vp} \\ \mathbf{x}_0^{\text{COM}} \\ \mathbf{x}_0^{\text{step}} \\ \mathbf{x}_1^{vp'} \end{bmatrix} \quad (\text{A.44})$$

The ZMP_1 trajectory can be written in a linear way:

$$\begin{aligned} x_{ZMP_1} &= \mathbf{A}_{x_{ZMP_1}} X + \mathbf{B}_{x_{ZMP_1}} \\ &= \mathbf{M}_t \cdot \mathbf{C}\mathbf{c}_1 \cdot X \end{aligned} \quad (\text{A.45})$$

with \mathbf{M}_t defined for $j \in \text{DSP}$. Thus

$$\begin{aligned} \mathbf{A}_{x_{ZMP_1}} &= \mathbf{M}_t \cdot \mathbf{C}\mathbf{c}_1 \\ \mathbf{B}_{x_{ZMP_1}} &= 0 \end{aligned} \quad (\text{A.46})$$

The ZMP_2 is obtained with:

$$x_{ZMP_2}^{(j)} = x_{ZMP_1}^{(j)} - \frac{1}{d^{(j)}} (x_{ZMP_1}^{(j)} - x_{ZMP}^{(j)}) \quad (\text{A.47})$$

The force distribution between the feet is an interpolation of 5th order polynomials between boundary conditions defined in (3.19) and (3.20). Thus d is defined by:

$$\begin{aligned} d^{(j)} &= \mathbf{d}\mathbf{t}^{(j)} \cdot \begin{bmatrix} \mathbf{C}\mathbf{a}_{012}^{(j)} & \mathbf{C}\mathbf{a}_{345}^{(j)} \end{bmatrix} \cdot \begin{bmatrix} 0 \\ 0 \\ 0 \\ 1 \\ 0 \\ 0 \\ 0 \end{bmatrix} \\ \mathbf{d}^{r,1} &= \begin{cases} d^{(r)} & \text{for } r = \text{DSP sequence} \\ 0 & \text{otherwise} \end{cases} \end{aligned} \quad (\text{A.48})$$

The ZMP_2 trajectory can be written in linear way:

$$\begin{aligned} x_{ZMP_2} &= \mathbf{A}_{x_{ZMP_2}} X + \mathbf{B}_{x_{ZMP_2}} \\ &= \mathbf{A}_{x_{ZMP_1}} X + \mathbf{B}_{x_{ZMP_1}} - (\text{diag}(\mathbf{d}))^{-1} \cdot ((\mathbf{A}_{x_{ZMP_1}} - \mathbf{A}_{x_{ZMP}}) X + (\mathbf{B}_{x_{ZMP_1}} - \mathbf{B}_{x_{ZMP}})) = 0 \end{aligned} \quad (\text{A.49})$$

Thus

$$\begin{aligned}\mathbf{A}_{x_{ZMP_2}} &= \mathbf{A}_{x_{ZMP_1}} - (\text{diag}(\mathbf{d}))^{-1} \cdot (\mathbf{A}_{x_{ZMP_1}} - \mathbf{A}_{x_{ZMP}}) \\ \mathbf{B}_{x_{ZMP_2}} &= \mathbf{B}_{x_{ZMP_1}} - (\text{diag}(\mathbf{d}))^{-1} \cdot (\mathbf{B}_{x_{ZMP_1}} - \mathbf{B}_{x_{ZMP}})\end{aligned}\tag{A.50}$$

Appendix B

Detail of the Frictional contact problem

B.1 Signorini's law

To find the interpenetration distances and forces, we can formulate the contact problem as a linear complementarity problem (LCP) [59]. Various methods, direct or iterative are possible to solve LCP. For our applications, we use an iterative solver Gauss-Seidel based on [49]. Using this contact resolution, LCP takes into account the coupling between the different contact points.

In our simulation, different forces are applied to the sole. We can classify this forces in two types: the forces that we know at the beginning of the time step (*explicit forces*, i.e. gravity force) and the unknown forces (*implicit forces*, i.e. contact forces). Using the explicit forces, we obtain the movement of the robot foot. We can qualified this as *free movement*.

In this case, the surface node positions of the sole are given by the following relationship (see figure 4.4):

$$\underline{\mathbf{P}}^{\text{free}} = \begin{bmatrix} \overrightarrow{OO_l} \\ \vdots \\ \overrightarrow{OO_l} \end{bmatrix} + \begin{bmatrix} \overrightarrow{O_l P_1} \\ \vdots \\ \overrightarrow{O_l P_m} \end{bmatrix} = \underline{\mathbf{O}}_l + {}^l \underline{\mathbf{P}}^{\text{free}} \quad (\text{B.1})$$

The subscript l denotes the local sole frame.

$\mathbf{H} = \text{diag}(\mathbf{R}, \dots, \mathbf{R})$, where \mathbf{R} is the rotation matrix dependent of the foot orientation (θ, ϕ, ψ) to project vector from the global frame to the sole frame.

When a point come into contact, the explicit force and the implicit forces are applied to the sole. The movement given by the contact forces is called *constraint movement*.

In order to obtain \mathbf{P}_α and \mathbf{Q}_α and solve this problem, the displacement $\underline{\mathbf{U}}_S$ of equation (4.6) (in absolute frame) is used:

$$\underline{\mathbf{U}}_S = \underline{\mathbf{P}} - \underline{\mathbf{P}}^{\text{free}} \quad (\text{B.2})$$

Using the linear relationship (4.6), the node position of each sole surface node is then composed of two terms:

$$\underline{\mathbf{P}} = \mathbf{H}\mathbf{C}_S\mathbf{H}^T \underline{\mathbf{F}} + \underline{\mathbf{P}}^{\text{free}} \stackrel{\text{def}}{=} \mathbf{W}\underline{\mathbf{F}} + \underline{\mathbf{O}}_l + \mathbf{H} \mathbf{l}\underline{\mathbf{P}}^{\text{free}} \quad (\text{B.3})$$

where $\mathbf{W} = \mathbf{H}\mathbf{C}_S\mathbf{H}^T$ is the Delassus' operator [60]; $\mathbf{H} = \text{diag}(\mathbf{R}, \dots, \mathbf{R})$, where \mathbf{R} is the foot orientation matrix defined by $\mathbf{Y} = (\theta, \phi, \psi)$.

By the definition of δ as the interpenetration distance between two nodes of the two objects (sole and ground), we can write:

$$\begin{aligned} \underline{\delta} &= \underline{\mathbf{P}} - \underline{\mathbf{Q}} \\ &= \mathbf{W}\underline{\mathbf{F}} + \underline{\mathbf{O}}_l + \mathbf{H} \mathbf{l}\underline{\mathbf{P}}^{\text{free}} - \underline{\mathbf{Q}} \\ &= \mathbf{W}\underline{\mathbf{F}} + \underline{\delta}^{\text{free}} \end{aligned} \quad (\text{B.4})$$

where $\underline{\mathbf{Q}} = \left[\left[\begin{array}{c} \mathbf{P}_{t,1}^{(t_s-1)} \\ 0 \end{array} \right]^T \dots \left[\begin{array}{c} \mathbf{P}_{t,c_n}^{(t_s-1)} \\ 0 \end{array} \right]^T \right]^T$.

From (B.4), we obtain the normal component of the interpenetration distance for each contact point α as:

$$\begin{aligned} \delta_{n,\alpha} &= \mathbf{n}\underline{\mathbf{O}}_l + \mathbf{n}\mathbf{R} \mathbf{l}\underline{\mathbf{P}}_\alpha^{\text{free}} + \mathbf{n} \sum_{\beta=1}^{c_n} (\mathbf{W}_{\alpha\beta} \underline{\mathbf{F}}_\beta) \\ &\stackrel{\text{def}}{=} \delta_{n,\alpha}^{\text{free}} + \mathbf{n} \sum_{\beta=1}^{c_n} (\mathbf{W}_{\alpha\beta} \underline{\mathbf{F}}_\beta) \end{aligned} \quad (\text{B.5})$$

where $\mathbf{W}_{\alpha\beta} \stackrel{\text{def}}{=} \begin{bmatrix} W_t \\ W_n \end{bmatrix} \stackrel{\text{def}}{=} \begin{bmatrix} W_{tt} & W_{tn} \\ W_{nt} & W_{nn} \end{bmatrix}$ is the 3×3 Delassus' operator coupling the contacts α and β and c_n is the number of contact nodes.

The Signorini's problem can be solved using the following LCP:

$$\begin{cases} \mathbf{F}_n \geq 0 \\ \delta_n = \mathbf{W}_n \underline{\mathbf{F}}_{S,n} + \delta_n^{\text{free}} \geq 0 \\ \mathbf{F}_n \perp \delta_n \end{cases} \quad (\text{B.6})$$

B.2 Coulomb's law

In this section we explain how we added the equations to respect the Coulomb's law. In 3D case, this law add one non-linearity to the initial contact problem.

To solve this problem, two approaches are commonly used in the literature: (i) multi-sided pyramids instead of friction cone [59] and (ii) seeking an approximate solution by a Newton's method [61].

Using the first method, we can stack multiple contacts with friction in a global LCP. However, if we choose to model the friction with pyramids of 4 facets, each contact generate six new lines in the LCP. The size of the matrix of LCP is $6s \times 6s$, with s is the number of sliding contacts. In addition, the accuracy will be very approximate because of the use of pyramids of 4 facets.

The second method [61] is based on the Newton's method. In this section, we explain how this method find a solution in case of only one node is in contact with the ground.

From (B.4), we find the tangential component of the interpenetration distance:

$$\begin{aligned}
 \boldsymbol{\delta}_{t,\alpha} &= \mathbf{t}\mathbf{O}_{l,\alpha} + \mathbf{t}\mathbf{R} \mathbf{l}\mathbf{P}_{\alpha}^{\text{free}} + \mathbf{t} \sum_{\beta=1}^{c_n} (\mathbf{W}_{\alpha\beta} \mathbf{F}_{\beta}) - \mathbf{t}\mathbf{Q}_{\alpha} \\
 &\approx \mathbf{t}\mathbf{O}_{l,\alpha} + \mathbf{t}\mathbf{R} \mathbf{l}\mathbf{P}_{\alpha}^{\text{free}} + \mathbf{t} \sum_{\beta=1}^{c_n} (\mathbf{W}_{\alpha\beta} \mathbf{F}_{\beta}) - \mathbf{t}\mathbf{P}_{\alpha}^{(q-1)} \\
 &\stackrel{\text{def}}{=} \boldsymbol{\delta}_{t,\alpha}^{\text{free}} + \mathbf{t} \sum_{\beta=1}^m (\mathbf{W}_{\alpha\beta} \mathbf{F}_{\beta})
 \end{aligned} \tag{B.7}$$

If at $t_s - 1$ a node α is already in contact, the reference node at t_s is $\mathbf{P}_{\alpha}^{(t_s-1)}$. If α is not in contact at $t_s - 1$, the reference contact node at t_s is approximated by the normal projection of α on the ground at $t_s - 1$. In reality, the contact creation occurs at an intermediate time step between $t_s - 1$ and t_s . The contact creation position could be found with a variable step size and an event driven simulation. This can be computationally costly for a large number of new contact nodes. However, with a small time-step, the approximation error is negligible.

From (B.5) and (B.7), we obtain:

$$\begin{aligned}
 \boldsymbol{\delta}_{\alpha} &= \mathbf{O}_{l,\alpha} + \mathbf{R} \mathbf{l}\mathbf{P}_{\alpha}^{\text{free}} - \begin{bmatrix} \mathbf{P}_{t,\alpha}^{(q-1)} \\ 0 \end{bmatrix} + \sum_{\beta=1}^m \mathbf{W}_{\alpha\beta} \mathbf{F}_{\beta} \\
 &= \boldsymbol{\delta}_{\alpha}^{\text{free}} + \sum_{\beta=1}^m \mathbf{W}_{\alpha\beta} \mathbf{F}_{\beta}
 \end{aligned} \tag{B.8}$$

Using (B.5) and (B.7) and Coulomb's law, we build for each contact an application $\Phi \in \mathbb{R}^2 \times \mathbb{R} \times \mathbb{R}^2 \times \mathbb{R}$:

$$\begin{cases} \Phi_1(\boldsymbol{\delta}, \mathbf{F}) = \boldsymbol{\delta}_t - \boldsymbol{\delta}_t^{free} - \mathbf{W}_{tn}F_n - \mathbf{W}_{tt}\mathbf{F}_t \in \mathbb{R}^2 \\ \Phi_2(\boldsymbol{\delta}, \mathbf{F}) = \delta_n - \delta_n^{free} - W_{nn}F_n - W_{nt}\mathbf{F}_t \in \mathbb{R} \\ \Phi_3(\boldsymbol{\delta}, \mathbf{F}) = \mathbf{F}_t - \frac{\mu F_n (\mathbf{F}_t - q_t \boldsymbol{\delta}_t)}{\|\mathbf{F}_t - q_t \boldsymbol{\delta}_t\|} \in \mathbb{R}^2 \\ \Phi_4(\boldsymbol{\delta}, \mathbf{F}) = q_n \delta_n \in \mathbb{R} \end{cases} \quad (\text{B.9})$$

This application is composed by the first three lines given by (B.8) and in the last tree lines we find the Signorini's and Coulomb's law in the case of frictional contact. So to solve (B.9), we need to find a couple $(\boldsymbol{\delta}, \mathbf{F})$ such as $\Phi(\boldsymbol{\delta}, \mathbf{F}) = 0$.

Alart [62] explains that a Newton method can be applied to this type of function. Detail about the convergence are given in [62]. Based on [63], we chose the coefficients q_n and q_t as:

$$q_n = \frac{1}{W_{nn}}, \quad q_t = \frac{\lambda_{min}}{\lambda_{max}^2} \quad (\text{B.10})$$

where λ_{min} and λ_{max} are respectively the min and max eigenvalue of the matrix \mathbf{W}_{tt} .

To solve (B.9), we use the Newton's iteration method:

$$\begin{bmatrix} \boldsymbol{\delta}_\alpha^{(r)} \\ \mathbf{F}_\alpha^{(r)} \end{bmatrix} = \begin{bmatrix} \boldsymbol{\delta}_\alpha^{(r-1)} \\ \mathbf{F}_\alpha^{(r-1)} \end{bmatrix} - [\partial\Phi(\boldsymbol{\delta}_\alpha^{(r-1)}, \mathbf{F}_\alpha^{(r-1)})]^{-1} [\Phi(\boldsymbol{\delta}_\alpha^{(r-1)}, \mathbf{F}_\alpha^{(r-1)})] \quad (\text{B.11})$$

where $\partial\Phi$ is the Jacobian matrix of the application Φ .

Using the application (B.9), we compute the gradient of each component and we obtain the Jacobian matrix:

$$\partial\Phi = \begin{bmatrix} \mathbf{I}_{2 \times 2} & \mathbf{0}_{2 \times 1} & -\mathbf{W}_{tt} & -\mathbf{W}_{tn} \\ \mathbf{0}_{1 \times 2} & 1 & -W_{nt} & -W_{nn} \\ \frac{\partial\Phi_3}{\partial\boldsymbol{\delta}_t} & \mathbf{0}_{2 \times 1} & \frac{\partial\Phi_3}{\partial\mathbf{F}_t} & \frac{\partial\Phi_3}{\partial F_n} \\ \mathbf{0}_{1 \times 2} & q_n & \mathbf{0}_{1 \times 2} & 0 \end{bmatrix} \quad (\text{B.12})$$

where:

$$\begin{aligned} \frac{\partial\Phi_3}{\partial\boldsymbol{\delta}_t} &= q_t \mu F_n \Pi(\mathbf{F}_t - q_t \boldsymbol{\delta}_t), \quad \frac{\partial\Phi_3}{\partial F_n} = -\frac{\mu (\mathbf{F}_t - q_t \boldsymbol{\delta}_t)}{\|\mathbf{F}_t - q_t \boldsymbol{\delta}_t\|} \\ \frac{\partial\Phi_3}{\partial\mathbf{F}_t} &= \mathbf{I}_{2 \times 2} - \mu F_n \Pi(\mathbf{F}_t - q_t \boldsymbol{\delta}_t) \end{aligned}$$

and:

$$\frac{\partial}{\partial V} \left(\frac{V}{\|V\|} \right) = \Pi(\mathbf{V}) = \frac{1}{\|V\|^3} \begin{bmatrix} (v_2)^2 & -v_1 v_2 \\ -v_1 v_2 & (v_1)^2 \end{bmatrix}$$

If the first derivatives are sufficiently smooth and the initial point is not too far from one of the roots of the equations the convergence of the Newton's Iteration Method is quadratic.

Solving (B.11) in the case of sliding contact, we respect at the same time the Signorini's and Coulomb's laws.

B.3 Gauss-Seidel method for contact handling

In the previous section, we explained how can we manage the contact when just one node is in contact with the ground. In multi-contact case (m contacts), we need to take into account the coupling between the contact nodes. Using (B.8), we have $3m$ equations with $3m$ force unknowns and $3m$ movement unknowns.

Rewriting (B.8) as:

$$\boldsymbol{\delta}_\alpha - \mathbf{W}_{\alpha\alpha}\mathbf{F}_\alpha = \sum_{\beta=1, \beta \neq \alpha}^m \mathbf{W}_{\alpha\beta}\mathbf{F}_\beta + \boldsymbol{\delta}_\alpha^{free} \quad (\text{B.13})$$

If we "freeze" the contribution of the other contacts ($\beta \neq \alpha$), the first term of the right part in (B.13) is constant. Therefore, we obtain a linear relationship between the contact force \mathbf{F}_α and $\boldsymbol{\delta}_\alpha$. This method consists of solving the contact and friction law of α considering the contribution of the other contacts as "frozen".

As shown in [49], we can use an iterative Gauss-Seidel method to obtain a real-time solution of the contact problem respecting the Signorini's and Coulomb's laws. This method is well-adapted to sparse matrices and it converges, at least locally, when the system is over-constrained and there are multiple solutions. The convergence of this method is shown in [50].

The principle is to test the contacts one by one, and always in the same order, blocking all others to their most recently calculated value (see algorithm 2).

Using the algorithm 2, we find the contact node forces and then the node positions for a given foot position trajectory (foot translation and rotation).

Algorithm 2: Frictional contact problem using Gauss-Seidel method. q is the time step and h is the last time step; ε_1 , ε_2 , ε_3 are respectively the desired accuracy for contact problem, Signorini's law and Coulomb's law

Input: δ^{free} , W

Output: F

if $q = 1$ **then**

for $\alpha = 1 \dots m$ **do**

$F_\alpha = \mathbf{0}$

$\delta_\alpha^{free} = \begin{bmatrix} 0 \\ \mathbf{n}(RP_{l,\alpha} + \mathbf{O}_l) \end{bmatrix}$

if $q = 2 \dots h$ **then**

for $\alpha = 1 \dots m$ **do**

$F_\alpha = F_\alpha^{(q-1)}$

$\delta_\alpha^{free} = RP_{l,\alpha} + \mathbf{O}_l - \begin{bmatrix} P_{t,\alpha}^{(q-1)} \\ 0 \end{bmatrix}$

do

$F^{old} = F$

for $1 \leq \alpha \leq m$ **do**

$\delta_\alpha^{test} = \sum_{\beta=1, \beta \neq \alpha}^m W_{\alpha\beta} F_\beta + \delta_\alpha^{free}$

if $\delta_{n,\alpha}^{test} < \varepsilon_2$ **then**

$F_\alpha = -W_{\alpha\alpha}^{-1} \delta_\alpha$

if $\|F_{\alpha,t}\| > \mu F_{\alpha,n}$ **then**

$F_{\alpha,n} = -\delta_{\alpha,n}^{free} / W_m$

$\delta_\alpha = W_{\alpha\alpha} F_\alpha + \delta_\alpha^{free}$

do

$c = [\partial\Phi(\delta_\alpha, F_\alpha)]^{-1} [\Phi(\delta_\alpha, F_\alpha)]$

$\begin{bmatrix} \delta_\alpha \\ F_\alpha \end{bmatrix} = \begin{bmatrix} \delta_\alpha \\ F_\alpha \end{bmatrix} - c$

while $\Phi(\delta_\alpha, F_\alpha) > \varepsilon_3$

else

$F_\alpha = \mathbf{0}$

while $\frac{\|F - F^{old}\|}{\|F\|} > \varepsilon_1$

Résumé en français

Titre

Marche des robots humanoïdes avec des semelles souples

Introduction

Pour les humains, la marche est un comportement naturel appris pendant l'enfance pour se mouvoir d'un endroit à l'autre. La marche des humanoïdes bipèdes alterne les phases de création et de rupture de contact avec le sol. Afin d'éviter de tomber et de rentrer en collision avec l'environnement autour d'eux, les humains ont une stratégie d'équilibrage utilisant les différentes parties de leurs corps pour faire face aux perturbations. Cette stratégie est aidée par des pieds à la structure complexe et adaptative qui peuvent prendre la forme et la texture de l'environnement de contact. Un tel contrôle sur la marche permet aux humains de se déplacer presque partout et faire face aux incertitudes du sol durant la marche comme un sol pentu ou accidenté avec des graviers.

Le milieu de vie des humains a été façonné, optimisé et conçu à taille humaine pour des humanoïdes bipèdes. C'est pour cela que pour les aider dans leurs différentes tâches, les humains ont naturellement décidé de construire des robots humanoïdes. Du point de vue de la locomotion, les marcheurs bipèdes s'adaptent le plus facilement à tout type d'environnement. Cependant, les robots humanoïdes contemporains ont une faiblesse liée à la conception de leurs pieds. En effet, la plupart des robots humanoïdes ont des pieds plats et rigides

En comparaison et en simplifiant, les pieds humains ont :

- une enveloppe qui peut changer ses propriétés en étant souple (pour prendre la forme des petites irrégularités du sol et absorber le choc d'impact lors de la pose des pieds au sol) ou rigide (pour améliorer la stabilité)
- deux segments (talon et orteils) reliés par une articulation (pour augmenter les degrés de liberté du pied).

De tels pieds permettent aux humains d'avoir un contrôle adaptatif de l'interaction pied-sol. En effet, le centre de pression (CoP) sous chaque pied, qui est la somme des points de contact pondéré par leurs forces de réaction du sol (GRF) respectives, présente une trajectoire curviligne (voir la Fig. 6.1a). A l'inverse, dans la robotique humanoïde, en raison des limitations liées à la conception des pieds, les mouvements (et par extension les CoP) sont le plus souvent générés en ligne droite (voir la Fig. 6.1b).

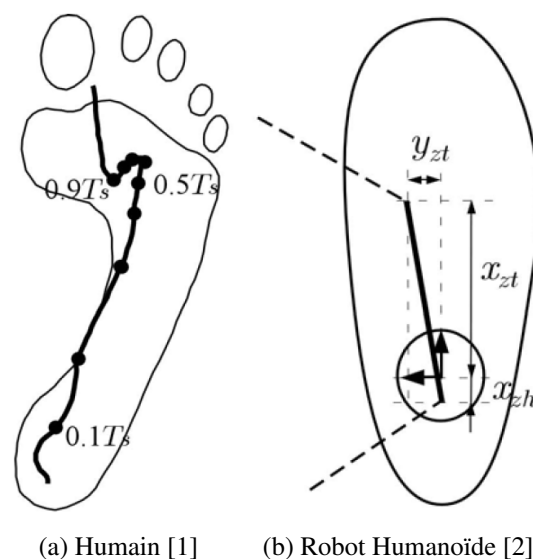


Figure 6.1 Exemple de trajectoires de CoP chez l'humain et en robotique humanoïde.

Ainsi, nous avons pointé la nécessité d'augmenter le nombre de degrés de liberté des pieds des robots humanoïdes. Nous avons choisi d'étudier l'ajout d'une semelle épaisse et souple sous les pieds des robots. Parce que, jusqu'à présent, aucun contrôleur de robots humanoïdes existant ne génère de mouvement pour marcher avec des semelles souples, la question est : *est-il possible pour un robot humanoïde de marcher avec des semelles souples ?*

Dans cette étude, nous nous intéressons à l'utilisation de semelles souples pour marcher. L'homme ayant un comportement naturel à marcher sur des matériaux souples (pieds, chaussures, matelas, ...). Nous allons commencer par examiner la stratégie d'équilibre des humains pour s'en inspirer pour le développement d'un contrôleur de robot humanoïde. Ensuite, nous développerons conjointement un générateur de modèle de marche (WPG) pour générer le mouvement du robot et un estimateur de déformation (DE) pour prédire la déformation de la semelle et la prendre en compte dans le mouvement du pied afin d'obtenir une marche stable. Cependant, en raison d'un temps de calcul élevé, une telle méthode empêche la génération de

mouvement en ligne et la réactivité du robot aux perturbations. Par conséquent, nous finirons par la conception d'un contrôleur en boucle fermée basé sur une simplification du DE pour suivre en ligne le mouvement de référence et traiter les déformations de la semelle. Tous ces développements sont validés par des tests expérimentaux sur de vrais robots humanoïdes HRP-2 et HRP-4.

Humain marchant sur un matériau mou inconnu

Le mouvement humain est un processus dynamique complexe nécessitant des actions correctives en continu pour maintenir l'équilibre [3]. Le contrôle efficace de la marche est un sujet central dans la robotique humanoïde et les méthodes de contrôle bio-inspirées peuvent apporter une solution au problème. Nous avons étudié le rôle des forces de réaction du sol (GRF) dans le contrôle de la locomotion humaine suite à des changements dans les propriétés de rigidité du sol.

Pour tester le changement de rigidité du sol sur le comportement humain, nous avons demandé à 10 personnes de marcher 10 fois sur une plate-forme ayant une partie du sol dure (H) et une autre molle (L) réalisée à partir d'un épais matelas de chute pour de la gymnastique. La cinématique du corps humain est enregistrée avec un système de capture de mouvement VICON composé de 10 caméras infrarouges traquant la position de 42 marqueurs réfléchissants collés sur les participants. Des ForceShoes possédant deux capteurs de forces et de couples sous les semelles sont utilisés pour enregistrer les GRF sous les pieds pendant tout l'essai. La position du CoP est reconstruit à partir des GRF mesurés sous chaque pied et de la position des marqueurs collés sur chaque pied.

A partir des mesures, on observe une forme classique en double pic des GRF verticaux sur sol dur. Ensuite des différences nettes dans les amplitudes de crête sont visibles sur un matelas mou entre les pics d'atterrissage et les pics juste avant la poussée vers le pas suivant. La distance de CoP sous le dernier pas sur sol dur a augmenté au cours des essais tout en restant quasiment constante lors du premier pas sur le matelas mou.

En conclusion, la GRF est probablement modulée pour atténuer l'accélération du centre de masse (COM) lors de la "chute" en raison de la transition sur le matelas mou en exploitant ses propriétés de déformation pour dissiper l'énergie mécanique. Des analyses supplémentaires sont nécessaires pour mieux comprendre la mécanique de la transition. Néanmoins, ces résultats vont inspirer le développement d'un générateur de modèle de marche (WPG) pour robots humanoïdes basés sur le comportement de GRF et d'un estimateur de déformation (DE) pour prendre en compte lors de la marche la déformation de surfaces souples.

Un générateur de modèle de marche d'humanoïde avec des semelles souples

La génération de démarche et le contrôle des robots bipèdes est difficile car ils n'ont pas de bases fixes et les points d'appuis ne sont pas continus sur le sol. Il existe de nombreuses méthodes numériques permettant de générer des mouvements. Le point de moment nul (ou ZMP) est habituellement utilisé comme critère dynamique pour la planification des démarches et le contrôle des robots pour avoir une marche stable. Vukobratovich *et al.* sont les premiers à avoir proposé le concept de ZMP [27][26].

Pour faire simple, sur sol plat, le ZMP est le point d'application des forces de réaction du sol sur le robot. Durant les phases de simple support (SSP), le ZMP est confondu avec le point de contact du pied sur le sol et pendant les phases de double support (DSP), le ZMP est le point d'application de la force de réaction globale du sol sur le robot complet (barycentre entre les points d'application des forces de réaction sous chaque pied sur le sol pondérés par leur force associée). Et si le ZMP se trouve dans les polygones de stabilité, le robot est stable. En SSP, les polygones sont les aires des pieds sur le sol et en DSP, ils incluent également les aires entre les deux pieds.

L'humain cherchant dans la plupart des cas à optimiser l'ensemble de ses mouvements naturels pour moins se fatiguer, nous avons naturellement choisi de nous en inspirer pour choisir nos critères d'optimisation. Ceux-ci sont basés sur des critères énergétiques inspirés par les humains [3][31].

En simplifiant le modèle des robots humanoïdes, les seuls actionneurs que nous allons traiter sont ceux des chevilles. L'énergie dépensée par le robot va être l'énergie des forces d'inertie appliquées au COM (aussi appelées forces du COM). Au final, notre critère inspiré par l'humain va être une combinaison entre la minimisation des couples chevilles et l'énergie du COM qui se retrouve être une combinaison entre les deux critères choisis par Wieber *et al.* [29] et Kajita *et al.* [28, 25].

En utilisant un modèle de pendule linéaire inversé et un modèle de chariot sur table [25], on obtient une relation entre le ZMP et le COM:

$$x_{\text{ZMP}} = x_{\text{COM}} - \frac{z_{\text{COM}} - z_{\text{ZMP}}}{g} \ddot{x}_{\text{COM}} \quad (6.14)$$

où x_{ZMP} est la coordonnée du ZMP suivant l'axe \vec{x} , g est la constante de gravité et \ddot{x}_{COM} est l'accélération du COM suivant l'axe \vec{x} .

On a choisi de générer des trajectoires de ZMP à partir d'une succession de polynômes de degré 5 interpolés entre des points de passage avec des conditions de continuité en position,

vitesse et accélération (qui seront les variables d'optimisation du problème de minimisation de l'énergie consommée). En résolvant l'équation différentielle (6.14), on peut écrire les trajectoires du COM comme des fonction linéaire du ZMP.

Enfin, inspiré par l'humain qui contrôle ses CoP sous chacun de ses pieds et pour concevoir un estimateur de déformation (DE) des semelles souples qui nécessite de connaître les CoP sous chacun des pieds et les GRF qui leurs sont associés, nous avons défini une méthode basée sur la distribution des forces entre chacun des pieds en DSP pour générer ces paramètres.

Finalement nous avons testé notre WPG sur le robot humanoïde HRP-2 dont les différentes expériences en faisant varier les poids du critère d'optimisation sont visibles dans la video¹. On observe que l'on arrive bien à marcher et à choisir différents comportements du COM lors de la marche. Néanmoins lors de ces tests, les déformations des semelles n'étaient pas prises en compte ce qui empêche d'utiliser des semelles trop souples et d'où la nécessité de développer un DE.

Estimateur de déformation de semelle souple

Afin de contrôler plus efficacement l'interaction pieds-sol des robots humanoïdes pendant la marche, nous avons étudié l'ajout de semelles extérieures souples (c'est-à-dire déformables) sous les pieds. La déformation induite par le contact entre les semelles et le sol est prise en compte en utilisant notre nouveau générateur de modèle de marche et un estimateur de déformation (DE) [37, 17]. Cette nouvelle approche de marche humanoïde garantit que le ZMP désiré est mieux suivi avec des semelles souples.

Dans la planification et le contrôle basés sur des modèles simplifiés, la flexibilité de la cheville et la déformation de la semelle ne sont pas modélisées. Elles sont laissées en tant que «perturbations» ou «incertitudes» pour être abordés par le contrôleur en boucle fermée. Par conséquent, les contrôleurs doivent compenser les erreurs dans l'attitude (c'est-à-dire l'orientation et la position de la base flottantes) en raison des déformations des pièces flexibles.

Dans notre schéma de contrôle, nous considérons le modèle de déformation résultant du contact de la semelle souple avec le sol. Cet estimateur de déformation se base sur :

- un modèle élément fini (FEM) des semelles souples pour calculer les déformations et les forces appliqués à la semelle en fonction du déplacement du pied par rapport au sol

- des lois mécaniques associant (i) la loi de Signorini, pour faire respecter la non-interpénétration (dans le calcul) de la semelle avec le sol, et (ii) la loi de Coulomb, qui définit le frottement sec associé aux différents points de contacts.

On obtient ainsi une relation liant le déplacement en position et orientation du pied au centre de pression (CoP) sous la semelle ainsi que la GRF associée.

Néanmoins, pour prendre en compte la déformation de la semelle lors du mouvement du robot, nous avons besoin connaître l'orientation et la position du pied par rapport au sol pour satisfaire les trajectoires de CoP et l'intensité de la force associée générés par le WPG. Pour résoudre ce problème, nous avons utilisé la méthode de Newton à partir de la relation différentielle donnée par l'estimateur de déformation. Ainsi, on prédit la trajectoire du pied en contact avec le sol qui permettra au robot d'être stable durant la marche.

Finalement nous avons testé notre DE sur le robot humanoïde HRP-4 dont les différentes expériences sont visibles dans la video². On observe que l'on arrive bien à marcher, ce qui valide ainsi le modèle de la semelle souple et la prise en compte de ses déformations par le DE. Néanmoins lors de ces tests, tous les mouvements sont générés hors-ligne puis directement joués sur le robot qui se retrouve avec un contrôle en boucle ouverte. Ainsi, le succès de la marche du robot se retrouve très impacté par les conditions initiales du robot et les possibles perturbations (sol pas tout à fait plat, modèle FEM qui simplifie le comportement de la semelle, ...), d'où la nécessité de développer un contrôleur en boucle fermée pour palier à ces sources d'erreurs.

Un contrôleur en boucle fermée pour marcher avec des semelles souples

La structure de contrôle utilisée avant n'avait aucune prise en compte de retour d'état du robot car tout le mouvement était planifié hors-ligne ce qui empêche d'être réactif pour corriger le mouvement. Pour pallier à cela, nous avons développé un contrôleur en boucle fermée pour les robots bipèdes marchant avec des semelles souples sur terrain plat et irréguliers. Le but de ce contrôleur est de minimiser l'erreur de suivi en termes de vitesse COM, de position du COM et du ZMP avec un contrôle en admittance des pieds basé sur un simple estimateur de déformation des matériaux sous les pieds. Cela se traduit par un contrôle en admittance aux chevilles dont les gains sont basés sur la rigidité de la semelle dans un état nominal à partir du modèle FEM. La structure de ce nouveau contrôleur se déroule comme suit:

- Un générateur de modèle de marche (WPG) [16, 17] produit des trajectoires de COM et de ZMP désirés, ainsi que la vitesse de COM désirée et la matrice de rigidité de la semelle souple.
- Un contrôleur de suivi ZMP-COM génère un ZMP de contrôle qui doit compenser les erreurs de COM et de ZMP entre les mesures et leurs références respectives de WPG. Ce contrôleur est basé sur un contrôle par retour d'état proportionnel et intégral sur l'erreur du COM.
- Une couche de distribution du ZMP de contrôle qui le convertit en centres de pression (CoP) de contrôle sous chacun des pieds en contact et distribue les GRF associés. Cette distribution est basée sur une solution analytique qui minimise les couples aux chevilles du robot.
- Une couche de contrôle de la force de réaction met à jour les positions et orientations des pieds pour obtenir les CoP de contrôle et leurs GRF associées utilisant un contrôle en admittance [51]. Ce contrôle en admittance utilise les gains de la matrice de raideur de la semelle souple en FEM dans un état nominal. Pour simplifier le contrôle et permettre un contrôle en-ligne du robot, cette matrice est supposée constante avec un coefficient d'adaptation linéaire en fonction de la pression sous le pied.

Enfin, un contrôleur du corps complet avec une programmation quadratique (QP) produit finalement des mouvements conjoints qui suivent les trajectoires de référence du CoM et de contrôle des pieds [52] à partir de la couche de contrôle de la force de réaction et de la trajectoire COM générée par le WPG.

Finalement nous avons testé notre contrôleur en boucle fermée sur le robot humanoïde HRP-4 dont les différentes expériences dans la vidéo³. On observe que l'on arrive à marcher sur sol plat et sur un lit de graviers. L'action correctrice du contrôleur est bien active pour stabiliser le robot en prenant en compte la déformation supposée de la semelle.

Conclusion

Dans cette thèse, nous avons étudié l'ajout de semelles souples sous les pieds des robots humanoïdes. Le but de l'utilisation de ces semelles est de:

- augmenter les mouvements possible du pied en contact avec le sol
- protéger le robot de l'impact à la pose des pieds sur le sol

- prendre la forme de l'environnement pour faire face aux inégalités et aux irrégularités du sol pendant la marche.

Cependant, les degrés de liberté passifs induits par ces semelles génèrent des instabilités qui doivent être prises en compte dans le mouvement de marche. Inspiré par la stratégie d'équilibre humain, nous avons abordé ce problème en développant un contrôleur en boucle fermée basé sur un simple estimateur de déformation qui compense la déformation de la semelle pour stabiliser le mouvement de marche généré par un générateur de modèle de marche dédié. Nous avons testé et validé notre approche en faisant marcher un robot humanoïde HRP-4 sur un lit de graviers.

En conclusion, nous avons prouvé la possibilité pour les robots humanoïdes de marcher avec des semelles souples sur du gravier, un sol inégal, irrégulier et déformable. Des efforts de programmation ont été réalisés pour développer une nouvelle structure de contrôle pour le robot réel HRP-4 pour marcher avec des semelles souples. Par ce travail, nous avons beaucoup appris à propos de la stabilisation des bipèdes sur des matériaux souples.